



University of Kentucky
UKnowledge

Theses and Dissertations--Chemical and
Materials Engineering

Chemical and Materials Engineering

2014

FUNCTIONALIZED MEMBRANES FOR ENVIRONMENTAL REMEDICATION AND SELECTIVE SEPARATION

Li Xiao

University of Kentucky, xiaoli.tju@gmail.com

[Right click to open a feedback form in a new tab to let us know how this document benefits you.](#)

Recommended Citation

Xiao, Li, "FUNCTIONALIZED MEMBRANES FOR ENVIRONMENTAL REMEDIATION AND SELECTIVE SEPARATION" (2014). *Theses and Dissertations--Chemical and Materials Engineering*. 32.
https://uknowledge.uky.edu/cme_etds/32

This Doctoral Dissertation is brought to you for free and open access by the Chemical and Materials Engineering at UKnowledge. It has been accepted for inclusion in Theses and Dissertations--Chemical and Materials Engineering by an authorized administrator of UKnowledge. For more information, please contact UKnowledge@lsv.uky.edu.

STUDENT AGREEMENT:

I represent that my thesis or dissertation and abstract are my original work. Proper attribution has been given to all outside sources. I understand that I am solely responsible for obtaining any needed copyright permissions. I have obtained needed written permission statement(s) from the owner(s) of each third-party copyrighted matter to be included in my work, allowing electronic distribution (if such use is not permitted by the fair use doctrine) which will be submitted to UKnowledge as Additional File.

I hereby grant to The University of Kentucky and its agents the irrevocable, non-exclusive, and royalty-free license to archive and make accessible my work in whole or in part in all forms of media, now or hereafter known. I agree that the document mentioned above may be made available immediately for worldwide access unless an embargo applies.

I retain all other ownership rights to the copyright of my work. I also retain the right to use in future works (such as articles or books) all or part of my work. I understand that I am free to register the copyright to my work.

REVIEW, APPROVAL AND ACCEPTANCE

The document mentioned above has been reviewed and accepted by the student's advisor, on behalf of the advisory committee, and by the Director of Graduate Studies (DGS), on behalf of the program; we verify that this is the final, approved version of the student's thesis including all changes required by the advisory committee. The undersigned agree to abide by the statements above.

Li Xiao, Student

Dr. Dibakar Bhattacharyya, Major Professor

Dr. Thomas Dziubla, Director of Graduate Studies

FUNCTIONALIZED MEMBRANES FOR ENVIRONMENTAL
REMEDICATION AND SELECTIVE SEPARATION

DISSERTATION

A dissertation submitted in partial fulfillment of the
requirements for the degree of Doctor of Philosophy in the
College of Engineering
at the University of Kentucky

By
Li Xiao
Lexington, Kentucky

Director: Dr. Dibakar Bhattacharyya, Alumni Professor of Chemical
Engineering
Lexington, Kentucky

2014

Copyright © Li Xiao 2014

ABSTRACT OF DISSERTATION

FUNCTIONALIZED MEMBRANES FOR ENVIRONMENTAL REMEDICATION AND SELECTIVE SEPARATION

Membrane process including microfiltration (MF), ultrafiltration (UF), nanofiltration (NF) and reverse osmosis (RO) have provided numerous successful applications ranging from drinking water purification, wastewater treatment, to material recovery. The addition of functional moiety in the membranes pores allows such membranes to be used in challenging areas including tunable separations, toxic metal capture, and catalysis. In this work, polyvinylidene fluoride (PVDF) MF membrane was functionalized with temperature responsive (poly(N-isopropylacrylamide), PNIPAAm) and pH responsive (polyacrylic acid, PAA) polymers. It's revealed that the permeation of various molecules (water, salt and dextran) through the membrane can be thermally or pH controlled. The introduction of PAA as a polyelectrolyte offers an excellent platform for the immobilization of metal nanoparticles (NPs) applied for degradation of toxic chlorinated organics with significantly increased longevity and stability. The advantage of using temperature and pH responsive polymers/hydrogels also includes the high reactivity and effectiveness in dechlorination.

Further advancement on the PVDF functionalization involved the alkaline treatment to create partially defluorinated membrane (Def-PVDF) with conjugated double bounds allowing for the covalent attachment of different polymers. The PAA-Def-PVDF membrane shows pH responsive behavior on both the hydraulic permeability and solute retention. The sponge-like PVDF (SPVDF) membranes by phase inversion were developed through casting PVDF solution on polyester backing. The SPVDF membrane was demonstrated to have 4 times more surface area than commercial PVDF MF membrane, allowing for enhanced nanoparticles loading for chloro-organics degradation. The advanced functionalization method and process were also validated to be able to be

scaled-up through the evaluation of full-scale functionalized membrane provided by Ultura Inc. California, USA.

Nanofiltration (NF) between UF and RO presents selectivity controlled by both steric and electrostatic repulsions, which are widely used to reject charged species, particularly multivalent ions. In this work, selective permeation of CaCl_2 and high sucrose retention are obtained through the modification of nanofiltration membranes with lower charge compared to commercial nanofiltration membrane. The membrane module also shows high stability with constant water permeability in a long-term (two months) test. Extended Nernst-Planck equation were further used to evaluate the experimental results and it fits well.

KEY WORDS: Functionalized Membrane, Dechlorination, Responsive, Tunable, Full-scale

Li Xiao

June 30, 2014

FUNCTIONALIZED MEMBRANES FOR ENVIRONMENTAL
REMEDICATION AND SELECTIVE SEPARATION

By

Li Xiao

Dr. Dibakar Bhattacharyya

Director of Dissertation

Dr. Thomas Dziubla

Director of Graduate Studies

June 30, 2014

ACKNOWLEDGEMENTS

First, I would like to express my deep appreciation and gratitude to my academic advisor, Dr. Dibakar Bhattacharyya for all his support, instructions and encouragement that he provides to me throughout my graduate study. His deep passion, innovative and dedication to research always impress me and I am sure it will keep inspiring me in future. Thanks for providing the amazing opportunities, such as conference and journal manuscript/proposal writing, which makes my graduate student experience fulfill. I am truly fortunate to have had the opportunity to work with Dr. Dibakar Bhattacharyya.

I would also like to thank the members of my doctoral committee: Dr. J. Zach Hilt, Dr. Stephen E. Rankin, and Dr. Lindell Ormsbee for their helpful comments and suggestions to my research work and their valuable time on reviewing my dissertation. Thank you as well to Mr. John May and Ms. Tricia Coakley from Environmental Research Training Laboratory for teaching and helping me in different analysis.

I would like to thank the National Institute of Environmental Health Sciences Superfund Research Program (NIEHS-SRP), and the Department of Energy (DOE)-Kentucky Research Consortium for Energy and Environment for the funding of this research. I would also thank Ultura. Inc. Oceanside, CA for their significant contributions on the development of full-scale membranes.

I am thankful to my lab-mates past and present: Dr. Scott Lewis, Dr. Noah Meeks, Dr. Vasile Smuleac, Ms. Ruo He, Mr. Minghui Gui, Mr. Sebastian

Hernandez, Mr. Andrew Colburn and Mr. Andrew Tomaino. Thanks to undergraduate students: Mr. Austin Isner, Ms. Krysta Waldrop, Mr. Anthony Saad and Mr. Doug Davenport for their contribution to this work. The experience of working with them was enjoyable and memorable.

My family's support is very important during every stage of my PhD support even they are far away from me. Thanks for their continuous encouragement and motivation. I will miss both of them a lot.

And now, the most important person in my life: my husband Kun. I am very lucky to have you in my life. How can I ever thank you for all you have done for me. Encouraging me when things are rough, cheering me up when I have a bad day in the lab. Thank you for everything!

Table of Content

Acknowledgements.....	iii
List of Figures	xii
List of Tables	xx
Chapter 1 - Introduction and Background	21
1.1 Introductory remarks	21
1.2 General background.....	23
1.2.1 Functionalized membrane.....	23
1.2.2 Functionalization techniques.....	23
1.2.3 Phase inversion for membrane fabrication.....	26
1.2.4 Stimuli-Responsive material	27
1.2.5 Functionalized membrane for nanoparticles synthesis	32
1.2.6 Nanofiltration.....	34
1.3 Objectives and outlines	35
Chapter 2 - Responsive Hydrogel-Supported Metallic Nanoparticles Synthesis and Water Remediation	37
2.1 Introduction	37
2.2 Experimental Methods.....	40
2.2.1 Materials	40
2.2.2 Synthesis of Crosslinked PNIPAAm-PAA Hydrogel	40

2.2.3 In-situ Synthesis of Nano-sized Iron Particles in Hydrogel Matrix.....	41
2.2.4 Characterization of Fe ⁰ Nanoparticles and Hydrogel Nanocomposite	43
2.2.5 Measurements of Swelling Ratio under Different Temperature	43
2.2.6 Hydrophobicity and Hydrophilicity Transitions of Temperature- Responsive Hydrogel Measured by Model Organic Partitioning Experiments	44
2.2.7 Adsorption Experiment.....	44
2.2.8 Dechlorination by Fe/Pd Nanoparticles in P(NIPAAm-AA) Hydrogel ..	45
2.2.9 Chloride Analysis	46
2.2.10 Metal Analysis.....	46
2.3 Results and Discussion	47
2.3.1 Synthesis of P(NIPAAm-AA) hydrogel	47
2.3.2 Synthesis of Reactive Fe Nanoparticles in P(NIPAAm-AA) Hydrogel .	50
2.3.3 Swelling Study of Temperature Responsive P(NIPAAm-AA) Hydrogel	52
2.3.4 Establishment of Hydrophobicity and Hydrophilicity Transitions of Temperature Responsive Hydrogel by Model Organic Partitioning Experiments.....	56
2.3.5 Reductive Reaction by Hydrogel Immobilized Nanoparticles	57
2.3.6 Role of Temperature Responsive Behavior	62
2.4 Conclusions.....	68

2.5 Broad Application Prospect	69
Chapter 3 - Development of Bench and Full-Scale Temperature and pH	
Responsive Functionalized PVDF Membranes with Tunable Properties	71
3.1 Introduction	71
3.2 Experimental	74
3.2.1 Materials	74
3.2.2 Synthesis of PNIPAM-functionalized PVDF Millipore Membrane.....	74
3.2.3 Attenuated Total Reflectance Fourier Transform Infrared (ATR-FTIR)	77
3.2.4 Scanning Electron Microscopy (SEM).....	77
3.2.5 Thermal Analysis	78
3.2.6 Atomic Force Microscopy (AFM).....	78
3.2.7 X-ray Photoelectron Spectroscopy (XPS) Analysis of Membrane Surface	79
3.2.8 Temperature-responsive Flux Measurements	79
3.2.9 Dextran Rejection	79
3.2.10 Total Organic Carbon (TOC) Analysis	80
3.2.11 Gel Permeation Chromatography (GPC)	80
3.2.12 Salt Rejection through PNIPAAm-FPAA-PVDFHE Ultura Membrane	81
3.2.13 Metallic Nanoparticles Synthesis within PNIPAAm-FPAA-PVDFHE Membrane.....	81

3.3 Results and Discussion	82
3.3.1 ATR-FTIR Spectroscopy of PNIPAAm Functionalized PVDF Membrane	82
3.3.2 Thermal Analysis	83
3.3.3 Microstructure and Morphology Analysis	85
3.3.4 Temperature Responsive Water Flux through the PNIPAAm-PVDF Membranes	91
3.3.5 Quantification of Temperature Dependent Unsteady-state Membrane Flux	96
3.3.6 Temperature and pH Dependent Hydraulic Permeability of PNIPAAm- FPAA-PVDFHE Membrane.....	97
3.3.7 Dextran Rejection through PNIPAAm-PVDF Membranes.....	101
3.3.8 Na ₂ SO ₄ Rejection through PNIPAAm-FPAA-PVDFHE Ultra Membranes	105
3.3.9 Catalytic Dechlorination	106
3.4 Conclusion	109
3.5 Broad Application Prospect	110
Chapter 4 - Polymerization and Functionalization of Membrane Pores for Water Related Applications	111
4.1 Introduction	111
4.2 Experimental	113

4.2.1 Materials	113
4.2.2 Dehydrofluorination of PVDF Membrane (Def-PVDF).....	113
4.2.3 PAA functionalization of PVDF membranes (PAA-Def-PVDF).....	114
4.2.4 Preparation of Spongy PVDF Membranes (SPVDF).....	114
4.2.5 Attenuated Total Reflectance Fourier Transform Infrared (ATR-FTIR)	114
4.2.6 Scanning Electron Microscopy (SEM).....	115
4.2.7 X-ray Photoelectron Spectroscopy (XPS) Analysis of Membrane Surface	115
4.2.8 Water flux Measurement.....	115
4.2.9 Na ₂ SO ₄ Rejection	116
4.2.10 Synthesis of Fe/Pd Nanoparticles in Membrane and Dechlorination	116
4.3 Results and Discussion	117
4.3.1 Dehydrofluorination and PAA Functionalization of PVDF Membranes	117
4.3.2 SEM Analysis.....	119
4.3.3 XPS Analysis of PAA-PVDF Membranes.....	120
4.3.4 Thermal Analysis of Membranes.....	123
4.3.5 pH Responsive Flux of PAA Functionalized Def-PVDF	124
4.3.6 Ca ²⁺ Pick-up.....	125

4.3.7 Na ₂ SO ₄ Rejection	126
4.3.8 Reductive Dechlorination	128
4.3.9 Spongy PVDF Membranes (SPVDF)	129
4.4 Conclusion	134
4.5 Broad Application Prospect	134
Chapter 5 - Nanofiltration of Sugar Containing Salt: Interaction between Sugar and Salt on Retention	
5.1 Introduction	136
5.2 Experimental	138
5.2.1 Materials	138
5.2.2 Membrane Characterization.....	138
5.2.3 Apparatus	139
5.2.4 Analysis	141
5.2.5 Theory.....	141
5.3 Results and Discussion	148
5.3.1 Membrane Characterization.....	148
5.3.2 The Retention of Single Solute	152
5.3.3 Retention of Combined Sucrose and Salt	159
5.3.4 Stability	162
5.4 Conclusion	163

5.5 Broad Application Prospect	164
Chapter 6 - Conclusion	165
6.1 Key Advancements to Science and Engineering	165
6.2 Specific Accomplishments.....	166
6.2.1 Stimuli-responsive Materials for Tunable Separation and Reaction..	166
6.2.2 Membrane Functionalization Techniques	167
6.2.3 Full-scale Membrane Validation and Evaluation	168
6.3 Future work	168
Nomenclature	170
Appendix.....	178
References	183
Vita.....	220

List of Figures

Figure 1.1. Schematic illustration of a novel separation system using temperature responsive NIPAAm grafted on PP membrane[51].	31
Figure 2.1. Schematic diagram of P(NIPAAm-AA) by UV photopolymerization ..	41
Figure 2.2. Schematic of direct formation of Fe ⁰ nanoparticles in P(NIPAAm-AA) hydrogel network (upside) and the corresponding digital camera images (underside).	42
Figure 2.3. ATR-FTIR spectra of P(NIPAAm-AA) hydrogel, NIPAAm and AA monomers. The percentage of transmission scales varied in the range 100-10%.	49
Figure 2.4. SEM images of hydrogels after reaching swelling equilibrium at pH 6.5 below LCST at 25°C (A and B: surface and cross-sections, respectively) and above LCST at 40°C (C and D: surface and cross-sections, respectively).	49
Figure 2.5. SEM images of Fe ⁰ nanoparticles immobilized in P(NIPAAm-AA) hydrogel. A-Fe ⁰ nanoparticles immobilized in hydrogel by <i>in-situ</i> synthesis; B-Fe ⁰ nanoparticles immobilized in hydrogel by encapsulation.	52
Figure 2.6. Swelling ratio of different systems at different temperature. Circles: blank P(NIPAAm-AA) hydrogel without any nanoparticles; triangles: P(NIPAAm-AA) hydrogel with 0.95wt% nanoparticles by in-situ synthesis (dry weight: 0.2 g; pH at 25°C: 6.86).	55
Figure 2.7. Variation of polymer solvent interaction parameter (χ_p) with different temperatures. The values were calculated using Eq. 2-2.	56

Figure 2.8. Partitioning coefficients (K) of methylene blue (A) and orange II (B) as a function of temperature through P(NIPAAm-AA) hydrogel (pH=6.5). The insets are the molecular structures of methylene blue and orange II.57

Figure 2.9. TCE dechlorination of deionized ultra-filtered water (DIUF) and “real” water (Paducah, KY) with Fe nanoparticles in-situ and encapsulated in P(NIPAAm-AA) hydrogel. Vol. = 43mL, initial pH: 7 (for DIUF) and 7.5(for real water); initial TCE concentration: 30 mg/L, iron loading amount: 1g/L; Temperature: 25°C 62

Figure 2.10. Normalized TCE adsorption through temperature responsive P(NIPAAm-AA) hydrogel below LCST (15°C and 23°C) and above LCST (34°C), feed concentration: 0.2 mM TCE, 20 mL, pH=6.8..... 63

Figure 2.11. Batch dechlorination of TCE with Fe/Pd (Pd=1.5 wt%) (70nm) immobilized in P(NIPAAm-AA) hydrogel at 30°C (below LCST) and 34°C (above LCST). Vol. = 43mL, pH=6.8; initial TCE concentration: 30 mg/L, iron loading amount: 0.3g/L..... 65

Figure 2.12. Batch dechlorination of 2,2'-dichlorobiphenyl (DiCB) with Fe/Pd (Pd=2.4%) immobilized in P(NIPAAm-AA) hydrogel at 30°C (below LCST) and 34°C (above LCST). Vol. = 43mL, pH=6.8; initial DiCB concentration: 5 mg/L, iron loading amount: 0.5g/L. 66

Figure 2.13. Schematic of temperature behavior and transport of reagents with temperature responsive hydrogel immobilized Fe⁰ nanoparticles..... 67

Figure 3.1 Schematic of proposed interpenetrating network (IPN) formation by post PNIPAAm functionalization of full-scale cross-linked FPAA-PVDFHE Ultura membrane (PNIPAAm-FPAA-PVDFHE).....	76
Figure 3.2. ATR-FTIR spectrum of blank PVDF, PNIPAAm functionalized PVDF Millipore membrane and PNIPAAm-FPAA-PVDFHE Ultura membrane.....	83
Figure 3.3. TGA curves of blank PVDF(A), PNIPAAm functionalized PVDF membrane (B) and the PNIPAAm homopolymer (C). The heating rate is 10 °C/min.	84
Figure 3.4. DSC thermograms of (A) PNIPAAm-PVDF.....	85
Figure 3.5. SEM images of blank PVDF (A) and PNIPAAm-PVDF Millipore membranes (B: 25°C(below LCST); C: 40 °C (above LCST)).....	86
Figure 3.6 SEM images of full-scale FPAA-PVDFHE Ultura membrane surface (A) and cross-section(C) and PNIPAAm-FPAA-PVDFHE Ultura membrane surface (B) and cross-section (D).....	87
Figure 3.7. AFM image blank full-scale PVDFHE Ultura membrane, functionalized FPAA-PVDFHE membrane, PNIPAAm-FPAA-PVDFHE Ultura membrane: (a) top view and (b) 3D.	89
Figure 3.8. XPS survey (Left) and C1s core-level spectra (right) of (A) FPVDFHE; (B)FPAA-PVDFHE;(C) PNIPAAm-FPAA-PVDFHE membranes.....	91
Figure 3.9. Dependence of thermally on-off ratio on the cross-linker amounts in the range from 0.1-2.0 mol% in for PNIPAAm-PVDF Millipore membrane (P=1.4 bar). For all the membranes, the NIPAAm concentration for polymerization	

solution was 5 wt%. Data was corrected with viscosity and normalized by permeability at 30°C.....	94
Figure 3.10. Effect of monomer (NIPAAm) concentration on water flux at 1.4 bar and calculated effective pore size for PNIPAAm-PVDF Millipore membrane. cross-linker concentration = 1mol%.....	96
Figure 3.11. Dynamic and Reversible flux response versus ramp change in feed temperature above LCST and below LCST through PNIPAAm-PVDF Millipore membrane at P = 1.4 bar. The inset is the experimental temperature step change approximation. For the polymerization, the NIPAAm concentration was 5 wt%, cross-linker was 0.1mol%.	97
Figure 3.12. Temperature and pH effects on the pure water flux at 3.8 bar through PNIPAAm-FPAA-PVDFHE Ultura membrane. For the polymerization, the NIPAAm concentration was 13 wt%, cross-linker was 1mol%. The inset is the temperature effect on the full-scale FPAA-PVDFHE Ultura membrane (pH=6.5, P=0.3 bar). All the flux Data were corrected with viscosity. Data are fitted by error function. Dark red broken circles represent the flux data obtained with different temperature at pH=6.3 after the run at pH=7.3 to check the stability and reversibility.....	99
Figure 3.13. The effects of temperature and monomer concentration on dextran rejection with PNIPAAm-PVDF Millipore membrane (5mol% cross-linker) ($M_w=2,000,000$ g/mol; stoke radius $r_s= 26.1$ nm, calculated from $r_s=0.27 \cdot M_w^{0.498}$).	103

Figure 3.14. The effects of temperature and pH on dextran rejection of PNIPAAm-FPAA-PVDF Ultura membrane ($M_w=2,000,000\text{g/mol}$; stoke radius $r_s=26.1\text{nm}$, calculated from $r_s=0.27 \cdot M_w^{0.498}$).	103
Figure 3.15. GPC results of dextran rejection with PNIPAAm-PVDF Millipore membrane below and above LCST (PNIPAAm-PVDF membrane was made of 5% NIPAAm and 5% cross-linker).	104
Figure 3.16. Na_2SO_4 rejection through PNIPAAm-FPAA-PVDFHE Ultura membrane at different temperatures (feed conc.=100 mg/L and 1000 mg/L, $P=3.8$ bar, $\text{pH}=6.5$).	106
Figure 3.17. Iron loading amount by three times of ion exchange under convective flow and corresponding water permeability through PNIPAAm-FPAA-PVDFHE Ultura membrane. Fe-1, Fe-2 and Fe-3 are iron nanoparticles formed by the 1 st , 2 nd and 3 rd ion exchange.	107
Figure 3.18. TCE dechlorination using Fe/Pd nanoparticles (diamond symbols) in PNIPAAm-FPAA-PVDF Ultura membrane .The inset figure is the SEM image of nanoparticles in membrane pore. The diamond symbols represent the control experiment with only membrane (no metal particles).	109
Figure 4.1. Change in color of the PVDF membranes after treatment with 15% of NaOH for different hours at 70°C: (a) 0h, (b) 1h, (c) 3h, (d) 22h.	118
Figure 4.2. ATR-FTIR spectrum of blank PVDF, Def-PVDF and PAA-Def-PVDF membranes. A: blank PVDF; B:Def-PVDF with 1h NaOH treatment; C: Def-PVDF with 3h NaOH treatment; D: Def-PVDF with 22h NaOH treatment; E: PAA-Def-PVDF (3h's treatment).	119

Figure 4.3. SEM image of blank PVDF (A), dehydrofluorinated PVDF-3h	120
Figure 4.4. XPS survey spectra of PVDF (A), Def-PVDF(B), and PAA-Def-PVDF(C).	122
Figure 4.5. Changes in XPS elemental percentages of fluorine and carbon with different treatment time with 6 M NaOH.....	122
Figure 4.6. XPS C1s core-level spectra of blank PVDF (A) and PAA-Def-PVDF (B) membranes.	123
Figure 4.7. DSC thermogram of (a)pristine PVDF, (b) Def-PVDF, (c)PAA-PVDF by pore filling method and (d) PAA-Def-PVDF.....	124
Figure 4.8. pH effect on the pure water permeability of the PAA-Def-PVDF functionalized membrane.....	125
Figure 4.9. Effect of feed solution pH on the ion exclusion (P=0.7 bar)	127
Figure 4.10. Effect of operating pressures on the ion exclusion of a 100 mg/L Na ₂ SO ₄ solution at pH=6.5 through PAA-Def-PVDF membrane.....	128
Figure 4.11. TCE dechlorination by Fe nanoparticles immobilized in PAA-Def-PVDF membrane. Vol.=43 mL, initial pH=6.8, initial TCE concentration: 30 mg/L, iron loading amount: 0.2 g/L (Pd=1.4wt% of Fe), Temp.= 25 °C.....	129
Figure 4.12. SEM images of surface and cross-section spongy PVDF morphology under different magnification (a) surface, ×15k; (b) cross-section of whole picture, ×300; (c) skin surface and macroporous matrix, ×4k; (d) microporous matrix under skin surface, ×10k; (e) interconnected fibrous structure in the microporous matrix, ×10k.....	131

Figure 4.13. SEM image of surface and cross-section of PAA-SPVDF morphology (a) surface, x15k; (b) overall of cross-section, x1k; (c)magnified structure, x15k.	132
Figure 4.14. SEM-EDS spectra of PAA -SPVDF membranes loaded with calcium ions.	133
Figure 5.1. Schematic of cross-flow permeating experimental set-up.....	140
Figure 5.2. Schematic diagram of numeric calculation procedure for effective charge density of nanofiltration membrane using extended Nernst-Planck model.	147
Figure 5.3. SEM image of surface (a) and cross-section (b) of SNF20 membranes, surface (c) and cross-section (d) of NF3A membranes.....	149
Figure 5.4. AFM image of SNF20 (a) and NF3A(b) membrane.	150
Figure 5.5. Pure water flux and the flux at 2 g/L sucrose versus the pressure of SNF20 (a) and NF3A (b).....	152
Figure 5.6. Rejection of sucrose and glucose as a function of permeate flux for SNF20 module (a) and NF3A module (b). The line shows fitting with Donnan-Steric-Pore model.	154
Figure 5.7. Rejection of CaCl_2 as a function of permeate flux for SNF20 module (a) and NF3A module (b) (square: 0.001 M; diamonds: 0.01M; circles: 0.05M). The modification of flux is through the change applied pressure. The line shows fitting with extended Nernst-Planck model.	157
Figure 5.8. Calculated effective charge density (X_d) as a function of different CaCl_2 concentration. Logarithm coordinates are used for better comparison. ...	158

Figure 5.9. Rejection curve of 10 mol/m³ CaCl₂ solution through SNF20 membrane with different effective charge density. 159

Figure 5.10. Rejection of sucrose (a) and CaCl₂ (b) for SNF20 membrane with different CaCl₂ concentration (2 g/L and 4 g/L) and constant sucrose concentration at 10 g/L. The flux is modified by the change of applied pressure. 160

Figure 5.11. Rejection of sucrose and CaCl₂ for NF3A module as a function of permeate flux for feeds containing 2 g/L sucrose and 2 g/L CaCl₂. The flux is modified by the change of applied pressure. 161

Figure 5.12. Rejection of CaCl₂ (a) and sucrose (b) for SNF20 membrane with different sucrose concentration (2 g/L and 10 g/L) and constant CaCl₂ concentration at 2 g/L. The flux is modified by the change of applied pressure. 161

Figure 5.13. The long term stability of SNF20 module over six months' run. (The pure water flux was normalized with viscosity at 25°C; P=10.4 bar. Membrane area: 6.4 ft²). 163

List of Tables

Table 1.1. pH responsive polymers.....	29
Table 3.1 Functionalized Membranes Utilized in Experiments.....	77
Table 3.2. Temperature responsive water flux fitting parameters (Eq. 3-4) by error function ($T_c = LCST$; ΔT are in $^{\circ}C$).....	99
Table 4.1. Comparison of SPVDF and PVDF(Millipore).....	130
Table 4.2. Comparison of PAA functionalization of SPVDF and PVDF(Millipore); adsorption data obtained using 1000 mg/L $CaCl_2$ solution at pH 6.3	133
Table 5.1. Input data for bulk values for DSPM model calculation	154
Table 5.2. Calculated pore radius (r_p) and effective thickness over porosity($\Delta x/A_k$)for SNF20 and NF3A membrane obtained by using Donnan- Steric-Pore Model (Eq. 5-2).	155
Table 5.3. Input values for known parameters in modeling.....	157

Chapter 1 - Introduction and Background

1.1 Introductory remarks

Access to clean water has been identified as one and critical challenge for world's social and economical growth[1-3]. The development of alternative water supplies is urgent and fundamental. One challenge is to develop efficient, less energy consumption process through recovering pure water from industrial, brackish and salt water. Membrane technology is known to be a promising and leading candidate for providing fresh water via desalination and reuse of industrial wastewater[4]. On the other hand, the contamination of groundwater aquifers and soils at various superfund sites by chlorinated organics, such as, trichloroethylene, TCE and polychlorinated biphenyls, PCBs, etc, are a pervasive problem that can prevent the use of these sources as a potential for clear water. They have high toxicity, persistence and widespread distribution in the world[5-7]. Although many of remediation techniques have been developed, such as microbial transformation, carbon adsorption, etc, they are chemical-intensive, energy intensive and/or requires additional post-treatment to remove unwanted by-products. In our previous publications, we have introduced a novel and environmental benign approach by using metal nanoparticles to degrade and detoxify toxic chlorinated organic compounds from water[8-10]. In this work, we integrate nanostructured metal particles within functionalized polymer membranes to obtain highly effective detoxification of chloro-organics.

This chapter serves as a platform to provide background knowledge for better understanding this work on the membrane functionalization, membrane

technology and the integration of membrane and nanoparticles for remediation. Membrane technology presents attractive traits including ease of manufacture and operation, compactness and modular design, which make the membranes more attractive for various industrial applications[11, 12]. Membrane processes such as, microfiltration (MF), ultrafiltration (UF), nanofiltration (NF) and reverse osmosis (RO) have been widely used in separation applications ranging from water purification, wastewater treatment, chemical recovery, to advanced bioseparation[13]. The separation by these membranes is primarily based on size exclusion or steric hindrance effect. For more dense NF membranes, the separation is also coupled with electrical or Donnan exclusion. RO process is dominated by partitioning between solutes and membrane surface and diffusion difference. However, these conventional membranes has limitations in some challenging separation applications, for example biomedical area. Thus, there is growing interest on the modification of membrane to enhance the performance and efficiency of membrane process. Membrane functionalization allows creation of specific properties, such as high adsorptive capacity, selectivity, tunable separation and antifouling, which is equally essential for the design of advanced membrane in industries with less energy and material cost[14]. Thus, the primary focus of this chapter is to discuss various functionalization techniques for the fabrication of advanced membranes. Special attention will be given on the functionalized membranes with stimuli-response, selectivity, and reactions.

1.2 General background

1.2.1 Functionalized membrane

Current research for membrane modification are focusing on the introduction of functional groups into membranes. The most common functional groups are -OH, -COOH, -NH₂, -SH, -SO₃H, -CONH₂, etc. The functionalized membrane with proper activating groups can extend the application ranging from selective and tunable permeation and separation[15-17], toxic metal capture[18, 19], nanoparticles immobilization for toxic organics degradation[16] to biocatalyst[20].

1.2.2 Functionalization techniques

Membrane functionalization can be achieved through either non-covalent or covalent attachment. Simply, these modification methods are built on in-situ polymerization, simple adsorption, or grafting to/on the existing support material[21-25]. The functional techniques will be discussed in this chapter includes coating (Section 1.2.2.1), layer-by-layer assembly (Section 1.2.2.2), grafting(Section 1.2.2.3) and in-situ hydrogel cross-linking(Section 1.2.2.4).

1.2.2.1 Coating

Coating is a simple physical functionalization method and can be achieved through three different ways[26]: (1) adsorption/adhesion of hydrophilic or biocompatible materials on the base polymer support. The interaction between functional groups in the molecule and membrane surface can enhance the binding strength; (2) interpenetration at the interface between the macromolecules and base polymer support; (3) entanglement of the

macromolecules and the membrane pore structure. Through the modification, the membrane surface properties can be modified from hydrophobic to hydrophilic. The disadvantage is the low stability caused by the leaching of the adsorbed functional material from the membrane.

1.2.2.2 Layer-by-layer assembly (LBL)

Layer-by-Layer assembly is a newly developed membrane functionalization method introduced by Decher's group[27]. The mechanism for this simple but highly versatile method is based on not only electrostatic interactions, but also covalent bonding, hydrogen bonding, hydrophobic interactions and partitioning[28]. Typically, LBL is achieved by the adsorption of charged layer onto a layer with opposite charge. Depending on the practical application and requirements, the surface charge, film thickness, and composition can be tuned with the different adsorbed molecules, number of layers deposited[29]. The versatility of LBL allows for the broad applications including other functionalization on nanoparticles, polymers, proteins and dye molecules[28].

1.2.2.3 Grafting

Grafting is a chemical modification method and can be classified by four major types: chemical, radiation, photochemical and plasma induced polymerization[30]. Compared with physical modification, such as coating, grafting offers covalently attachment with membrane structure and maintains long-term stability. Besides, the key benefit for this technique is that the membrane surface can be tailed with the choice of different monomers to obtain

desirable properties. Chemical grafting involves two major types: free radical and ionic. Free radical polymerization contains three major steps: initiation, propagation and termination. In addition to general free radical polymerization, atom transfer radical polymerization (ATRP) and reversible free radical-fragmentation chain transfer polymerization (RAFT) have received increasing interest ascribed to their controllable reaction and narrow molecular weight distribution. Radiation grafting includes pre-irradiation by vacuum or an inert gas to form free radicals, peroxidation with formed hydroperoxides or diperoxides in the presence of air or oxygen, and mutual irradiation technique[30]. The major drawback for this technique is the potential destruction of polymer support by irradiation. Plasma grafting is a well-established technique for membrane functionalization to form linear polymer chains in the porous supports. The graft copolymerization is initiated by the macromolecule radicals formed via the cleavage of chemical bonds in the base structure[31]. This technique has been utilized for the grafting of poly(acrylic acid) onto polypropylene with enhanced printability or adhesion[32]. The weakness for this method is the production of the various side reactions caused by strong interaction between plasma species (electrons, ions, etc) and the base polymer supports[33].

1.2.2.4 In-situ hydrogel cross-linking

In-situ hydrogel cross-linking is the incorporation of cross-linked hydrogel inside the porous material. Hydrogels also possess a degree of flexibility to undergo a large amount change of volume[34]. However, the lack of mechanical strength confines its applications in separation area. To overcome this problem,

hydrogels can be imbedded in a rigid and porous matrix (membrane, etc) through cross-linking. The process is carried out in the support with in-situ polymerization and simultaneous cross-linking[35]. The cross-linked polymer chains are entangled within the porous matrix and lead to high stability. It should be noted that this technique is non-covalent modification and the performance of the membrane support highly depends on the concentration and loading amount of the hydrogel. The cross-linking provides the advantages of high stability, uniform distribution and high concentration of functional groups, but too much cross-linking also severely limits the movement of the polymer chains in the matrix resulting in mass transfer resistance.

1.2.3 Phase inversion for membrane fabrication

In the previous discussion, the method for fabricating the functionalized membrane is to modify the common and existed membrane to endow functions of membrane. Another method is to develop new membrane materials and structures including casting polymer solution in organic solvent to make the membrane. The formation of membrane includes phase inversion. Phase inversion technique is an extensively used method for prepare ultrafiltration membrane and most of microfiltration membranes. All the phase inversion membranes involve the precipitation of polymer from the polymer rich casting solution induced by solvent and non-solvent miscibility[36, 37]. The polymer creates membrane structure and the non-solvent makes pores. Thus, the parameters can affect the membrane morphology including: type of polymer, type of solvent, type of non-solvent, concentration of casting solution, temperature of

non-solvent, temperature of casting solution, evaporating time, and additives. The most commonly used polymer includes cellulose acetate, polyamide, poly(vinylidene fluoride) (PVDF) and polysulfone (PS). The solvent can be N,N-dimethylacetamide (DMA), N,N-dimethylformamide (DMF), N-methylpyrrolidone (NMP), dimethylsulfoxide (DMSO), acetone, etc. Water, ethanol and glycerol are used as non-solvent. In this study, PVDF membrane with sponge-like structure was fabricated with PVDF casting solution in DMF, water as non-solvent, polyvinylpyrrolidone and lithium chloride (LiCl) as additives.

1.2.4 Stimuli-Responsive material

Stimuli-responsive material, most of which are functional polymers, can adjust or modulate their physicochemical properties in response to an external stimulus. The environmental stimuli can be pH, temperature, light, electrical field, pressure, ions, chemical and biochemical compounds (such as, glucose et al.). The physical basis for this responsive behavior is the change of polymers conformation from a hydrating (hydrophilic) state to a dehydrating (hydrophobic) state, caused by a change of environmental conditions [38]. The changes are usually reversible and can go back to the initial state when the stimulus is removed. There are growing interest in recent years regarding the developing of functionalized membranes with responsive property by chemical modification. The introduction of porous membrane can be served as a delicate responsive partner. In this way, the permeation and mechanical properties can be independently approved within a large range of parameters.


Among these various stimulus, temperature and pH are most comment and widely used because they are easily designed and controlled. Thus, temperature and pH responsive membranes have gained special interest. These two kind responsive polymers will be discussed in details in the following sections. Other stimuli responsive polymers will also be discussed afterwards.

1.2.4.1 pH response

pH responsive polymers are polymers which can respond to the change of medium pH. As the pH changes, the degree of ionization of a polymer with weakly ionized groups (such as, $-\text{COOH}$) will be dramatically changed at a specific pH called pK_a , which induce the conformational change of polymer chains[38]. Table 1.1 shows several pH responsive polymers. Chitosan and collagen are two natural polymers with weakly ionized groups, $-\text{NH}_2$ and $-\text{COOH}$, respectively. Polyacrylic acid (PAA) is another most widely studied pH responsive polymer. At low pH below pK_a , the carboxyl groups are protonated, leading to the contract of the polymer chains. While, at higher pH over pK_a , the carboxylic acid groups are fully ionized, resulting in an expansion or swelling of the polymer chains[39]. When this response is immobilized in the porous membrane support, it can be used to modulate the permeation property of the membrane. For example, Mika et al. reported the synthesis of poly(4-vinylpyridine) onto MF membrane through UV-induced grafting method with outstanding pH sensitivity and the capability to reject small inorganic ions in the process of RO[40]. The response is directly related to the degree of polymer grafting. The introduction of PAA on the poly(vinylidene fluoride) (PVDF)

membrane has been applied to the separation of drugs[41] and controlled drug delivery[42].

Table 1.1. pH responsive polymers

Polymer name	pH responsive groups	pK _a	Reference
Poly(acrylic acid)(PAA)	-COOH	4.2-5.5	[43]
Polymethacrylic acid (PMAA)	-COOH	5.6-7.0	[44]
Poly(sulfoethyl methacrylate)	-SO ₃ H	1.5	[45]
Chitosan	-NH ₂	6.4	[46]
Poly[(N,N-dimethylamino)ethyl methacrylate]	-N(CH ₃) ₂	1.2	[47]
Poly(4-vinylpyridine)		3.9	[48]

1.2.4.2 Temperature responsive behavior

Temperature is the most widely utilized stimulus for responsive membranes because it's easy to control and easily applicable especially in drug delivery area. The unique property of temperature responsive polymers is the existence of either lower critical solution temperature (LCST), or upper critical

solution temperature (UCST). LCST is the temperature above which the polymer chain is separated from water due to the break of hydrogen bonds. While UCST is the temperature above which the polymer and solvent are miscible. Temperature responsive polymers can be derived from vinyl ethers, vinylcaprolactam and N-alkylacrylamides and ethylene oxide and propylene oxide monomers[49]. Among various temperature responsive polymers with LCST, poly(N-isopropylacrylamide) (PNIPAAm) with LCST at about 32°C is the most actively studied. At a temperature below LCST, PNIPAAm is fully hydrated (hydrophilic) due to the formed hydrogen bonds between amide groups and water. With the increase of temperature over LCST, the hydrogen bonds is broken, resulting in the collapse/shrink of the polymer. By combining this response with membrane, Akerman's group reported the 30 times increase of dextran permeability at temperature above and below LCST[50]. Besides the control of membrane pore size for the modulation of permeability due to the swelling and shrinking of PNIPAAm chains, the transition change (hydration and dehydration) can also be used to separate solute with different properties. Choi et al. has demonstrated the use of grafting PNIPAAm onto polypropylene (PP) to separate hydrophobic and hydrophilic solutes by temperature swing operation below and above LCST[51]. The schematic illusion of this novel separation process is shown in Figure 1.1.

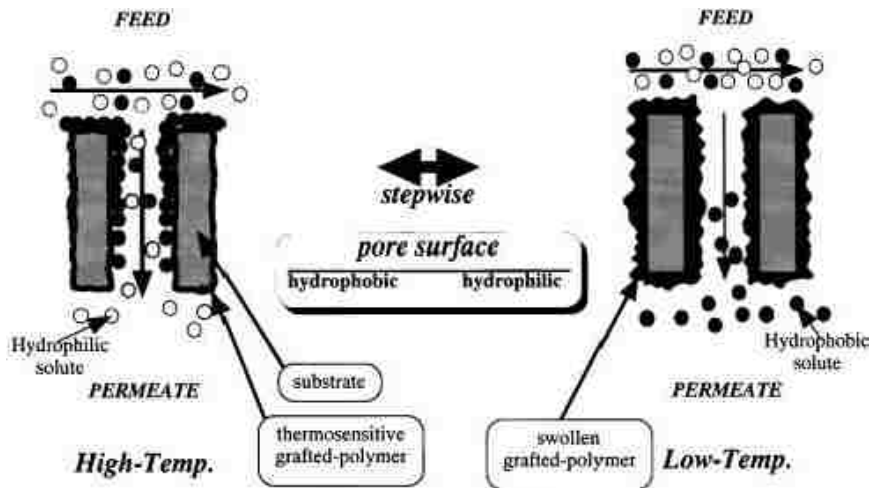


Figure 1.1. Schematic illustration of a novel separation system using temperature responsive NIPAAm grafted on PP membrane[51].

1.2.4.3 Other stimuli-responsive material

In addition to pH and temperature responsive polymers, light sensitive polymers can respond to UV light or visible light irradiation. The typical structure for light sensitive polymers contains double, triple bonds, or other conjugated interactions, such as azobenzene based, triphenylmethane-based and spiropyran based polymers[52]. The polymer hydrophilicity or surface wettability can be changed by irradiation induced phase transition through ionization, ring opening and cis-trans isomerization[53]. Chen's group reported the use of light responsive polymer to realize remote controlled drug delivery and cancer therapy[54].

Polymers with ionic charge groups can trigger the phase transition behavior by the modification of electric field, which have been applied in the bio-related area, such as drug delivery, artificial muscles[55, 56].

Glucose responsive polymers is based on the polymer-polymer or glucose-protein binding[57]. These polymers have received tremendous attention

recently due to their potential application in insulin-dependent diabetes[58, 59]. One example for glucose response is the combination of pH responsive polymer with glucose oxidase. The swelling and shrinking of the material is caused by the decrease of pH indirectly through the oxidization of glucose oxidase to gluconic acid[58]. Kost et al. reported the development of glucose responsive membrane by radiation polymerization for the potential application for an artificial pancreas with controlled insulin delivery[60]. However, the challenge for using glucose responsive polymer with glucose oxidase is the difficulty in maintaining the enzyme activity .

1.2.5 Functionalized membrane for nanoparticles synthesis

Our previous publications have reported the use of metal nanoparticles (NPs) to do water remediation for chloro-organic degradation to non-toxic compounds. The development of flexible and efficient remediation technology is of immense importance. The following sections will discuss the use of nanoparticles and the integration of nanoparticles and functionalized membranes.

Zero-valent nanoscale metal (especially iron) particles have been studied and implemented in groundwater remediation of chlorinated solvents through reductive pathways[61-64]. For a more rapid and complete reductive dechlorination, a second metal is added. In these systems, the first metal (most commonly Fe, but also Mg, Sn, etc) is an electron donor that generates hydrogen gas via a corrosion reaction to degrade the organic compound, and the second metal promotes the reactivity through hydrogenation, acting as a catalyst. Several bimetallic systems that are designed to dechlorinate toxic chlorinated

organic compounds have been reported in the literature, including: Fe/Cu[65, 66], Fe/Ni[67] or Fe/Pd[68-71]. Among these, the Fe/Pd bimetallic system are the most efficient and most commonly used system for dechlorination of various chloro-organics due to their low activation barrier[72]. However, due to their magnetic properties, NPs tend to agglomerate rapidly in water to form micron size or larger aggregates, thus reducing their dechlorination reactivity[73, 74]. Various techniques have been employed to control particle size, e.g., soluble dispersing agents such as polymers, surfactants or protective coating[75-77]; however, the use of polymers and surfactants as coating on particles may sacrifice the dechlorination reactivity. Thus recent interest focuses on the immobilization of NPs in other platform, such as, carbon, silica and crosslink polymers.

Among various supporting material, functionalized membranes provide a highly tunable platform due to its ease of functionalization and accessibility with charged groups (-COOH, -SO₃H, -OH) and control of pore size. In particular, membranes with open structure (such as PVDF and polyether sulfone (PES) microfiltration membranes) have the distinct benefits of high internal surface area and ease of access to the active particle site[78-80]. Moreover, the synthesis of metal NPs in functionalized membrane with environmental response (pH and temperature, etc)[81] may further allow the control of the microenvironment near the active reaction sites and reduces the loss of particles by recapturing the metal ions and thus may offer a increase of dechlorination reactivity. The

diffusion, mass transfer resistance, and pressure drop can also be eliminated by convective flow operation of membranes.

1.2.6 Nanofiltration

Nanofiltration membrane generally consist of negatively charged groups (COO^- , SO_3^{2-}) and/or positively charged (NH_3^+) groups within a relatively dense membrane matrix (with pore size less than 2 nm) by famous interfacial polymerization[82]. Due to this charged pore surface, NF can be effectively utilized to separate sugar, organic molecules, mono-valent and multi-valent salts based on both size and Donnan exclusion. Typically, NF membranes are characterized with low rejection of mono-valent ions, high rejection of divalent ions with higher flux than RO membranes[83]. Commercial available NF membranes is varied in characteristics such as pore size and surface charge, leading to various performance[84]. Thus, a lot of efforts have been devoted to develop appropriate NF membranes for selective separation of sugar from salts in food industry. Especially in some cases, lower divalent salt rejections while maintaining over 98% sucrose/lactose is highly desirable. Thus, minimization of surface charge through modification of interfacial polymerization process and coating technique are required in synthesis of NF membranes with high selectivity and high flux. In this work, full-scale modified NF membrane with less charge was developed and evaluated for the selective rejection of divalent salt and sugar mixture.

1.3 Objectives and outlines

The specific research objectives are:

- To synthesize temperature responsive P(NIPAAm-AA) hydrogel and membrane with ion exchange groups (-COOH) for metal ion capture and subsequent conversion to nanostructured zero-valent metal in the matrix (Chapter 2 &Chapter 3).
- To characterize the hydrogel, hydrogel nanocomposites and functionalized membranes with attenuated total reflectance-Fourier transform infrared (ATR-FTIR), scanning electron microscopy (SEM), thermogravimetric analysis (TGA), differential scanning calorimetry(DSC), atomic force microscopy (AFM) and x-ray photoelectron spectroscopy (XPS). (Chapters 2-5).
- To investigate the transition behavior via swelling study and model evaluation and demonstrate the hypothesis that the use of immobilized NPs in responsive hydrogel nanocomposite domain will allow highly effective PCB and TCE dechlorination by both reductive approach (Chapter 2).
- To develop both temperature and pH responsive membrane based on full-scale membrane to evaluate the feasibility of continuous manufacture of functionalized membranes and to demonstrate controlled and tunable separation through water, charged solute and uncharged solute (dextran) permeation study(Chapter 3).

- To modify PVDF membrane with alkaline solution to create double bonds for covalently grafting of polyacrylic acid; and to study the effect of treatment time on the membrane structure and morphology (Chapter 4).
- To fabricate the sponge-like PVDF membrane through phase inversion methods with high adsorption ability for metal ions (Chapter 4).
- To establish the nanofiltration membrane with selective separation of sugar and divalent salt; and to investigate the effects of sugar and salts concentration on the sugar rejection by model development(Chapter 5).
- To model the solutes (charged and uncharged) transport in the nanofiltration membranes for understanding the structure and electrical properties (Chapter 5).

Chapter 2 - Responsive Hydrogel-Supported Metallic Nanoparticles Synthesis and Water Remediation

2.1 Introduction

Hydrogels are hydrophilic polymer networks that can absorb a large amount of water but not dissolve in water[85-87]. Responsive hydrogels can undergo a swelling transition in response to environmental stimuli, such as the changes in temperature, light, pH etc[39, 88-90]. Due to this unique feature, responsive hydrogels have received extensive attention in the fields of drug delivery[38], bioseparation[91], sensors and optical transduction of chemical signals[42, 91]. For example, the drug release from responsive hydrogels can be remotely controlled by the local heating of magnetic nanoparticles[92-95]. The same concept has been transferred to the application in catalytic reaction, which is particularly attractive due to the unique tunable and responsive properties as well as the improvement of reactive properties[38, 42, 91]. Specifically, the swelling and deswelling of the hydrogel with temperature change can control the partitioning of reactants in the hydrogel network, which in turn changes the reactivity. Poly (N-isopropylacrylamide) (PNIPAAm) is one of the most common and widely studied temperature responsive hydrogels with hydrophobic and hydrophilic phase transition at a lower critical solution temperature (LCST) about 32°C[96-98]. Below the LCST, NIPAAm is hydrophilic and swells in aqueous media, while it becomes hydrophobic and collapses above the LCST. Attracted by these particular responsive properties with the change of temperature, PNIPAAm has been received considerable attention and has been successfully

employed as a support for the synthesis of metal nanoparticles and smart catalyst[99, 100]. For example, Lu et al. proved the adjustable catalytic reactivity with response to temperature change for Ag nanoparticles imbedded in PNIPAAm-b-PS core-shell systems[101]. This extend the use of hydrogel from biomedical field[102, 103] to environmental application by incorporating catalyst and responsive property.

One can also utilize the hydrogels in environmental catalysis (such as, organic pollutant degradation from water) if appropriate catalytic domain and selective reactant partitioning can be created. The quality of water has been always an important and demanding issue in the exploitation of natural water resources and remediation of contamination in recent years[2, 104]. Hydrogels has been reported to be used as is for fouling control in water treatment[105, 106]. In particular in the field of catalysis, we use this hydrogel immobilized nanoparticles for detoxification of organic chlorinated compounds from aqueous streams. Chlorinated organics such as trichloroethylene (TCE) and polychlorinated biphenyls (PCBs) are the most concerned water pollutants due to their high toxicity, persistence and various sources of distribution in environment[107, 108]. In recent years, the creation and development of nano-sized materials (iron) as a promising way for toxic chlorinated organics degradation and water pollution treatment have been widely studied and investigated[109-111]. Nanoscale metallic particles with high surface area and high binding energy of core electrons can enhance the interaction of the surface sites between the reactants and products[70, 112]. For more rapid and complete

degradation, a second element such as Pd, Pt, Ni, Cu and Ag was added as a hydrogenation catalyst[110]. Among these, Fe and/or Fe/Pd, and Fe/Ni, are the most efficient and commonly used system. However, Fe and/or Fe/Pd nanoparticles naturally tend to aggregate due to the magnetic properties, which may lead to the reduction of dechlorination reactivity[113, 114]. Thus, immobilization of nanoparticles has drawn great interests due to the increasing demand in controlling nanoparticle aggregation and reactivity. Specifically, stabilizers, ligands and membrane supports have been used to stabilize and immobilize nanoparticles[115, 116]. A common problem in using these supports is the sacrifice of nanoparticle reactivity. Moreover, the surfactant coating may hinder the diffusion of reactant to the surface of the nanoparticles, which may reduce the reaction rate. To overcome these problems and enhance the nanoparticles' performance, we proposed to use a temperature responsive P(NIPAAm-AA) hydrogel as a promising network support to immobilize metallic nanoparticles for toxic chlorinated organics degradation. Furthermore, for environmental catalytic applications, the synthesis of Fe and Fe/Pd NPs in temperature responsive hydrogels allows the control of the microenvironment near the active reaction sites to modulate the reactivity. Although immobilization of iron and other catalyst in membrane platform has been reported, to our knowledge, the membrane platform combined with both PAA for in-situ synthesis of nanoparticles, and potential tunable reactivity with temperature responsive PNIPAAm have not been published with Fe and Fe/Pd nanoparticles.

The main goals of the present study are: (1) to synthesize temperature responsive P(NIPAAm-AA) hydrogel with ion exchange groups (-COOH) for metal ion capture and subsequent conversion to nanostructured zero-valent metal in the matrix, (2) to characterize the swelling and partitioning of hydrogel and hydrogel nanocomposites, and (3) to test the hypothesis that the use of temperature responsive hydrogels will allow the modulation of reductive dechlorination reaction reactivity of toxic chlorinated organics with TCE and PCB as model compounds by altering pollutant partitioning and water content around reactive nanoparticles.

2.2 Experimental Methods

2.2.1 Materials

N-isopropylacrylamide (NIPAAm), acrylic acid (AA), poly (ethylene glycol) 600 dimethacrylate (PEG600DMA), 4-(4-Dimethylaminophenylazo) aniline (DMPA), Ethanol (>99.5%), ferrous chloride tetrahydrate ($\text{FeCl}_2 \cdot 4\text{H}_2\text{O}$), sodium borohydride (NaBH_4), sodium carboxymethyl cellulose (CMC, mean $M_w=90,000$ g/mol), and trichloroethylene (TCE) were purchased from Sigma-Aldrich (>99.5%). 2,2'-dichlorobiphenyl (DiCB), biphenyl (BP), 2-chlorobiphenyl were obtained from Ultra Scientific.

2.2.2 Synthesis of Crosslinked PNIPAAm-PAA Hydrogel

Three gram N-isopropylacrylamide (NIPAAm), 1 g acrylic acid, 0.207 g poly (ethylene glycol) 600 dimethacrylate (PEG600DMA) (molar ratio of NIPAAm: AA: PEG600DMA=80:10:10), 43 mg DMPA as initiator were added in a 20 mL vial and equal weight amount of ethanol were added, mixed them together

to get the uniform solution. The mixture was pipetted into two 15x15 cm² clamped glass plates with Teflon spacer to make the thickness to be 0.5 mm. UV polymerization was conducted for 5 minutes with 14.8 mW/cm² intensity. The hydrogel was carefully removed from the plates, placed in deionized water and washed daily [117]. The schematic of P(NIPAAm-AA) synthesis steps are shown in Figure 2.1.

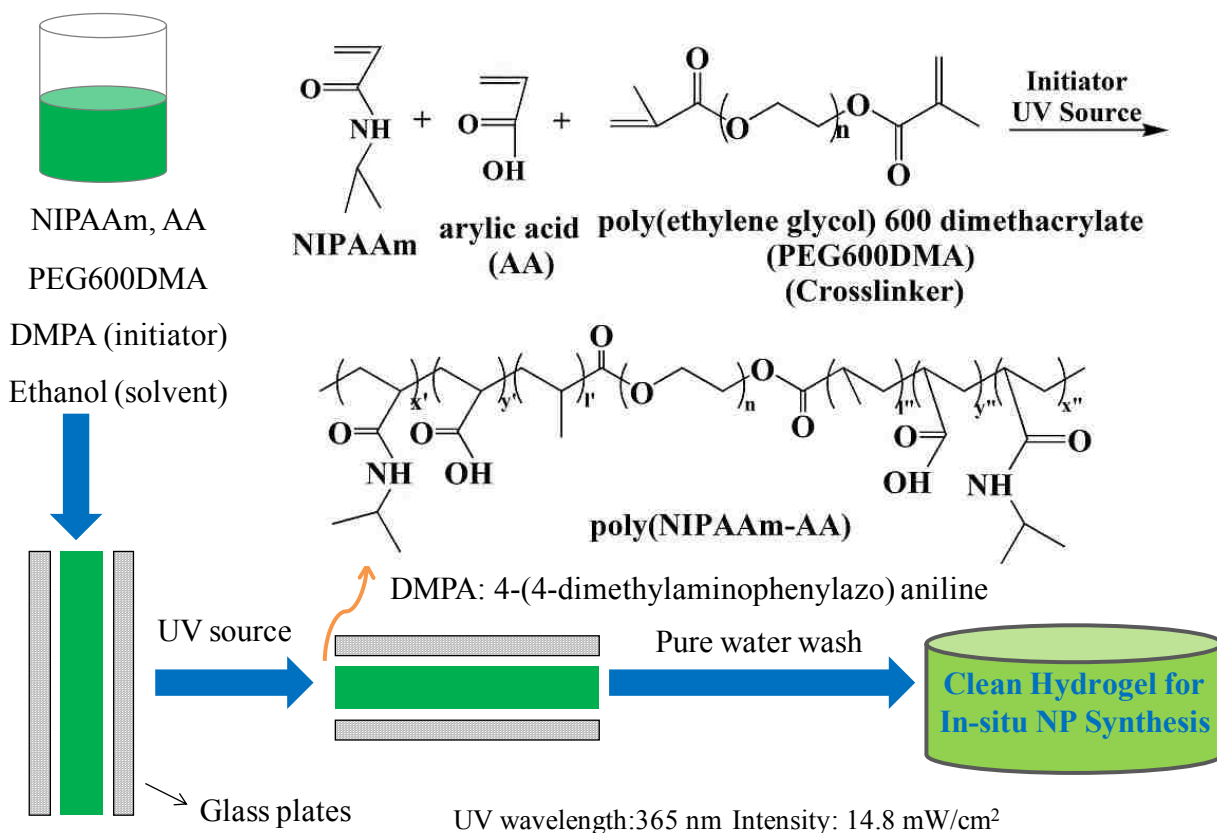


Figure 2.1. Schematic diagram of P(NIPAAm-AA) by UV photopolymerization

2.2.3 In-situ Synthesis of Nano-sized Iron Particles in Hydrogel Matrix

Fe⁰ nanoparticles were prepared by soaking hydrogel into the 200 mL 200 mg/l (as Fe) ferrous chloride solution with bubbling nitrogen for 4h. Then, the hydrogel was washed with deoxygenated DIUF water. The composite hydrogel

was then immersed into 200 mL 0.5M NaBH₄ aqueous solution for 2h. Fe²⁺ in the hydrogel network was reduced and immobilized inside the network which can prevent the aggregation of newly formed iron nanoparticles. The hydrogel was rinsed by a large amount of deoxygenated DIUF water to remove unreacted reactant, and was stored in ethanol. The schematic of Fe⁰ nanoparticles synthesized directly in hydrogel network are shown in Figure 2.2.

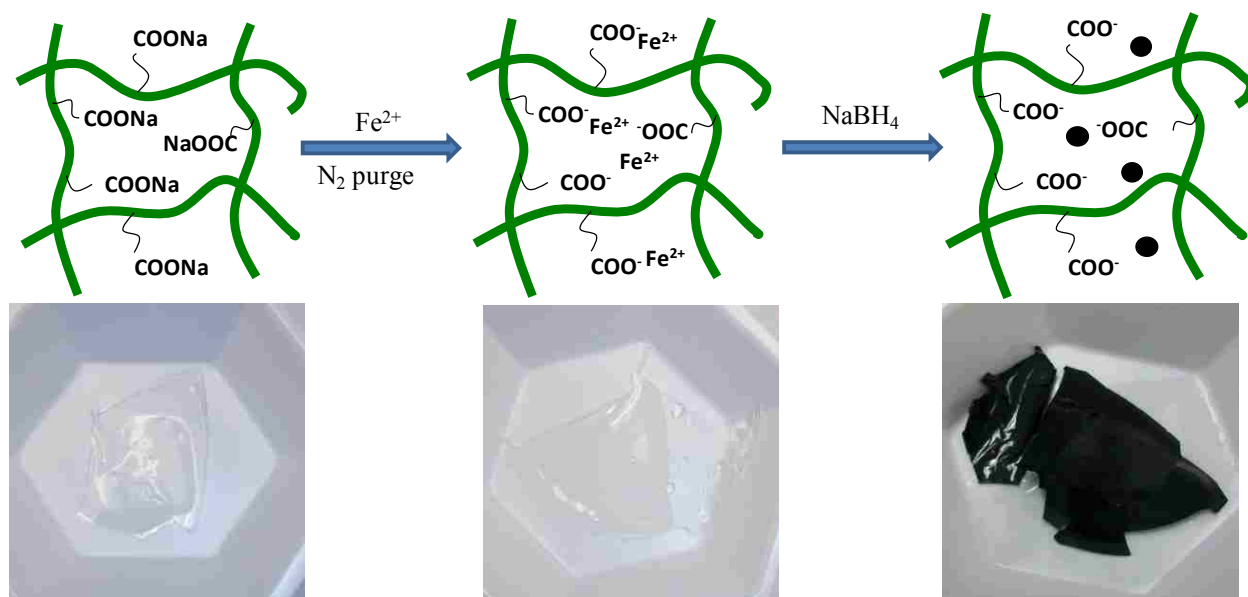


Figure 2.2. Schematic of direct formation of Fe⁰ nanoparticles in P(NIPAAm-AA) hydrogel network (upside) and the corresponding digital camera images (underside).

Fe⁰ nanoparticles encapsulated externally in hydrogel network were also prepared. The pre-formed iron nanoparticles (Fe⁰-CMC-1) (prepared by Zhao's method [118]) was mixed with monomer mixture by bath sonication and performed UV polymerization. The hydrogel nanocomposites were washed with deoxygenated DIUF water for several times and stored in ethanol.

2.2.4 Characterization of Fe⁰ Nanoparticles and Hydrogel Nanocomposite

Surface area (BET area) of the nanoparticles was measured by collecting nitrogen sorption isotherms at 77K via the Micromeritics Tristar 3000. The pore volume and pore size distribution were calculated with Tristar 3000 V 4.02 software using the BJH method. Prior to the measurements, the nanoparticles were dried at 120°C for 10 h under a flow of nitrogen.

Surface and cross-section of hydrogel containing Fe⁰ nanoparticles were examined by Hitachi S-4300 Scanning Electron Microscope (SEM). Hydrogel were coated with gold for imaging purposes.

2.2.5 Measurements of Swelling Ratio under Different Temperature

The weight swelling ratio was determined by gravimetric method [119] at different temperature ranging from 15°C to 50°C. At each particular temperature, the dry weight of hydrogel disk was measured. This sample was immersed in water bath for 24 h, wiped by fiber tissue to remove excess water on the surface, and weighed until the equilibrium was achieved. The weight data was an average from three samples. The swelling ratio was calculated as follows:

$$Q = \frac{W_s}{W_d} \quad \text{Eq. 2-1}$$

where W_s is the weight of hydrogel at swelling state, and W_d is the weight of hydrogel at dry state.

2.2.6 Hydrophobicity and Hydrophilicity Transitions of Temperature-Responsive Hydrogel Measured by Model Organic Partitioning Experiments

The hydrogel hydrophobicity and hydrophilicity was investigated by two different dyes: methylene blue and orange II, which are two widely used dyes for study the transition of temperature responsive polymer due to their different hydrophilic character. 0.01 mmol/L methylene blue and orange II aqueous solution was prepared in advance. The hydrogels were immersed into 20 mL of the two solutions respectively at different temperatures for 24 h. The concentrations in solution phase before and after the immersion were measured by UV-Vis spectroscopy with the reading of wavelength at 664 nm for methylene blue and 486 nm for orange II [120, 121]. The partitioning coefficients (K_i) at different temperatures were calculated based on the initial and final concentrations of these two dyes. The partition coefficient (K_i) was defined as the ratio of the dye solubility in hydrogel and solubility in water.

2.2.7 Adsorption Experiment

In order to determine the adsorption capacity of P(NIPAAm-AA) hydrogel for TCE, as well as the effects of temperature, experiments were performed by batch equilibrium technique. A typical experiment was conducted in a 43-mL serum vials containing 0.47g (dry weight) of hydrogel. At selected time, 2 mL sample was taken out and 2 mL pentane was added to extract TCE. GC-MS was used to measure the TCE concentration in the solution.

2.2.8 Dechlorination by Fe/Pd Nanoparticles in P(NIPAAm-AA)

Hydrogel

Batch dechlorination experiments of TCE and DiCB were conducted in 43 mL serum glass vials. Fe or Fe/Pd NPs immobilized in a P(NIPAAm-AA) hydrogel were loaded into the vial containing 30 mg L⁻¹ TCE in 43 mL deoxygenated water. For DiCB, the feed concentration is 5 mg/L in 43 mL 50:50% ethanol:water mixture. Both experiments were also carried out at 30°C and 34°C to investigate the reactivity tunability. All the serum glass vials were sealed with Teflon-lined silicon septa and placed on a wrist-action shaker throughout the duration of the experiment. Parallel control experiments with only hydrogel (no metal nanoparticles) were also performed. TCE analysis was performed using a gas chromatograph (GC, Varian-3900) equipped with an ion-trap mass spectrometer (MS, Saturn-2100T). Two mL of pentane as the extractant for TCE was added to an 8 mL vial containing 2 mL of aqueous solution which was taken from the reaction vial. The vials were placed on the shaker to mix for 2 hours to achieve extraction equilibrium. For each extracting vial, 1 micro liter solution in the extracting solvent phase was removed and injected into the GC sample column for analysis. 1, 2-dibromoethene was used as an internal standard. The TCE calibration curves were created using 7 concentrations ranging from 5 to 50 mg L⁻¹ with R² = 0.999 and average analytical error of 5%.

For PCB analysis, the samples were extracted with hexane (volume ratio=1:1) with the addition of external standard, naphthalene-d8. For each extraction vial, a 1 mL aliquot of the extraction solvent were transferred into 1 mL GC autosampler for analysis with a Varian CP-3800GC coupled with a Varian

Saturn 2200 MS. External standards of DiCB, 2-chlorobiphenyl and biphenyl in hexane (Ultra Scientific) were used to prepare calibration curves. The calibration curves were linear over the concentration range from 0.5 to 10 mg/L with $R^2 > 0.999$ and analytical error less than 2%.

2.2.9 Chloride Analysis

The concentration of chloride ion as the main product of TCE degradation in aqueous solution was measured by the Orion 94-17 Solid State half-cell and Orion 96-17 iron plus Sure-Flow with Chloride Electrode. In all cases, the instrument calibration was based on commercial standards (Fisher Scientific) containing 1000 mg/L of the chloride with $R^2 = 0.994$ and an average analytical error of 3%. 2% (volume) of sodium nitrate (LabChem Inc., 5mol/L) was added into the samples as the Ionic Strength Adjuster (ISA) to ensure the same ionic strength.

2.2.10 Metal Analysis

The amount of Fe captured during ion exchange and the amount of Pd in the hydrogel were quantified by using a Varian SpectrAA 220 Fast Sequential atomic absorption spectrometer equipped with a Fisher Scientific hollow cathode lamp. For Fe, the lamp was operated at a wavelength of 386.0 nm. The calibration plot was created using 4 different concentrations of Fe ranging from 25 to 200 mg/L with $R^2 = 0.9998$ and an average analytical error of 2%. In the case of Pd, the lamp was operated at a wavelength of 246.6 nm and the linear calibration range was between 0.2 and 28 mg/L Pd. The error of analysis was < 2% with $R^2 = 0.9996$.

2.3 Results and Discussion

2.3.1 Synthesis of P(NIPAAm-AA) hydrogel

The synthesis of both free radical redox and photo polymerization of NIPAAm hydrogel with PAA has extensively reported in the literatures [122-124]. Our work is to create hydrogel along with ionizable groups such as: carboxylic groups to adsorb metal ions for post reduction with reduce agent to form nanoparticles for catalysis. This brings in catalytic aspects domain which is an important area particularly environmental area. This section addresses specific aspects of the UV based polymerization steps.

Hydrogel network is the key point for the in-situ formation of nanoparticles with both size control and shape control. Various parameters can affect the network structure, for example, the type of monomers chemistry, the ratio between two different monomers, the solvent, and the type and amount of cross-linker. PEGDMA with different ethylene glycol chains is a widely used cross-linker[125, 126]. Here, PEG600DMA was selected as the cross-linker due to formation of flexible network with better diffusional characteristics[126]. The synthesis flowchart for the P(NIPAAm-AA) hydrogel and the corresponding mechanism are shown in Figure 2.1. It should be pointed out that the thickness of hydrogel can be easily changed by adjusting the spacer thickness. The first stage was to characterize the polymerization steps by using ATR-FTIR. From the ATR-FTIR spectra as shown in Figure 2.3, the peak at 1720 cm^{-1} is assigned to the C=O group in AA, and the peak at 1650 cm^{-1} belongs to the overlapping of NIPAAm and AA ranging from 1610 cm^{-1} to 1660 cm^{-1} . The band at 1550 cm^{-1} is

assigned to the N-H vibration of NIPAAm[96]. The appearance of these peaks in the P(NIPAAm-AA) hydrogel demonstrates the successful copolymerization of NIPAAm and AA. Figure 2.4A and B show the SEM image of P(NIPAAm-AA) surface and cross-sectional structure. Clearly, the hydrogel shows a porous structure which is beneficial for the increase of accessibility towards the immobilized metallic nanoparticles. In this paper, AA was utilized to pick up iron ions and therefore immobilize metallic nanoparticles into the hydrogel network. The thermo-sensitive NIPAAm segments can swell and deswell reversibly, which can in turn adjust the concentration of toxic organics and the immobilized nanoparticles in the hydrogel matrix that can modify the reduction reaction[101]. Furthermore, the swelling/deswelling facilitates the regeneration and the reusability of nanoparticles. It's reported that when the temperature is raised above LCST, the hydrogel containing catalyst becomes dehydrated and it's easy to be removed from solution and recycled for the next cycle[127].

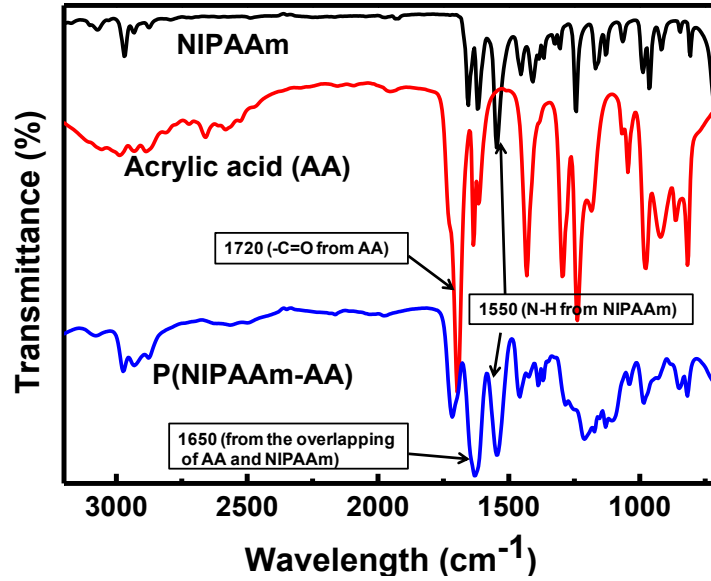


Figure 2.3. ATR-FTIR spectra of P(NIPAAm-AA) hydrogel, NIPAAm and AA monomers. The percentage of transmission scales varied in the range 100-10%.

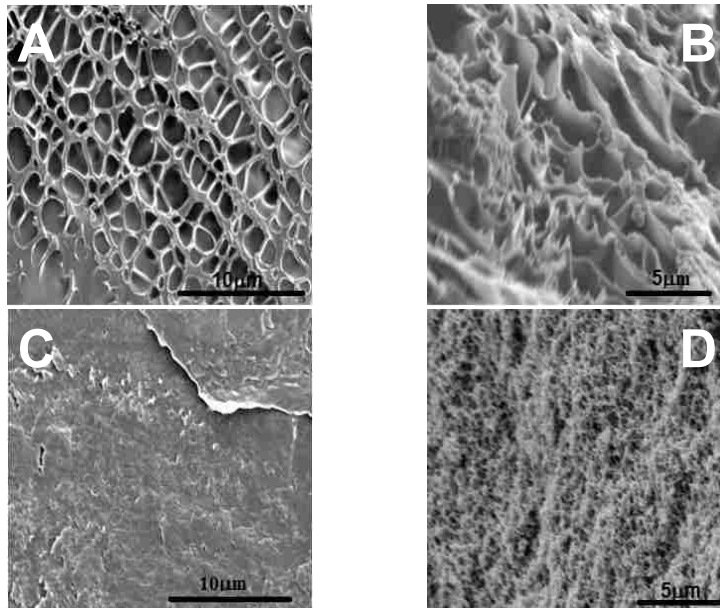


Figure 2.4. SEM images of hydrogels after reaching swelling equilibrium at pH 6.5 below LCST at 25°C (A and B: surface and cross-sections, respectively) and above LCST at 40°C (C and D: surface and cross-sections, respectively).

2.3.2 Synthesis of Reactive Fe Nanoparticles in P(NIPAAm-AA) Hydrogel

As reported, the metal ion can also be bonded to the nitrogen atom from amide group in NIPAAm chain but with lower affinity to ferrous ions[128]. Thus, in our work, free –COOH groups from PAA segment in the hydrogel was utilized to ion exchange metal ions for post reduction by reducing agent. It has been reported that one ferrous ion can be complexed with two –COOH groups[129]. The mass balance of ferrous ions was calculated based on the atomic adsorption spectrometer (AAs) analysis of the FeCl₂ solution before and after the loading of Fe²⁺ in the hydrogel. Assuming all the acrylic acid was polymerized in the final co- polymer, so the amount of acrylic acid should be 0.9 mmol for per gram of dry hydrogel weight. Base on this number, assuming all carboxylic groups are ionized and can be complexed with Fe²⁺, the ration of Fe²⁺ to –COOH should be 0.5. Based on the results from AA analysis, our experimental value is 0.6, which is quite reasonable. The exchanged metal ions were reduced with NaBH₄ to form Fe nanoparticles. Correspondingly, the color of hydrogel changes from white to black due to the formation of Fe⁰ nanoparticles inside the hydrogel network as shown in the corresponding digital photos in Figure 2.2. The total iron amount was obtained by analyze the Fe concentration before and after permeation. To check the material balance, the reduced Fe NPs was also digested by 20wt% nitric acid and analyze the Fe concentration by AAs. According to the AAs analysis results, a 94% yield of Fe nanoparticles was achieved after the reduction of bound Fe²⁺ with NaBH₄. This value agrees well with the established PAA metal binding stability constant.

It is worth noting that the formed Fe nanoparticles may have an oxide layer on the surface even for the freshly made and nitrogen protected nanoparticles. Literature[130, 131] data have demonstrated the formed nanoparticles always contain a core-shell structure with Fe nanoparticles as core and oxide as shell by spectroscopy and electrochemistry, but these nanoparticles are still very reactive and can be used for toxic organics degradation according to the results of the reductive reaction study. Actually, these oxide shells impart some stability to these Fe nanoparticles in solution phase, because the nanoparticles are very easy to aggregate in solution to form cluster leading to the decrease of reactivity. Therefore, the hydrogel network in this work is chosen to prevent the oxidation and aggregation of the nanoparticles.

For comparative purposes, Fe⁰ nanoparticles immobilized in hydrogel by encapsulation of preformed nanoparticles were also prepared. As shown in the SEM images, Fe⁰ nanoparticles directly synthesized in the hydrogel (Figure 2.5A) are roughly spherical with a homogeneous distribution and an average size of about 40 nm which was smaller than those encapsulated in a hydrogel network (100 nm) (Figure 2.5B). By using this method with PAA metal ion binding followed by reduction, iron nanoparticles can be created with uniform distribution inside the matrix, which can prevent the migration and nanoparticles aggregation. This is important in stabilizing the nanoparticles and controls the size of particles[132].

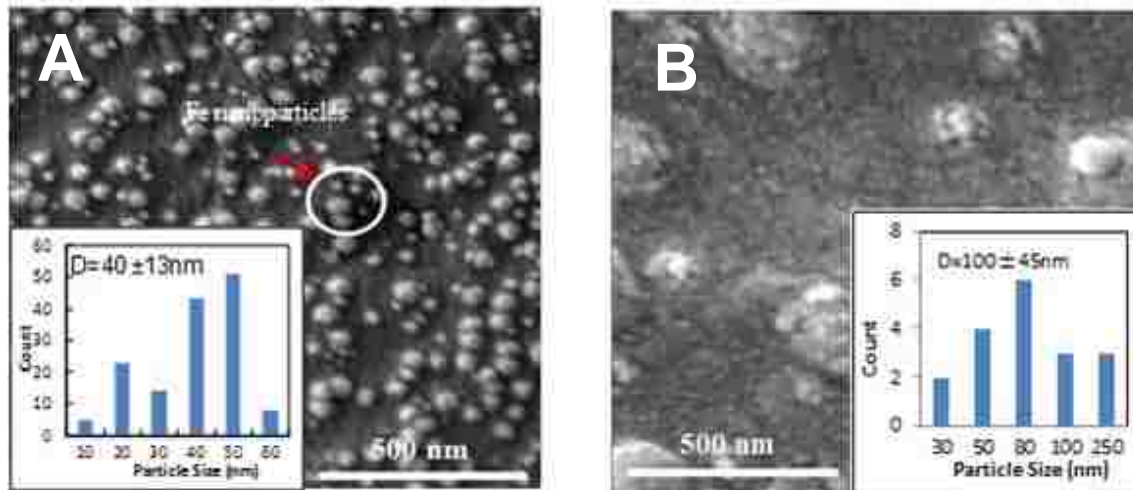


Figure 2.5. SEM images of Fe⁰ nanoparticles immobilized in P(NIPAAm-AA) hydrogel. A-Fe⁰ nanoparticles immobilized in hydrogel by *in-situ* synthesis; B-Fe⁰ nanoparticles immobilized in hydrogel by encapsulation.

2.3.3 Swelling Study of Temperature Responsive P(NIPAAm-AA) Hydrogel

Swelling/shrinking in water by temperature change is a unique feature of hydrogel, and has been widely studied by many researchers [133, 134]. The driving force of swelling/shrinking below and above volume phase transition temperature is usually considered to be the formation of hydrogen bonds with water and the hydrophilicity and hydrophobicity transition which is controlled by the property changes of side chain of NIPAAm[96-98]. This work takes the advantages of swelling/shrinking feature of hydrogel to manipulate the reduction of toxic organics by controlling the water content in the hydrogel network.

For better understanding of the swelling behavior, the polymer solvent interaction parameter, χ_p was calculated using Peppas-Lucht Model for cross-linked polymer system[135, 136] as following:

$$\chi_p = \frac{\left(\frac{1}{2}\Phi_p - \Phi_p^{1/3}\right)\left(1 + \frac{\nu^0 M_r \nu}{\lambda} \Phi_p^{1/3}\right)^2 - \frac{1}{\nu^0 V_{H_2O}} \left(1 - \frac{\nu^0 M_r \nu}{\lambda} \Phi_p^{2/3}\right)^3 (\ln(1 - \Phi_p) + \Phi_p)}{\frac{1}{\nu^0 V_{H_2O}} \Phi_p^2 \left(1 - \frac{\nu^0 M_r \nu}{\lambda} \Phi_p^{2/3}\right)^3} \quad \text{Eq. 2-2}$$

$$\frac{1}{\Phi_p} = 1 + \frac{W_s \rho_p}{W_d \rho_s} \quad \text{Eq.2-3}$$

Where Φ_p is the polymer repeat unit volume fraction in the swollen state; V_{H_2O} is the water molar volume (18 cm³/mol); λ is the number of links of repeating unit; M_r is molecular weight of repeating unit; ν^0 is the cross-linking density (mol/cm³); ν is specific volume of the polymer; W_s and W_d are the weights of absorbed solvent and dried hydrogel, respectively; ρ_p and ρ_s are the densities of dried polymer and solvent, respectively (1.0 g/cm³ for ρ_s ; and 1.1 g/cm³ for ρ_p [137]). W_s at different temperatures is obtained from the difference between the weight of swollen hydrogel and dry hydrogel. Then Φ_p at different temperatures are calculated based on **Eq. 2-3**. Assuming every monomer can cross-linked and then λ will always be 1. Moreover, the NIPAAm monomer can be assumed to attach to one AA monomer. Thus the repeat unit for the network is defined by:

$$M_r = M_r^{NIPAAm} + M_r^{AA} \quad \text{Eq. 2-4}$$

Thus M_r is calculated to be 185 g/mol. χ_p describes the free energy change by mixing and the values are shown in Figure 2.7. As the temperature increases, χ_p is increased from 0.57 to 0.71, which is less than the reported value larger than 1 for PNIPAAm [137] because the introduction of more hydrophilic PAA chain providing more compatibility with water. The increase of χ_p indicates the decreased swelling degree, which means poorer solvent for the polymer.

Water plays an important role in the reduction of toxic organics by Fe nanoparticles because it can facilitate the corrosion of the Fe to provide hydrogen and electrons which can be utilized to replace chlorine in the reduction of toxic chlorinated organics[129]. But too much water may oxidize the nanoparticles and decrease the reactivity. So by utilizing the swelling/shrinking feature of temperature responsive hydrogel, water content in the hydrogel network can be modulate, which in turn can tune the toxic chlorinated organics reduction reaction.

The preliminary swelling ratio of the hydrogel at different temperatures was investigated to study the water content in the hydrogel matrix as shown in Figure 2.6. The swelling ratio decreases with the increasing of temperature. The observed water content decrease in hydrogel at higher temperatures is consistent with the phase change behavior. In addition, the presence of nanoparticles in the nanocomposite hydrogel does not appear to have significant effects on the swelling ratio, which may be because of the free space left after

the *in-situ* reduction of nanoparticles[99]. For complete degradation of TCE ($C_2HCl_3 + 4Fe^0 + 5H_2O \rightarrow C_2H_6 + 4Fe^{2+} + 3Cl^- + 5OH^-$)[118], the minimum water amount for complete TCE dechlorination (30mg/L, 40mL) was calculated to be only 0.8mg, and the excess water may cause the iron corrosion ($Fe^0 + 2H_2O \rightarrow Fe^{2+} + H_2 + 2OH^-$) and less reactivity. Therefore, by utilizing the temperature responsive hydrogel, the water content can be properly adjusted and modulate the reaction.

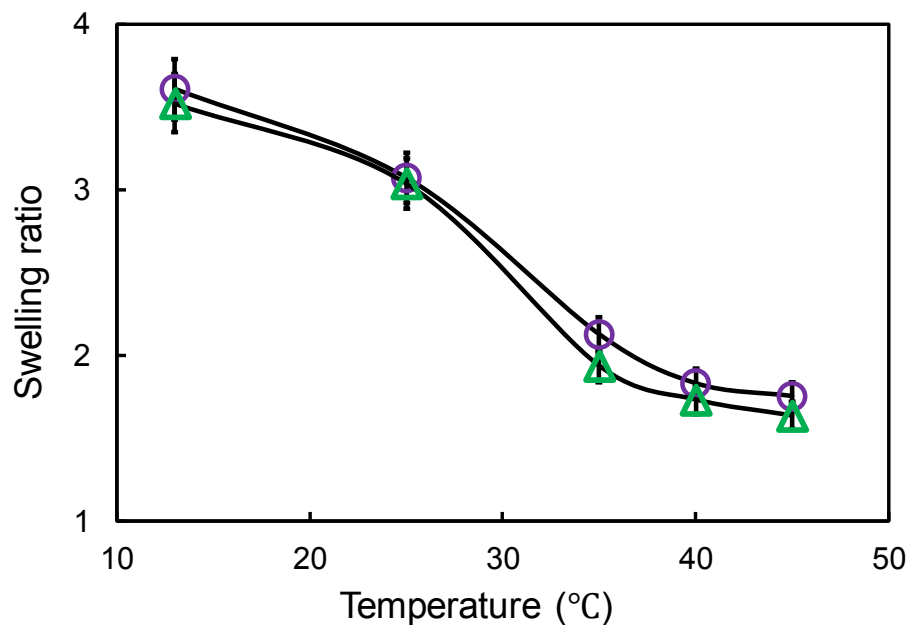


Figure 2.6. Swelling ratio of different systems at different temperature. Circles: blank P(NIPAAm-AA) hydrogel without any nanoparticles; triangles: P(NIPAAm-AA) hydrogel with 0.95wt% nanoparticles by in-situ synthesis (dry weight: 0.2 g; pH at 25°C: 6.86)

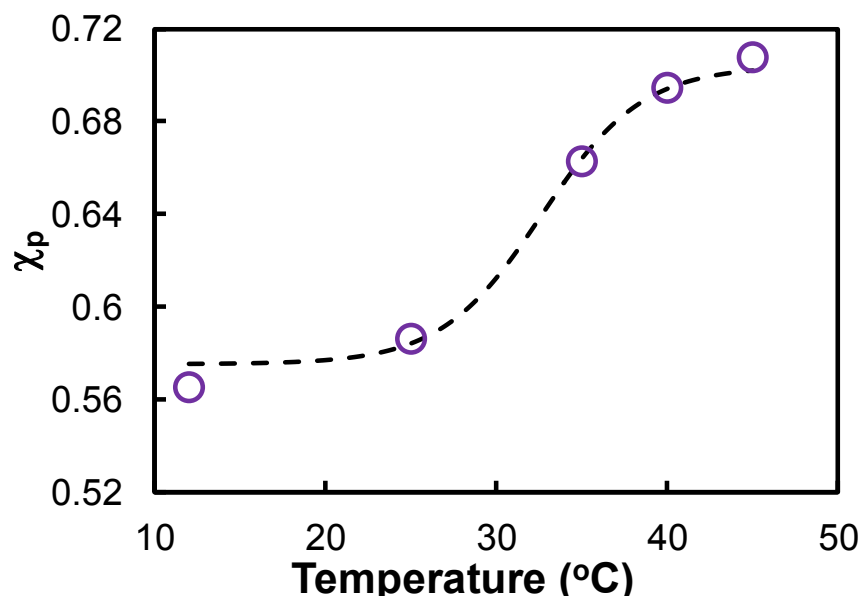


Figure 2.7. Variation of polymer solvent interaction parameter (χ_p) with different temperatures. The values were calculated using Eq. 2-2.

2.3.4 Establishment of Hydrophobicity and Hydrophilicity Transitions of Temperature Responsive Hydrogel by Model Organic Partitioning Experiments

For catalytic important material, molecule transport in hydrogel is important and only can occur in the confined space within the polymer chain[138, 139]. And thus, any factors that can reduce this space size, like hydrophobicity and hydrophilicity transition, would also affect the movement of molecule through hydrogel network. Thus it is important to establish quantitatively the role of hydrophobicity and hydrophilicity of hydrogel. For such purpose, partition coefficient (K) defined as the ratio of solubility in hydrogel and in water phase, was determined through the use of two model compounds: methylene blue and orange II[120, 121]. These two compounds have similar molecular weight, which can minimize the effects of the molecular size on the affinity with the hydrogel. The comparison of the two structures indicates that orange II is more hydrophilic

than methylene blue due to the facile formation of hydrogen bonds in the orange II molecule[120, 121]. The rise of solubility of methylene blue in swollen hydrogel was observed when the hydrogels were heated from 10°C to 45°C (Figure 2.8A), while the orange II shows opposite solubility change behavior (Figure 2.8B). Such observation is consistent with the phase change of temperature responsive segment NIPAAm. When the temperature increases, the existence of NIPAAm makes the network to change from hydrophilic to hydrophobic, during which the diffusion of orange II is reduced by the non-polar groups and in turn, and the solubility decreases.

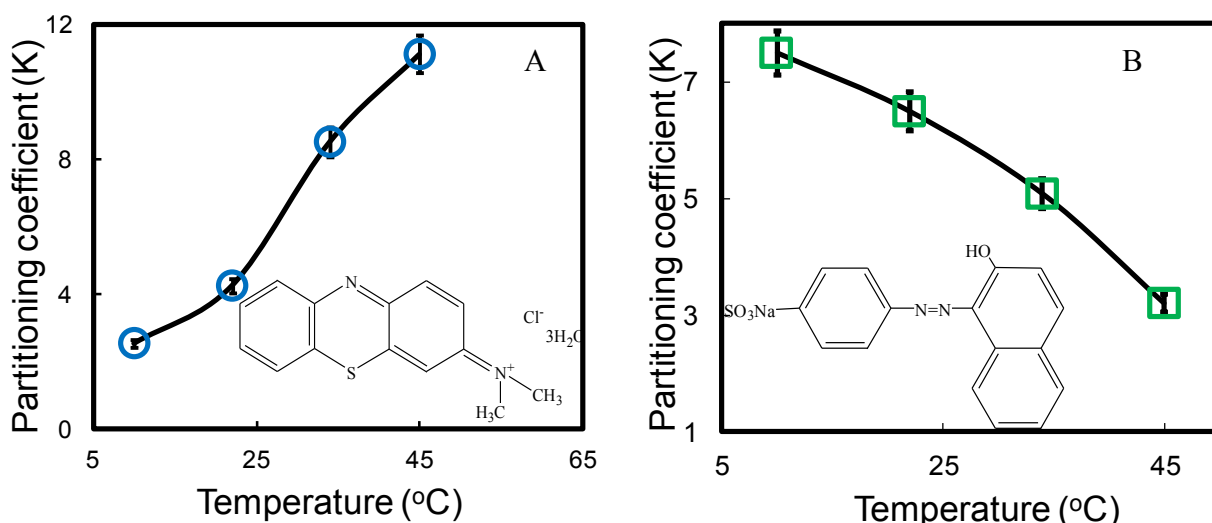


Figure 2.8. Partitioning coefficients (K) of methylene blue (A) and orange II (B) as a function of temperature through P(NIPAAm-AA) hydrogel (pH=6.5). The insets are the molecular structures of methylene blue and orange II.

2.3.5 Reductive Reaction by Hydrogel Immobilized Nanoparticles

The model compound utilized for reductive reaction is a well-known pollutant in ground water, trichloroethylene (TCE), and the objective of this reductive transformation is to exchange Cl with H, which is commonly referred by

environmental literature as dechlorination. It is well known that the reductive reaction by Fe nanoparticles is through electron transfer mechanism which are generated from Fe^0 corrosion; while in the Fe/Pd bimetallic system, H_2 was generated by Fe corrosion and Pd acts as a catalyst (the dechlorination occurs on Pd surface)[114, 140, 141]. The reductive degradation of chlorinated organics with zero valent metallic nanoparticles is a heterogeneous reaction, which include the adsorption of TCE on the particles surface, surface of reaction and desorption[129]. As a reactant, TCE concentration can affect the reductive reaction. Our previous work has established a mathematical model to study the transport of the reactant (such as TCE) to the reactive sites by adsorption and demonstrated that the surface TCE saturation has no effect on the reaction mechanistic pathways[112]. The Langmuir-type quasi-sorption isotherm model in this literature was utilized to study the TCE adsorption and the effects of TCE concentration on the degradation reaction. The result shows at the higher TCE concentration (500 mg/L), the total surface of nanoparticles covered by TCE molecules has reached a saturation, and there is no more available sites for TCE adsorption. However, in our work, dilute TCE feed concentration (30 mg/L) was used for environmental application and the iron loading concentration is higher than the theoretical requirement is considerably higher than the theoretical requirement, so the complete degradation of TCE would be expected.

The dechlorination performance for Fe^0 nanoparticles immobilized in a hydrogel network is shown in Figure 2.9. Most of the bound chloride was converted to Cl^- . Some points were taken in duplicate, which shows a good

reproducibility and stability (no nanoparticle deactivation observed). The reductive degradation rate in batch system can be described by the pseudo-first-order model [112]: $dC/dt = k_{obs}C = k_{SA}\alpha_S\rho_m C$, where “ α_S ” is the specific surface area of the nanoparticles (m^2/g) and ρ_m is the nanoparticle loading (g/L). In order to get better comparison of reaction rate under different conditions, the surface area normalized reactivity was calculated and the result is shown in Figure 2.9. Logarithmic values of TCE concentrations are plotted versus time and best linear fit values of the k_{SA} can be obtained by using the experimental degradation results. Assuming discrete spherical particles with a diameter of 40 nm, as observed from SEM image, α_S was calculated to be $20m^2/g$. Based on these assumptions, the calculated k_{SA} values for the nanoparticles for DIUF water dechlorination were determined to be $0.0066 L/m^2h$ for *in-situ* synthesized Fe^0 in P(NIPAAm-AA) hydrogel and $0.0036 L/m^2h$ for Fe^0 encapsulated in hydrogel as shown in Figure 2.9. In this case, the concentration of chloride, the only product of reduction reaction was also measured to determine the reactivity. In case of complete TCE degradation, 1 mole of TCE degraded can yield 3 mole of chloride. The chloride balances were defined as the ratio of detected chloride ($[Cl^{-1}]$) over the theoretical formation of chloride ($[Cl^{-1}]_{max}$) calculated from the TCE degradation data. The formed chloride balances obtained in the above systems were about 90%. The chloride loss can be explained by the sorption of chloride ions on to hydrogels and nanoparticles [129, 141]. Beside the deactivation by iron hydroxide formed on the metal surface without hydrogel matrix, the reaction rates difference is probably due to the small and uniform particles directly formed in the

matrix. Nanoparticles without any polymer support may cause excessive aggregation of metal atoms. Since TCE degradation rates highly depend on the total surface area of metal particles[115], the excessive aggregation of particles in solution phase and in hydrogel phase by external encapsulation may cause less surface area or loss of the available reactive sites which results in the decrease of k_{SA} . Also, the more free spaces left after direct reduction within the networks may facilitate the transportation of TCE inside the hydrogel network and as well as enhance the reaction on the reactive sites of the nanoparticles[112]. It is also important to mention that during TCE degradation, the Fe^{2+}/Fe^{3+} ions that are formed from the reactant Fe^0 are recaptured by the carboxylic acid groups from acrylic acid. This not only can prevent the formation of precipitate that can inhibit the dechlorination reaction, but also make it easy for recovered ions to be regenerated to the metal form[116]. In contrast to the homogeneous phase nanoparticles applications, our approach has negligible loss of iron to solution phase. Besides sodium borohydride, a highly reactive reducing agent, other natural and non-toxic materials can replace $NaBH_4$ as green reducing agents, for example, vitamins, amino acid, plant surfactants and green tea extract[142, 143]. Our group has reported the utilization of green tea extract for TCE dechlorination with reactivity ranging from 0.005 to 0.01 L/m²h[144]. The tea extract contains a lot of phenols acting as both dispersive and capping agents to minimize the nanoparticles oxidation and aggregation. The direct comparison of reactivity for borohydride and tea extract reduced nanoparticles is not appropriate due to the different reaction mechanism. For borohydride reduced nanoparticles, the

reaction involves both mass transfer and reaction on the surface. While for polyphenols reduced nanoparticles, the effect of reaction is more dominant than mass transfer[144]. Thus, A trade-off between the higher reactivity and larger longevity of nanoparticles should be taken into account.

In addition, TCE degradation was also conducted with sample water from a contaminated site in Paducah, KY containing 82 mg/L alkalinity, 293 mg/L total dissolved solids and 1.2 mg/L turbidity. The detailed water quality analysis was reported in literature[145]. As shown in Figure 2.9, the difference of degradation results between DIUF and sample water was within 2% for the same feed TCE concentration, which indicates the insignificant impact of hydrogel network on dechlorination in the contaminated sites. This also demonstrates that our system can be applied to the real world. It should be noticed that control experiments were also conducted to prove that TCE evaporation and physical adsorption in hydrogel has no effects on the TCE degradation. The whole hydrogel was extracted with pentane and no TCE detected by GC-MS and also, the TCE concentration was within 10% of the original value, which can prove that TCE concentration decrease during dechlorination studies is completely due to reaction with Fe nanoparticles.

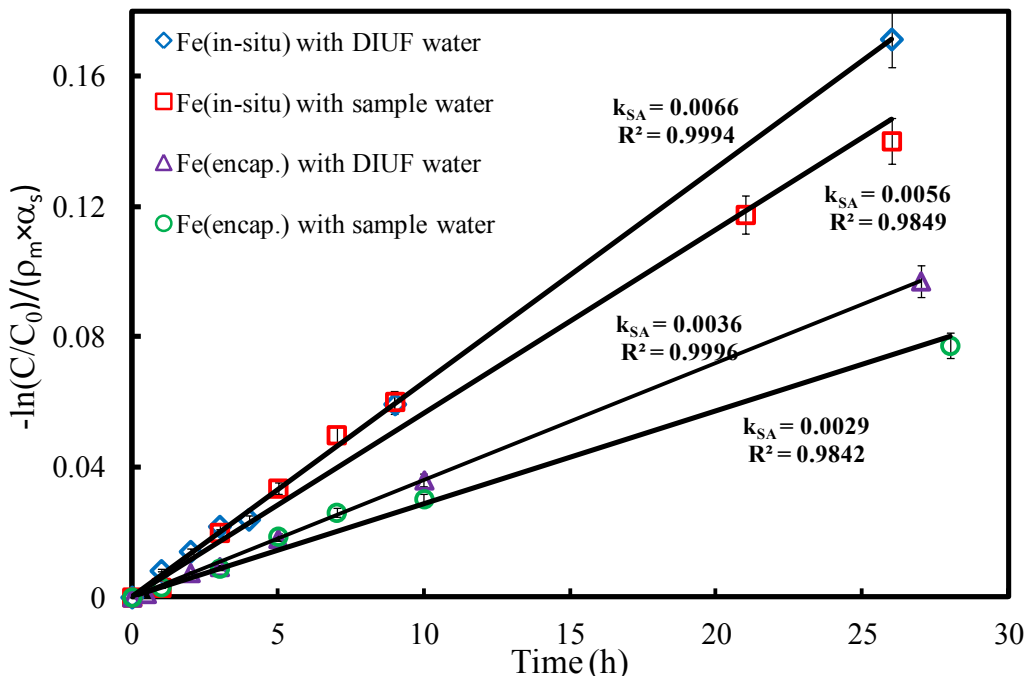


Figure 2.9. TCE dechlorination of deionized ultra-filtered water (DIUF) and “real” water (Paducah, KY) with Fe nanoparticles in-situ and encapsulated in P(NIPAAm-AA) hydrogel. Vol. = 43mL, initial pH: 7 (for DIUF) and 7.5(for real water); initial TCE concentration: 30 mg/L, iron loading amount: 1g/L; Temperature: 25°C.

2.3.6 Role of Temperature Responsive Behavior

There are extensive literatures on the role of temperature on the catalytic behavior of Fe and Fe/Pd on various degradation reactions[146-148]. On the other hand, the simultaneous role of hydrophilic and hydrophobic domain with the temperature change in hydrogel along with reactivity is a new area. The reaction rate discussed here is the overall reaction rate including the intrinsic reaction rate and adsorption rate of TCE to reactive sites of nanoparticles[70, 116].

TCE adsorption on reactive sites can be achieved by transfer in aqueous phase or diffusion in hydrogel matrix[129]. TCE diffusion rate in hydrogel matrix is higher than the rate in aqueous phase because of the enhancement of

hydrophobicity at higher temperature above LCST[96-98]. When the temperature increases, the hydrogel become hydrophobic and thus lead to a strong interaction with hydrophobic compounds such as TCE, i.e. a higher partitioning rate for TCE. Based on the TCE adsorption experiment for 24h is shown in Figure 2.10, only 30% of TCE was adsorbed at 23°C (below LCST), while it was increased to 65% at 34°C (above LCST). However, the TCE adsorption through PAA hydrogel shows decrease of adsorption amount when temperature increases, which shows the importance of hydrophobic property of NIPAAm segment. Therefore, in addition to the prevention of agglomeration of nanoparticles, another advantage of using the temperature responsive hydrogels is the potential change in observed particle reactivity via the temperature change in state.

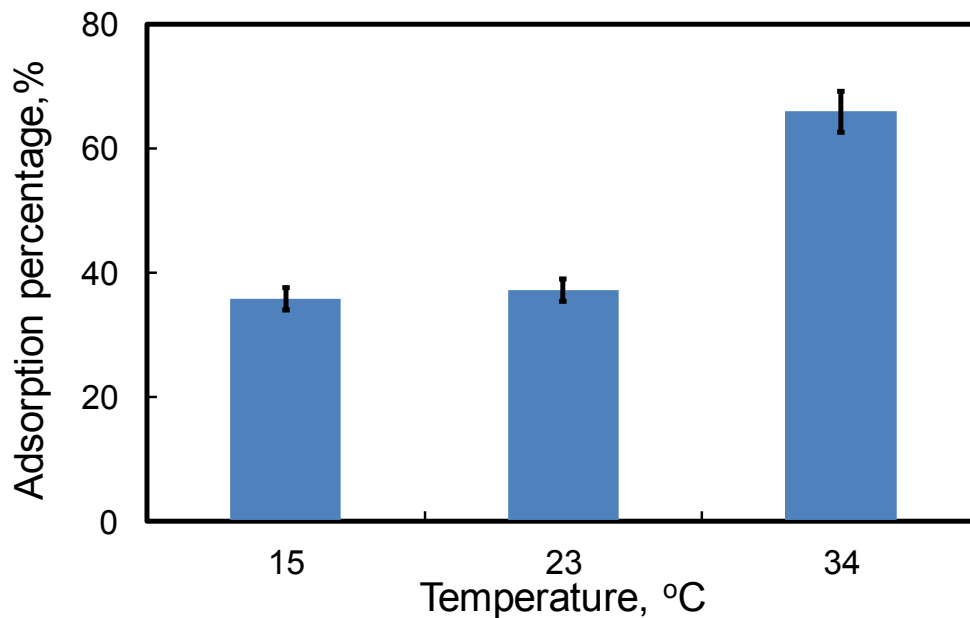


Figure 2.10. Normalized TCE adsorption through temperature responsive P(NIPAAm-AA) hydrogel below LCST (15°C and 23°C) and above LCST (34°C), feed concentration: 0.2 mM TCE, 20 mL, pH=6.8.

To demonstrate the effects of temperature on the reduction reactivity with hydrogel nanocomposites, the dechlorination performance with TCE or 2, 2'-dichlorobiphenyl (DiCB) by Fe/Pd bimetallic nanoparticles immobilized in a hydrogel were studied at 34°C and 30°C which cover the polymer domain transitions from hydrophilic to collapsed hydrophobic state as shown in Figure 2.11 and Figure 2.12, respectively. The surface area normalized reaction rate (k_{SA}) for Fe/Pd (1.5 wt% as of Fe) immobilized in P(NIPAAm-AA) hydrogel indicated three times increase from 0.0156 to 0.0411 L/m²h for TCE dechlorination, and from 0.06 to 0.21 L/m²h for DiCB dechlorination. For comparison, dechlorination with Fe/Pd in solution phase (about 50 nm) was also conducted and showed only two times increase of reactivity, which demonstrates the primary role of partitioning increase in the reactivity improvement via temperature change for hydrogel immobilized nanoparticle. It should be mentioned that the reactivity here is lower than the referenced value[139]. This may be due to the reason that Fe/Pd reactivity is a strong function of Pd loading amount, and the chloro-organics dechlorination rates could vary by 1-5 orders of magnitude by changing the Pd loading amount[70, 114]. The TCE or PCB diffusion rate in hydrogel networks should be faster than that in the aqueous phase when the hydrophobicity of the hydrogel increases via a temperature increase, helping to enhance the overall dechlorination rate as illustrated in Figure 2.13. In addition, the calculated nanoparticles volume fraction was increased by more than 2 times, which can expectedly lead to the enhancement of dechlorination reactivity. The

discussion may lead to the question why not use hydrophobic polymer immobilized catalyst and do the reaction and the same result could be obtained. The hydrophobic polymer can indeed increase the absorption of chlorinated organics. However, truly hydrophobic polymer cannot make hydrogels with porous network and the synthesis of nanoparticles without any water is also not possible. On the other hand, the hydrophilic and hydrophobic copolymer used in this work can perfectly fit the needs.

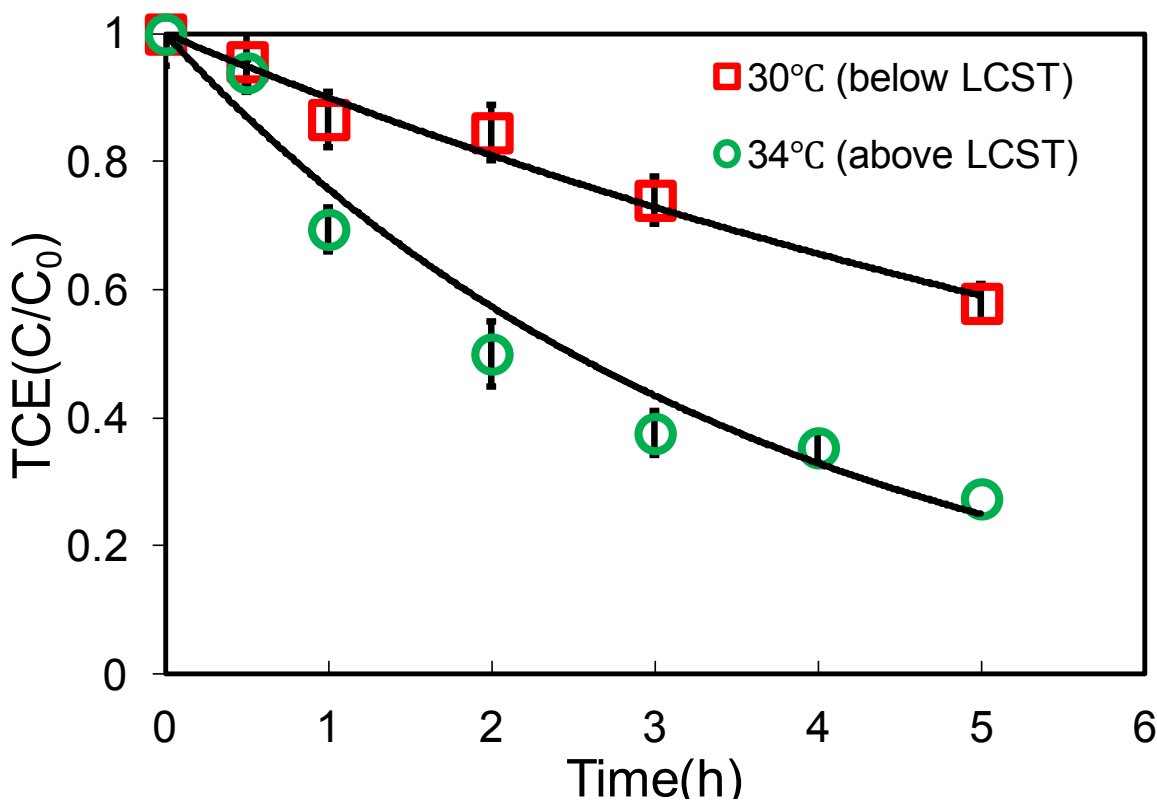


Figure 2.11. Batch dechlorination of TCE with Fe/Pd (Pd=1.5 wt%) (70nm) immobilized in P(NIPAAm-AA) hydrogel at 30°C (below LCST) and 34°C (above LCST). Vol. = 43mL, pH=6.8; initial TCE concentration: 30 mg/L, iron loading amount: 0.3g/L.

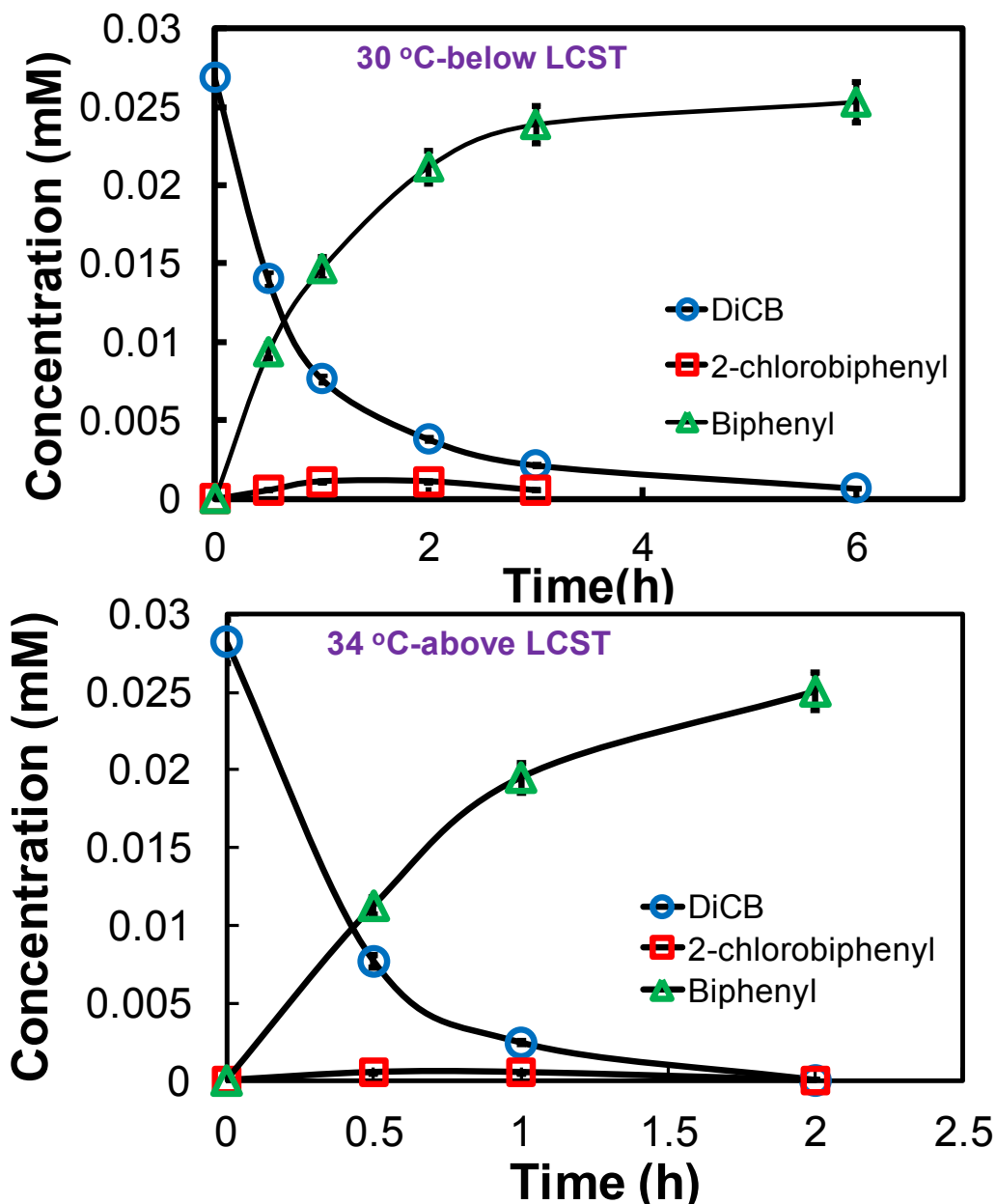


Figure 2.12. Batch dechlorination of 2,2'-dichlorobiphenyl (DiCB) with Fe/Pd (Pd=2.4%) immobilized in P(NIPAAm-AA) hydrogel at 30°C (below LCST) and 34°C (above LCST). Vol. = 43mL, pH=6.8; initial DiCB concentration: 5 mg/L, iron loading amount: 0.5g/L.

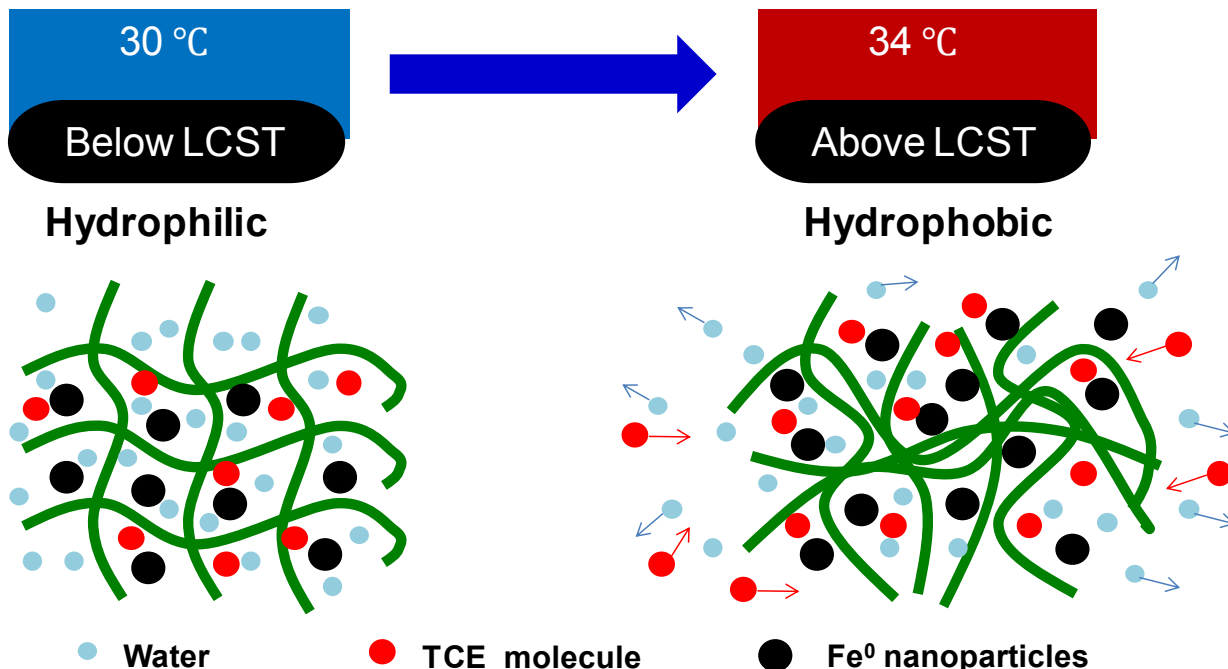


Figure 2.13. Schematic of temperature behavior and transport of reagents with temperature responsive hydrogel immobilized Fe⁰ nanoparticles.

Our lab has reported the PAA functionalization of membrane with subsequent Fe and Fe/Pd nanoparticles immobilization to degrade a variety of toxic chlorinated organic compounds[149, 150]. Here, P(NIPAAm-AA) hydrogel was utilized because of the demand of not only transition but also hydrophilic ion exchange sites, like -COOH. The use of PAA hydrogel without NIPAAm could make it difficult to modulate hydrophobicity in the same platform. In addition, some minimum water content is required to maintain the reaction as the reactivity will drop to zero[129] if iron nanoparticles are placed in completely hydrophobic domain such as polydimethylsiloxane (PDMS). Therefore, by the use of P(NIPAAm-AA) hydrogel, all of these requirements about balanced hydrophobicity and hydrophilicity, minimum water content and ion exchange groups, post capture of dissolve Fe can be achieved. Here, it should be pointed

out that the cycle for TCE/PCB degradation between low temperature (below LCST) and high temperature (above LCST) was just used to prove the concept that the use of temperature responsive hydrogel can modulate the dechlorination reaction reactivity by control the water content in the matrix and enhance the affinity and partitioning of hydrophobic TCE/PCB to the polymer matrix. Even though the high temperature above LCST of NIPAAm is impractical in real water treatment application, the main purpose is to look at the fundamental aspects. Furthermore, the transition temperature can be decreased by introduction of hydrophobic moiety (such as, tert-butyl methacrylate (tBMA), butyl methacrylate (BMA), etc) into the copolymer as widely reported in the literatures[151-153].

A common problem for using nanoparticles in solution phase is that the oxidation of iron by dissolved O₂ in water and iron corrosion by water can lead to the loss of iron and formation of precipitates. In contrast, the use of hydrogel with the carboxylic groups can effectively prevent precipitation to give longevity. Our preliminary study with a multi-trial TCE dechlorination studies (6h for one trial) proved no loss of reactivity even after 3 days' storage, which can be very practical for environmental application to prevent aggregation and loss of reactivity as compared to conventional nanoparticles.

2.4 Conclusions

In conclusion, temperature responsive P(NIPAAm-AA) hydrogel prepared by free radical polymerization have been investigated as templates for the in-situ formation of nanosized Fe particles with uniform size and distribution. The hydrogel immobilized Fe nanoparticles showed a strong reactivity for the

reductive degradation of a model toxic chlorinated organic, a common pollutant, TCE and could be recyclable and reused. Furthermore, the reduction reaction rate was modulated by taking advantage of hydrophobic and hydrophilic transitions (30 to 34°C) through controlling the swelling and collapse of the hydrogel at LCST of temperature responsive hydrogel. The development of reactive polymer hydrogel with nanoparticles and controlled partitioning should lead to applications ranging from organic synthesis to pollution control.

2.5 Broad Application Prospect

The combination of hydrogels or polymers and metal nanoparticles has generated a new class of catalytic materials. The key aspect of hydrogel network is suitable for in-situ or ex-situ preparation of nanoparticles. The free space in the hydrogel matrix can act as nanoscopic domain, which is excellent and efficient for the growth of nanoparticles, providing not only stabilization but also prevention of oxidation. Thus, the size, the morphology and the shape of nanoparticles can be controlled by varying the polymer/metal ratio or the cross-linking degree, which endow them with particular surface properties[154, 155]. Furthermore, the catalytic reaction rate can be modulate through controlling the swelling and shrinking of the host hydrogel network by temperature change. Thus, one can envisage a broad application of these systems in temperature dependent catalytic reactions, such as, in the fields of synthesis of amino compounds in a large scale and wastewater treatment. In addition, the electronic properties can also be controlled by the utilization of nanoparticles/responsive hydrogel composites. For example, the presence of Au nanoparticles inside

PNIPAAm hydrogel provides tunable electronic and optical properties through the swelling and shrinking thermal transition[155]. Beside the application in catalytic reaction, responsive polymer can also be utilized in separation area. For example, the functionalization of chromatographic columns with PNIPAAm moiety[156] was reported to obtain tunable separation of peptides through the control of hydrophobicity and hydrophilicity transition.

Chapter 3 - Development of Bench and Full-Scale Temperature and pH Responsive Functionalized PVDF Membranes with Tunable Properties

3.1 Introduction

Environmentally sensitive polymers have gained considerable attention in areas ranging from new material designs to drug delivery and composite biomaterials[38, 157-159]. These polymers can transform between swollen and shrunk state reversibly in response to environmental conditions such as pH, temperature, light, the nature of solvent and added chemicals[44, 160, 161]. For example, poly(acrylic acid) (PAA) is a typical polyelectrolyte and particularly used in sensing and modulating external chemical signals due to the conformation change based on pH change and ionic strength of the aqueous media[162]. Poly(N-isopropylacrylamide)(PNIPAAm), on the other hand, is the most widely studied temperature responsive polymer. It exhibits remarkable and reversible hydration-dehydration changes in temperature near lower critical solution temperature (LCST) at around 32°C[163]. Below the LCST, the polymer network is hydrophilic due to the formation of the hydrogen bonding between amide groups on the PNIPAAm chain and water molecules. When the temperature increases higher than the LCST, the hydrogen bonds are broken and water is expelled from the network leading to the hydrophobic network[98, 164]. These smart polymers are considered to have great potential in a wide variety of applications, such as, controlled drug delivery, chemical separation, water treatment, sensor and bioreactors[47, 165, 166].

Unfortunately these polymers usually lack mechanical strength to be used alone for a particular application. Therefore, responsive membranes with the combination of a responsive hydrogel and a porous substrate membrane have been developed [42, 167]. The porous supports can provide mechanical strength and dimensional stability. Several micro-porous supports have been reported including poly(vinylidene fluoride) (PVDF)[166], polyethylene (PE)[168], polypropylene (PP)[169], poly(ethylene terephthalate) (PET)[170], polycarbonate (PC)[171]. PVDF is known to have advantages of good thermal and chemical resistance properties and also the asymmetric structure is known to have lower mass transfer resistances[172]. Our group has already published the formation of PAA hydrogels inside the pores of PVDF membranes for in-situ nanoparticle fabrication and toxic organic remediation[150, 173].

Since temperature responsive polymer is the most easily designed and controlled among these stimuli, thermo-responsive membranes have gained special interest. Most thermo-responsive membranes have been prepared by forming PNIPAAm chains directly in/on porous membranes. The methods reported include UV photo-grafting, plasma modification, irradiation and ion-tracking[51, 174, 175]. These macroporous membranes with PNIPAAm hydrogel can act as a valve with controlled or adjusted permeability due to the open and close of membrane pores caused by the shrinking and swelling of PNIPAAm chain according to the temperature changes. In comparison with conventional separation process, this proposed membrane system may have the potential to separate mixtures of molecules with similar molecular sizes through selective

adsorption of different molecules based on the modification of hydrophobicity and hydrophilicity by immobilized thermo-sensitive gel[51]. Moreover, the process has both feed and permeate streams, which can allow the continuous flow and allow to collect the permeate with a temperature swing operation. Besides the use of advanced separation, this system also has the potential to water treatment technology[176]. This platform can be used as a support to immobilize metal nanoparticles for catalytic dechlorination of toxic chlorinated organic compounds with the prevention of aggregation, oxidation and potentially tunable reactivity via the change of temperature. On the other hand, the immobilized functional polymers in the membrane support are important for the gating of stimuli-responsive permeability of membranes. Therefore, several important parameters, such as the grafting yield, the morphologies of filled polymer gel, the molecular size of permeate and initial membrane pore size have been reported to play an important role[177] and need to be investigated. For responsive membranes, stable responsive characteristics are also very important and essential.

The synthesis of temperature responsive membranes have been published for the application of controllable drug release. However, the synthesis of both temperature and pH responsive membranes for both separation and reactions based on full-scale membranes hasn't been reported yet. Therefore, the main objectives of this study are: (1) preparation and characterization of PNIPAAm functionalized PVDF membrane; (2) investigation about the temperature responsive on solvent permeation properties; (3) studies of the effects of monomer concentration and cross-linker amount on the temperature

responsive permeation flux behavior; (4) the development of both temperature and pH responsive membrane based on full-scale membrane to evaluate the feasibility of continuous manufacture of functionalized membranes and (5) the synthesis of PNIPAAm-PAA-PVDF with immobilized metal nanoparticles for catalytic dechlorination.

3.2 Experimental

3.2.1 Materials

All chemicals were used as reagent grade. Hydrophilized polyvinylidene fluoride (PVDF) microfiltration membranes were obtained from Millipore (average pore size: 0.65 μm , thickness: 125 μm , porosity: 70%, diameter: 142 mm) and full-scale PAA-PVDFHE membrane[178] (hydrophilized, average pore size: 0.42 μm , PVDF layer thickness: 70 μm porosity: 45–55%) was obtained from Ultura Inc., Oceanside, CA. N-isopropylacrylamide (NIPAAm), N,N'-methylenebisacrylamide (BIS), ammonium persulfate (APS), N,N,N',N'-tetramethylethylenediamine (TEMED), acrylic acid (AA) and ethanol (>99.5%), dextran ($M_w=2,000,000$ g/mol) were purchased from Sigma-Aldrich. Deionized ultra-filtered water (DIUF) was from Fischer Scientific. Ultra-high purity (UHP) nitrogen gas used in flux experiments was purchased from Scott Specialty Gases.

3.2.2 Synthesis of PNIPAM-functionalized PVDF Millipore Membrane

Although many membranes can be used for this application, PVDF membrane was chosen in this paper because of its chemical resistance properties and good thermal stability[172]. The thermo-sensitive PNIPAAm-

PVDF membrane was prepared via pore-filling method by the redox polymerization as reported in the literatures [179, 180]. The polymerization was conducted in the aqueous phase. The polymerization solution contained 5 wt% NIPAAm (monomer), BIS (cross-linker, added in a 0.1-5% molar ratio of BIS to NIPAAm), and 1% APS (initiator). The solution was purged with nitrogen for 1h. After adding 1% of redox accelerator, TEMED, the PVDF membrane was put into the solution and the reaction continued for 6h at 25°C. The resulting composite membrane was taken out from the gel carefully and immersed in DIUF overnight. The effects of cross-linker density and monomer concentration were also studied.

The full-scale FPAA-PVDFHE flat sheets (1.0 m wide and 91.4m long, 70 μm PVDF thickness) were recently developed by joint work with Ultura Inc, Oceanside, CA. These hydrophilized PVDF membrane support was made with backing fabric to increase material stability. They have fairly uniform geometry, open structure and polymer distribution. The full-scale membrane was post-functionalized with PNIPAAm to get both temperature and pH responsive behavior. It should be noted that unlike the Millipore PVDF membrane, the functionalization of full-scale membrane was by dip-coating method. Therefore, a higher NIPAAm concentration (13wt%) is used to make sure enough polymer formed in the pores. 1 mol% of BIS and 1 mol% of APS with respect to NIPAAm were added to the solution, and the membrane was immersed in the monomer solution for 5 min. The membrane was sandwiched into two glass plates after getting rid of excess solution on the membrane surface and put it in the oven for 2.5h at 70°C. The membrane was washed with DIUF and ethanol for several

times, and immersed in DIUF overnight. The schematic for the PNIPAAm functionalization with full-scale FPAA-PVDFHE Ultura membrane (PNIPAAm-FPAA-PVDFHE) is shown in Figure 3.1. The membrane description and their abbreviation are shown in Table 3.1.

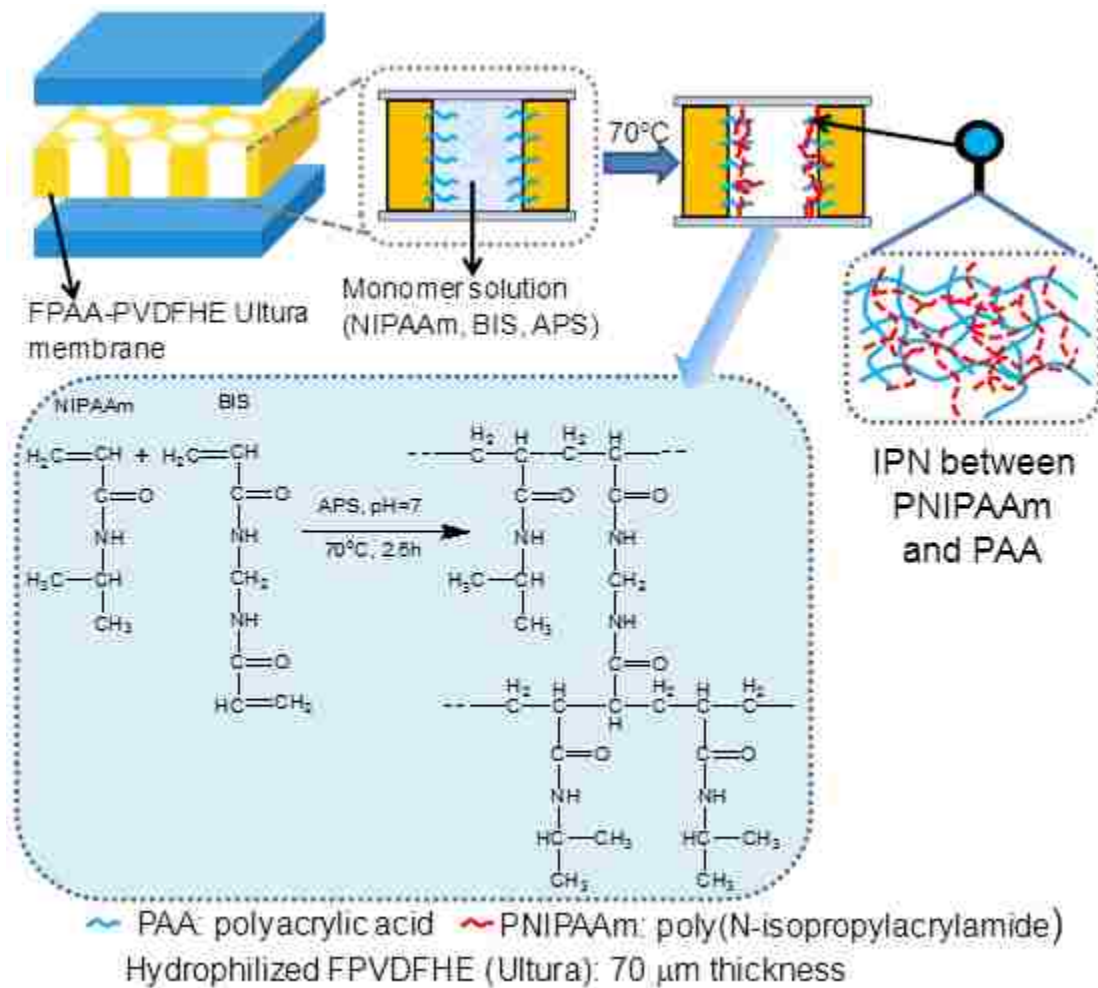


Figure 3.1 Schematic of proposed interpenetrating network (IPN) formation by post PNIPAAm functionalization of full-scale cross-linked FPAA-PVDFHE Ultura membrane (PNIPAAm-FPAA-PVDFHE).

Table 3.1 Functionalized Membranes Utilized in Experiments

Membrane abbreviation	Membrane full name
PNIPAAm-PVDF	PNIPAAm functionalized Millipore PVDF membrane in lab-scale
FPAA-PVDFHE	Full-scale PAA functionalized PVDFHE membrane by joint work with Ultura Inc. CA, USA
PNIPAAm-FPAA-PVDFHE	Post PNIPAAm functionalized FPAA-PVDFHE membrane in lab-scale

3.2.3 Attenuated Total Reflectance Fourier Transform Infrared (ATR-FTIR)

Attenuated total reflectance Fourier transform infrared (ATR-FTIR) (Varian 7000e) was used to determine the presence of functional groups in PNIPAAm-PVDF membrane. The samples were placed on the diamond crystal and the spectrum was obtained between 500 and 4000 cm^{-1} for 32 scans at a resolution of 8 cm^{-1} .

3.2.4 Scanning Electron Microscopy (SEM)

The surface and cross-section morphology of the blank PVDF and PNIPAAm-PVDF membranes were studied by Hitachi S-4300 Scanning Electron Microscope (SEM). The samples were mounted on the sample studs and a thin layer of gold was sputtered on the sample surface for imaging purpose. The SEM measurements were performed at an accelerating voltage of 10 kV.

The effect of temperature on the morphology of membranes was also investigated. The membranes were swelled in water at temperature 25°C and 40°C for 48h to reach equilibrium, respectively. Then, the membrane was taken out and immediately put it in liquid nitrogen, and freeze dried. The dry samples were used for SEM analysis.

3.2.5 Thermal Analysis

The thermal properties of the PNIPAAm-PVDF membrane were measured by thermogravimetric (TG) analysis and differential scanning calorimetry (DSC). For TG analysis, the samples were heated up to 600°C with a rate of 10°C/min under dry nitrogen atmosphere by using a TGA 2050 thermo-gravimetric analyzer (TA Instrument, USA). About 4 mg sample was used. For DSC analysis[166, 179], the samples were immersed into distilled water at room temperature for at least two days to reach a swollen state. About 5 mg swollen sample was placed inside a hermetic aluminum lid. The thermal analyses were performed from 25 to 55 °C on the swollen hydrogel samples under a dry nitrogen atmosphere with a flow rate of 25 mL/min and a heating rate of 2.5°C/min.

3.2.6 Atomic Force Microscopy (AFM)

The membrane surface was also characterized by AFM (Agilent PicoPlus 3000) using a resonance frequency of approximately 150 kHz in tapping mode. The average roughness (the average deviation of the peaks and valleys height from the mean value) was determined on 5 µm × 5 µm membrane area. All AFM images were processed and presented using Gwyddion software.

3.2.7 X-ray Photoelectron Spectroscopy (XPS) Analysis of Membrane Surface

The surface composition of membrane was characterized using an X-ray photoelectron spectroscopy (Thermo Scientific K-Alpha) with Al/K ($h\nu=1486.6$ eV) anode mono X-ray source. The sample was directly mounted on a sample holder then transferred into the analyzer chamber. The whole spectra of all the elements with much high resolution were recorded with the Avantage software. Each survey spectra was the average of five survey scans.

3.2.8 Temperature-responsive Flux Measurements

The water permeability was measured at different temperatures to study the temperature responsive flux behavior of PNIPAAm-PVDF Millipore membranes and PNIPAAm-FPAA-PVDFHE Ultura membrane. The tested membrane was mounted in a stirred cell (Millipore). The stirred cell containing the feed water was kept in constant temperature for at least 1.5 h by electrical heating tape with a digital thermocouple to continuously monitor the internal feed temperature at the membrane-solution interface. The cell was pressurized using pure nitrogen. Once the membrane flux reached steady-state, volume flux was measured in triplicates by recording the volume passed in a given time interval. A final run was conducted by adjusting the feed temperature back to 30°C to test for reversibility.

3.2.9 Dextran Rejection

The solution consisting of 2 g/L dextran ($M_w = 2,000,000$ g/mol) was fed into a convective flow cell and was equilibrated at 30°C for 1h at 1.4 bar. After

first run, the DIUF feed was replaced with dextran solution at 30.0°C to wash the membrane. Then, a second rejection study was conducted at 34.0°C. All experiments were conducted in triplicate and average values are given. After equilibration, multiple permeate and feed samples were collected for total organic carbon (TOC) and gel permeation chromatography (GPC) analysis.

3.2.10 Total Organic Carbon (TOC) Analysis

The total organic carbon was analyzed using a TOC analyzer. Carbon standards were prepared in the range from 1-100 mg/L and were used to generate a calibration curve. Samples were automatically introduced to the TOC analyzer (experimental error <2%). Ultra-high purity nitrogen was used as the carrier gas at 87.0 psi and a flow rate of 150 mL/min.

3.2.11 Gel Permeation Chromatography (GPC)

Feed and permeate samples (1mL) were analyzed by a Shimadzu HPLC system with a Shimadzu refractive index detector (RID-10A). The gel permeation column used was a Shimadzu (Tokyo, Japan) TSK-GEL G6000PWXL. Column temperature was maintained at 30±1°C. For analysis, the column was operated under isocratic flow conditions of 0.5 mL/min with phosphate buffered saline (PBS) (0.0119M phosphates, 0.137 M NaCl, 0.0027 KCl) (pH 7) as the mobile phase. Before injection, the samples were filtered with 0.45 µm PVDF porous membrane.

3.2.12 Salt Rejection through PNIPAAm-FPAA-PVDFHE Ultra Membrane

Na₂SO₄ rejection experiments were performed using a stirred membrane cell provided by Millipore with a membrane cross-sectional area of 13.2 cm² including a stirring device to minimize the effects of concentration polarization. The effects of Na₂SO₄ concentration on the rejection was also investigated by using 100 mg/L and 1000 mg/L concentration. The sodium concentration was measured with a Varian AA220 series atomic absorption spectrophotometer.

3.2.13 Metallic Nanoparticles Synthesis within PNIPAAm-FPAA-PVDFHE Membrane

The method for the synthesis of nanoparticles is developed by our group and described anywhere else [150, 173]. Before ion exchange with Fe²⁺, the membrane was immersed in NaCl/NaOH solution (pH=11.9) overnight to convert -COOH to -COONa. In the next step, the membrane was washed with DIUF until the pH of the effluent became neutral. Then, the membrane was immersed in 200 mL 200 mg/L FeCl₂ solution at a pH of 5.5 for 4 h. Nitrogen gas was bubbled to minimize the oxidation of Fe²⁺. The reduction with sodium borohydride ensured the Fe⁰ nanoparticle formation. The membrane was stored in ethanol to prevent the oxidation. For the deposition of second metal (Pd) on the surface of Fe nanoparticles, the membrane was immersed in K₂PdCl₄ solution of ethanol and water (90:10 vol%). The concentration of K₂PdCl₄ solution varied based on the Pd amount desired to be deposited on the Fe nanoparticles. The amount of Fe and Pd immobilized in the membranes during the ion exchange and post

coating was quantified using Varian AA220 series atomic absorption spectrophotometer with the wavelength of 386.0nm and 247.6 nm respectively.

3.3 Results and Discussion

3.3.1 ATR-FTIR Spectroscopy of PNIPAAm Functionalized PVDF Membrane

The functionalization of the PVDF membranes with PNIPAAm was characterized by ATR-FTIR spectroscopy as shown in Figure 3.2. The characteristic absorption band for CF_2 of blank PVDF appears at 1120-1280 cm^{-1} [181]. Compared with the spectrum of blank PVDF membrane, two new peaks appeared at about 1650 and 1540 cm^{-1} in both spectra of PNIPAAm-PVDF and PNIPAAm-FPAA-PVDFHE composite membrane. The absorption band at about 1650 cm^{-1} belongs to the second amide C=O stretching (amide I) and the band at 1540 cm^{-1} is corresponding to the N-H stretching (amide II) of the O=C-NH groups in the PNIPAAm chains [174, 175, 182]. The peaks in 1366-1466 cm^{-1} range are corresponding to the symmetrical and asymmetrical bonds of isopropyl groups from NIPAAm. This comparison results verified the formation of PNIPAAm with PVDF membrane support by pore-filling method.

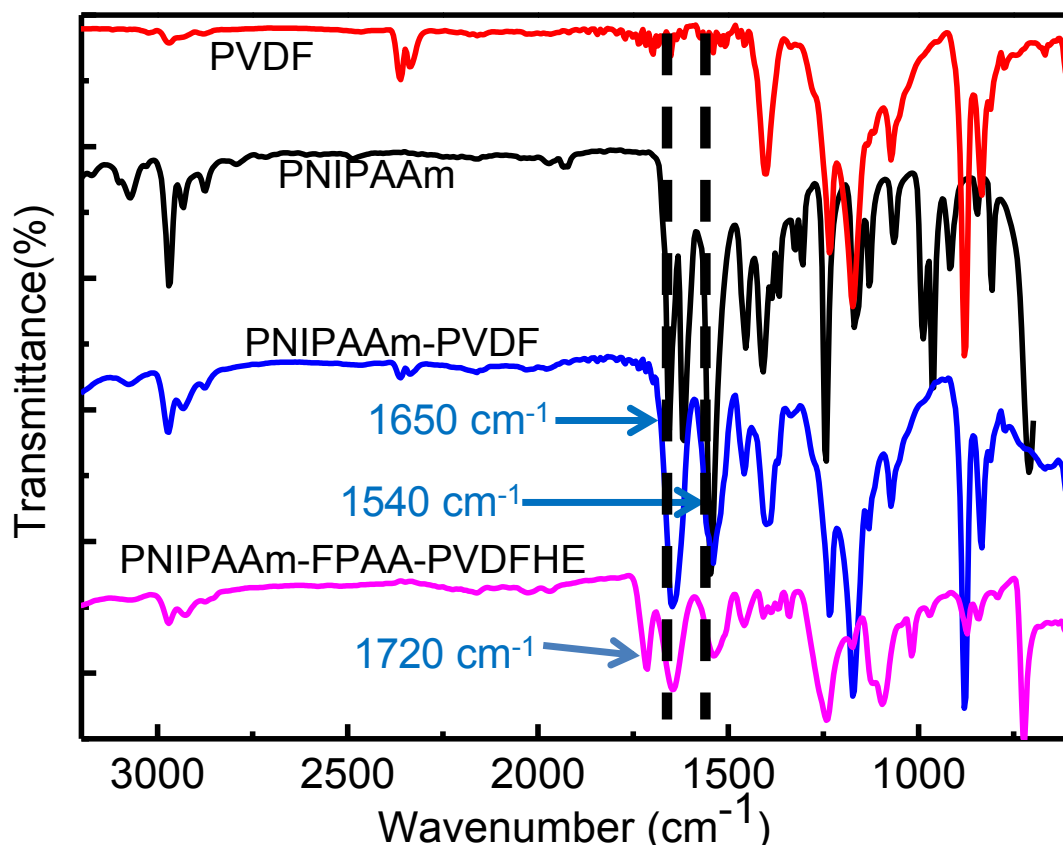


Figure 3.2. ATR-FTIR spectrum of blank PVDF, PNIPAAm functionalized PVDF Millipore membrane and PNIPAAm-FPAA-PVDFHE Ultura membrane.

3.3.2 Thermal Analysis

The thermal stability of blank PVDF and PNIPAAm-PVDF Millipore membranes were evaluated by TGA, and the resulting TGA curves are presented in Figure 3.3. The blank PVDF begins to decompose at about 460°C[181], while the PNIPAAm-PVDF shows a distinct two-step degradation process. This phenomenon is attributed to the degradation of PNIPAAm graft chains and PVDF main chains at different temperatures. The first major loss of PVDF-PNIPAAm begins at about 400°C, corresponding to the decomposition of PNIPAAm chains[175, 179]. The onset of second major loss occurs at about 460°C, which is attributed to the decomposition of PVDF main chains. The lower critical

solution temperature (LCST) was determined by DSC to be about 32°C (Figure 3.4) for PNIPAAm-PVDF functionalized membrane, which is consistent with the reported LCST of PNIPAAm[98, 166].

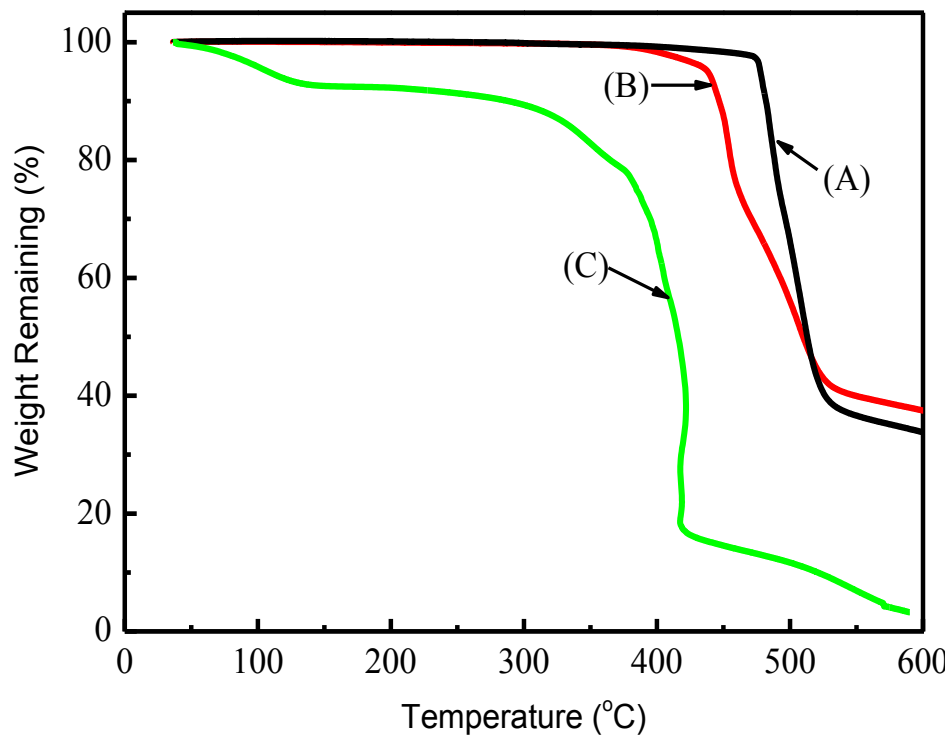


Figure 3.3. TGA curves of blank PVDF(A), PNIPAAm functionalized PVDF membrane (B) and the PNIPAAm homopolymer (C). The heating rate is 10 °C/min.

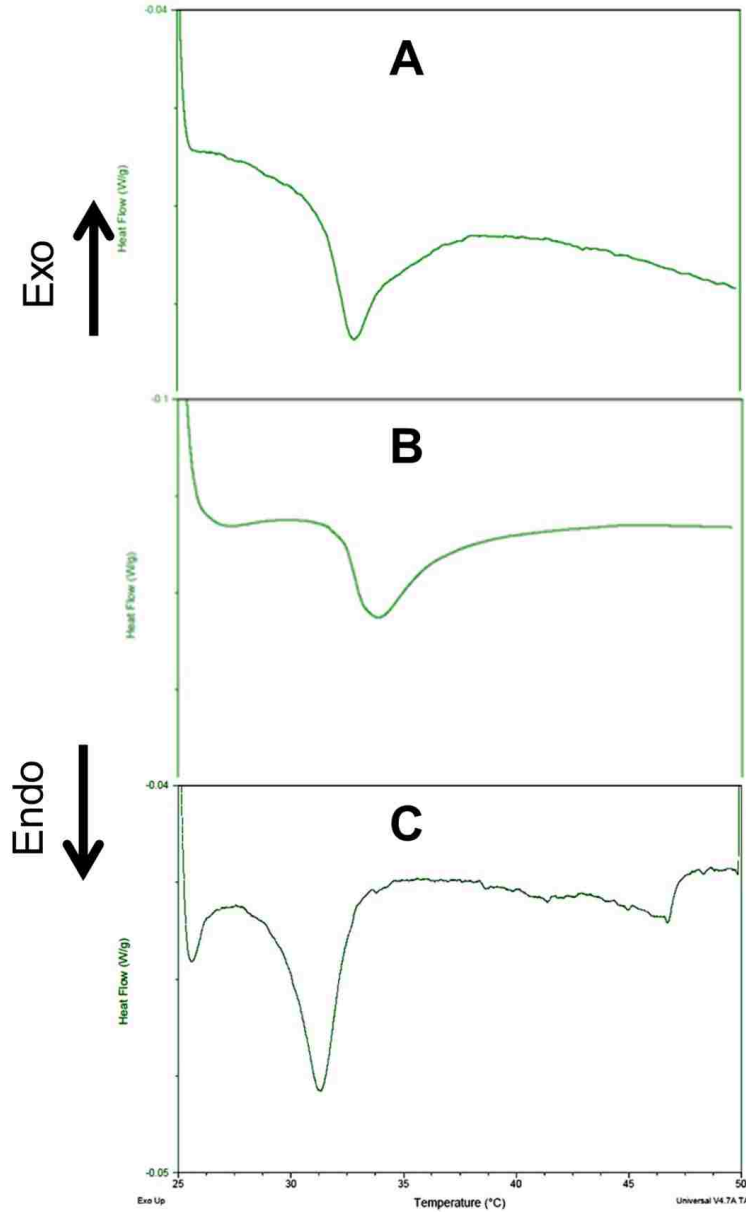


Figure 3.4. DSC thermograms of (A) PNIPAAm-PVDF membrane (heating rate=0.5°C/min), (B)PNIPAAm-PVDF membrane (2.5°C/min), (C)PNIPAAm hydrogel with (heating rate =0.5°C/min).

3.3.3 Microstructure and Morphology Analysis

3.3.3.1 SEM

The morphologies of the blank PVDF and PNIPAAm-PVDF Millipore membranes were examined by SEM shown in Figure 3.5. The blank PVDF Millipore membrane shows (Figure 3.5A) a highly porous structure with mostly circular shape and non-uniform pore size. As expected, the functionalized PNIPAAm-PVDF membrane (Figure 3.5B and C) showed less porosity with small size of pores. The grafted hydrogels were not removed in the rinse treatment, which indicate the strong attachment between the PNIPAAm hydrogel and the PVDF membrane[171]. The microstructure showed strong evidence of the polymerization of NIPAAm onto the membrane.

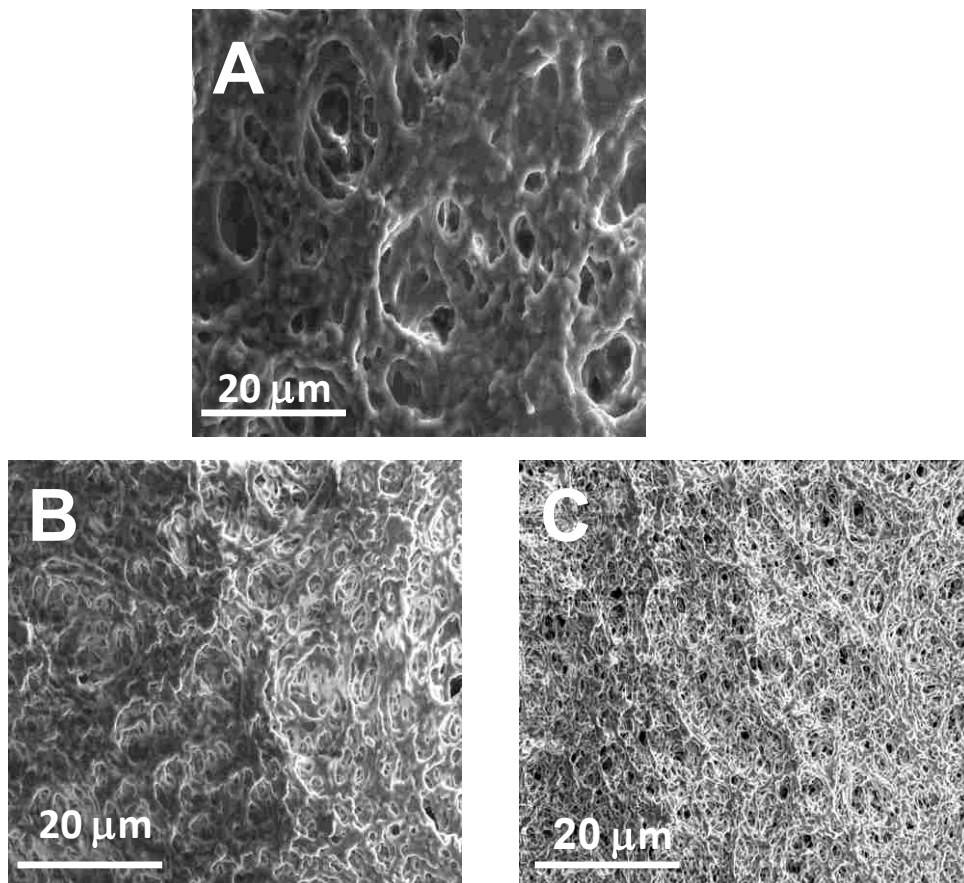


Figure 3.5. SEM images of blank PVDF (A) and PNIPAAm-PVDF Millipore membranes (B: 25°C(below LCST); C: 40 °C (above LCST))

On the other hand, the surface images (Figure 3.6A and B) of PNIPAAm-FPAA-PVDF Ultura membranes clearly show that the PNIPAAm was coated on the surface with decrease of pore size. Furthermore, it can be obviously seen from the cross-section images (Figure 3.6C and D) that the PNIPAAm hydrogel filled in the pores through the whole FPAA-PVDF layer resulting in a denser membrane and less porosity. It should be noted that all the SEM images are obtained under dry conditions. Therefore, the real morphology of PNIPAAm-FPAA-PVDF membranes may be more different from FPAA-PVDF membrane. These results are consistent with the reported methods by using different membrane supports and synthesis techniques [183, 184].

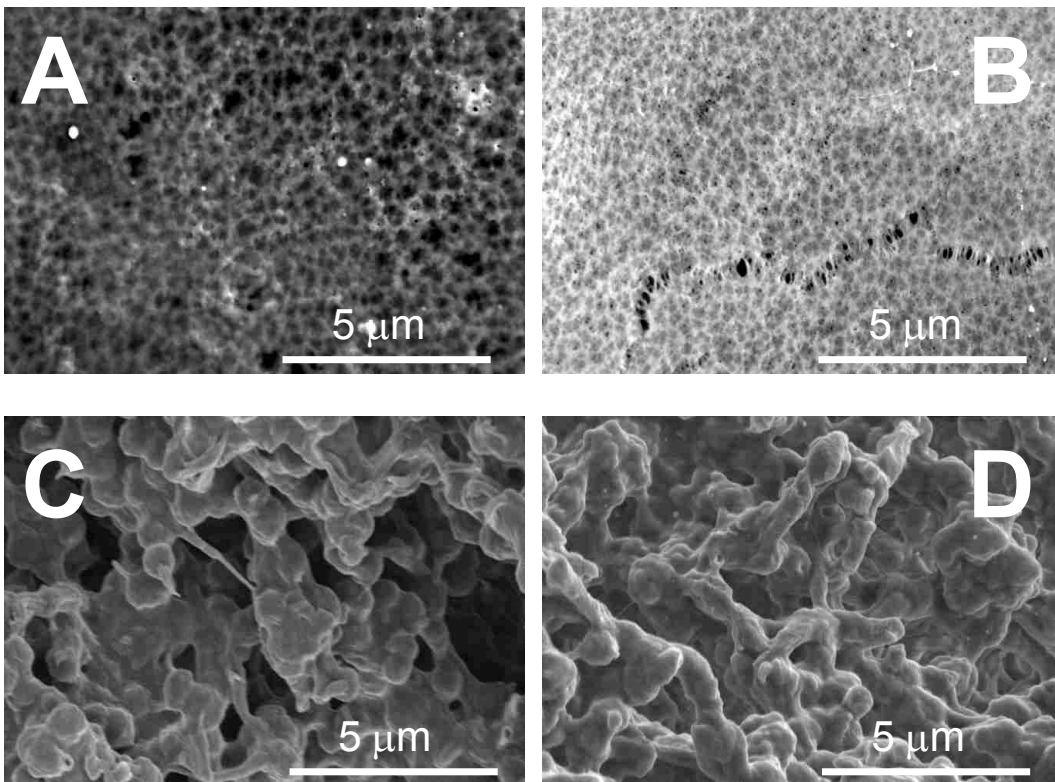


Figure 3.6 SEM images of full-scale FPAA-PVDFHE Ultura membrane surface (A) and cross-section(C) and PNIPAAm-FPAA-PVDFHE Ultura membrane surface (B) and cross-section (D).

The temperature effect on the structure of composite membrane was also studied and showed in Figure 3.5B and C. It indicates that the membrane pore size is increased when temperature increases from 25°C (below LCST) to 40°C(above LCST). This phenomenon is consistent with the change in conformation and orientation of the PNIPAAm chain near the LCST. When the temperature is below the LCST, the PNIPAAm hydrogel on the membrane or the inner pores swells and occupies the pore volume, which decrease the effective pore size. Whereas when the temperature above the LCST, the PNIPAAm hydrogel changes to a shrinking state, leading to the increase of the effective pore size. Therefore, by adjusting the initial monomer concentration, the pore-filling density in the membrane support can be controlled, which in turn regulate the temperature responsive behavior as detailed discussed in the following section.

3.3.3.2 AFM

AFM was chosen to characterize the surface morphology of full-scale PVDFHE and functionalized PNIPAAm-FPAA-PVDF ultra membranes as shown in Figure 3.7. Average roughness is defined as average deviation of the peaks and valleys from the mean plane and root mean squared (RMS) roughness is the RMS deviation of the peaks and valleys. The untreated PVDF membrane showed a flat surface, but as shown in Figure 3.7, PNIPAAm-FPAA-PVDF membrane roughness increases and has many isolated rough spots, which was also found with PNIPAAm grafted PET membrane[185, 186]. The remarkable topography change is attributed to the grafting of PNIPAM chains.

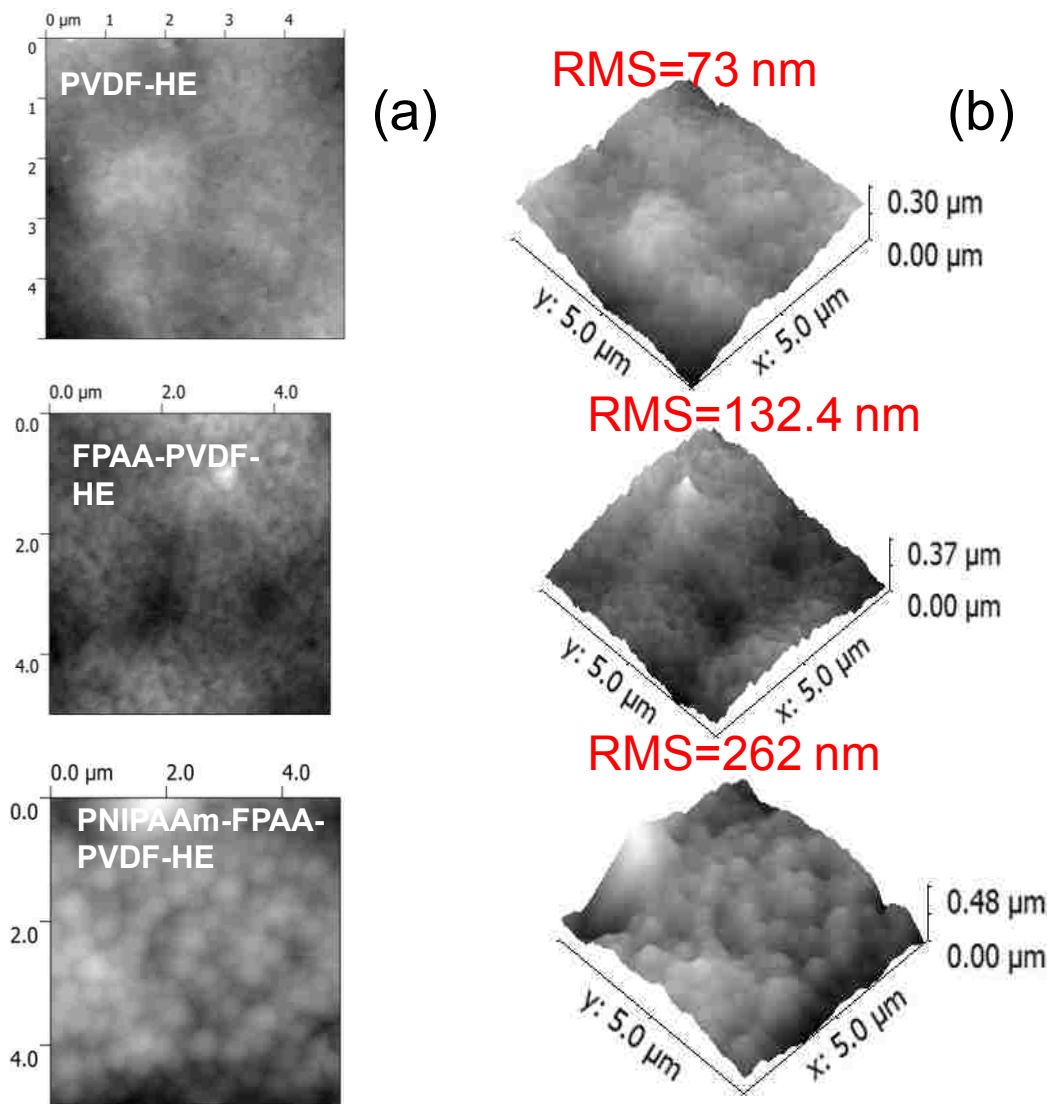


Figure 3.7. AFM image blank full-scale PVDFHE Ultura membrane, functionalized FPAAPVDFHE membrane, PNIPAAm-FPAAPVDFHE Ultura membrane: (a) top view and (b) 3D.

3.3.3.3 XPS

Figure 3.8 shows the respective survey and C1s core-level spectra of the blank and functionalized membranes. Compared with the survey of blank FPVDFHE (Figure 3.8A, left), the increase of O (1s) intensity (Figure 3.8B) (left) confirms the appearance of PAA on the membrane. While the F(1s) peak

intensity decreased, accompanied by the appearance of N (1s) peaks in Figure 3.8C(left) indicates the introduction of PNIPAAm on FPAA-PVDFHE membrane. The C1s core-level spectrum for all the membranes was curve-fitted. For FPAA-PVDFHE membrane, there are two peaks with the binding energy (BE) at 286.0 eV for the $\underline{\text{C}}\text{H}_2$ group, 290.6 eV for the $\underline{\text{C}}\text{F}_2$ groups[187]. The C1s core-level spectrum for FPAA-PVDFHE was curved-fitted with four peaks. The two peaks with BE at 286.0 eV ($\underline{\text{C}}\text{H}_2$) and 290.6 eV ($\underline{\text{C}}\text{F}_2$) is assigned to be PVDF main chains. The peak with BE at 288.6 eV belongs to the $\text{O}-\underline{\text{C}}=\text{O}$ group from the formed PAA polymer chains on the membrane[188]. The peak with BE at 284.7 is attributed to the hydrocarbon backbone of the PAA polymer[189]. On the other hand, the C1s core-level spectrum for PNIPAAm-FPAA-PVDFHE was also curved-fitted with four peaks. The peak with BE at 284.8 eV belongs not only to the hydrocarbon backbone from PNIPAAm, but also to that of PAA. The peaks with BE at 286.2 eV, 287.6 eV and 288.9 eV are attributed to $\text{HN}-\underline{\text{C}}=\text{O}$ (PNIPAAm), $\underline{\text{C}}\text{O}$ and $\underline{\text{C}}\text{OOH}$ (PAA). It should be noted that the XPS can only characterize the membrane surface with 0-10 nm thickness. The disappear of PVDF peaks in the C1s core-level spectrum for PNIPAAm-FPAA-PVDFHE may because the formation of PNIPAAm on the membrane surface.

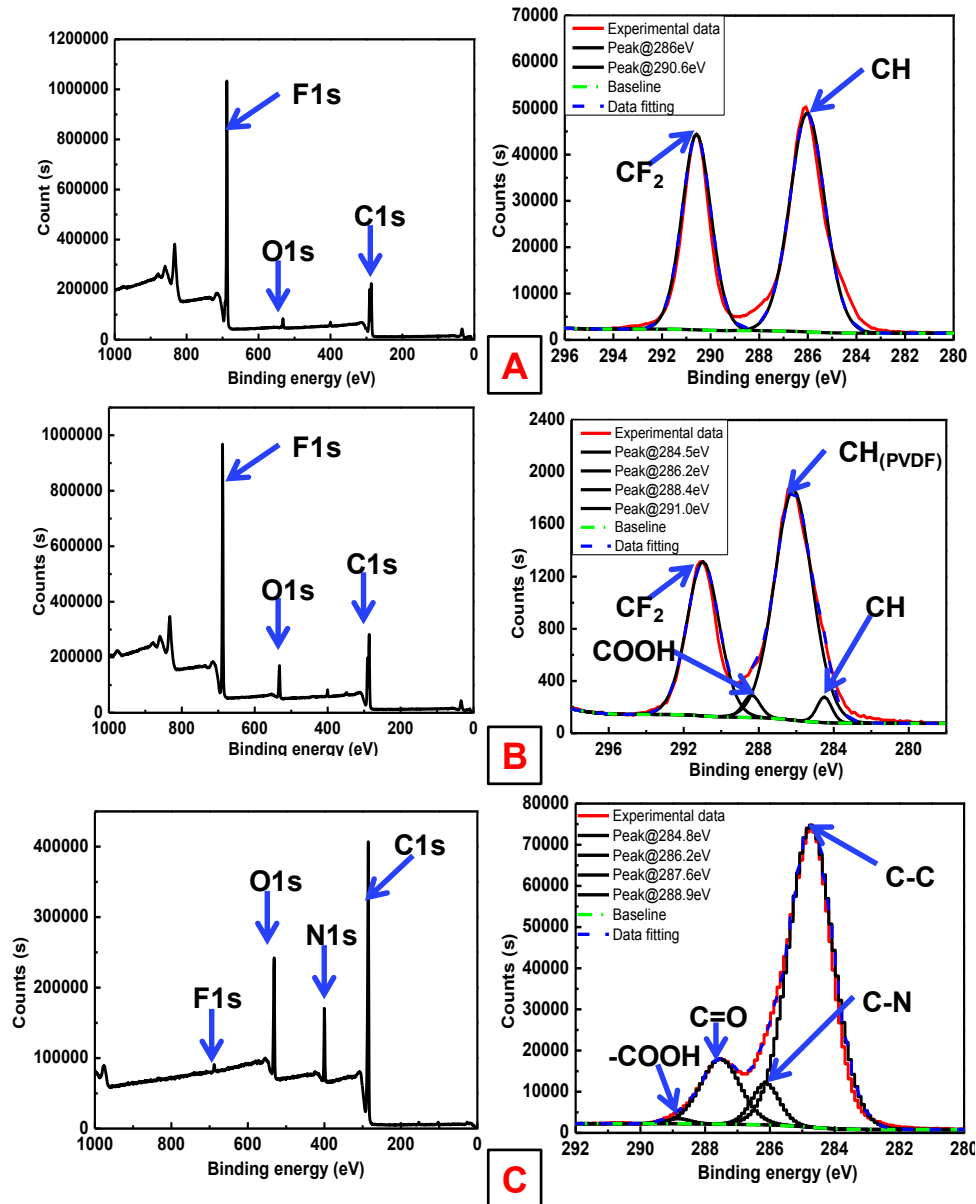


Figure 3.8. XPS survey (Left) and C1s core-level spectra (right) of (A) FPVDFHE; (B)FPAA-PVDFHE;(C) PNIPAAm-FPAA-PVDFHE membranes.

3.3.4 Temperature Responsive Water Flux through the PNIPAAm-PVDF Membranes

To investigate the pore opening and closing of PNIPAAm functionalized PVDF membrane due to the swelling and shrinking behavior with response to temperature changes, the water permeability of PNIPAAm-PVDF membrane was

measured at temperature below and above LCST. The effects of cross-linker amount and monomer amount are investigated in this section.

3.3.4.1 Theory

According to Hagen–Poiseuille’s (HP) equation [171, 179], the fluid flux is dependent on the following factors:

$$J = \frac{NA\pi\Delta P}{8\eta L} \left(\frac{D}{2}\right)^4 \quad \text{Eq.3-1}$$

Where J is the volume flux (L/m²/h); N is the membrane pore density; A is the membrane area; D is the pore diameter; η is the dynamic viscosity of water, L is the membrane thickness, and ΔP is the transmembrane pressure difference. According to this equation, the flux is inverse proportional to the viscosity, which is also related to temperature. Therefore, to eliminate the temperature effects, reported flux was normalized by:

$$J = \frac{J_T \eta_T}{\eta_{25^\circ C}} \quad \text{Eq. 3-2}$$

Where J_T and η_T represents the reported flux and viscosity at temperature T , and $\eta_{25^\circ C}$ represents the viscosity of water at 25°C.

Assuming a cylindrical pore and uniform polymer distribution throughout the membrane pores, the effective pore size can be calculated from Eq.1 based on the water flux measurement. Then the volume fraction (ϕ) of the polymer in the membrane is:

$$\phi = 1 - (D_f / D_o)^2 \quad \text{Eq. 3-3}$$

Where D_o is the pore diameter for blank membrane; D_f is the pore diameter for functionalized membrane.

3.3.4.2 Effects of Cross-linker Amount

In an attempt to control the membrane flux response, the effect of cross-linker amount was investigated. Figure 3.9 shows the water fluxes of PNIPAAm-PVDF membranes with different cross-linker amounts ranging from 0.1% to 2%. As for comparison, the permeability of blank PVDF membrane is 3809L/m²/h/bar. When temperature increased, the permeability of blank PVDF membrane was increased to 4864L/m²/h/bar due to water viscosity decrease (as indicated in Eq.1). To eliminate the effects of viscosity, all the flux data were normalized with viscosity at 25°C. As shown in Figure 3.9, PNIPAAm-PVDF membranes show obvious thermo-responsive characteristics. The ratio of flux at 30°C (below LCST) and 34°C (above LCST) was plotted in Figure 3.9 to directly compare the degree of response. For all the cross-linker amounts from 0.1 to 0.5 mol%, an increase in the relative permeability ratio or “valve” ratio was observed reaching a maximum of approximately 15 at the temperature about 34°C (above LCST). The valve mechanism was achieved by the transition between the polymer swelling (30°C) and shrinking (34°C) to close and open the membrane pore [175, 182] (as shown in the SEM image (Figure 3.5(B) and 3.5(C))). The constant permeability ($J_{30'}/J_{30}=1$) when temperature was returned to 30°C, indicates the temperature responsive reversibility and stability. For cross-linker amounts increased from 0.5 and up to 2.0 mol%, the permeability ratio decreased, but still retained temperature-responsive behavior. At higher crosslinker amount, the lower temperature response is due to the limited movement of PNIPAAm chains

immobilized in membrane pores, which can reduce the swelling ratio of hydrogel[179, 186]. Therefore, by varying the cross-linker amount, swelling–shrinking ratio of the thermo-sensitive membrane can be modified leading to greater or lesser flow through the membrane pores.

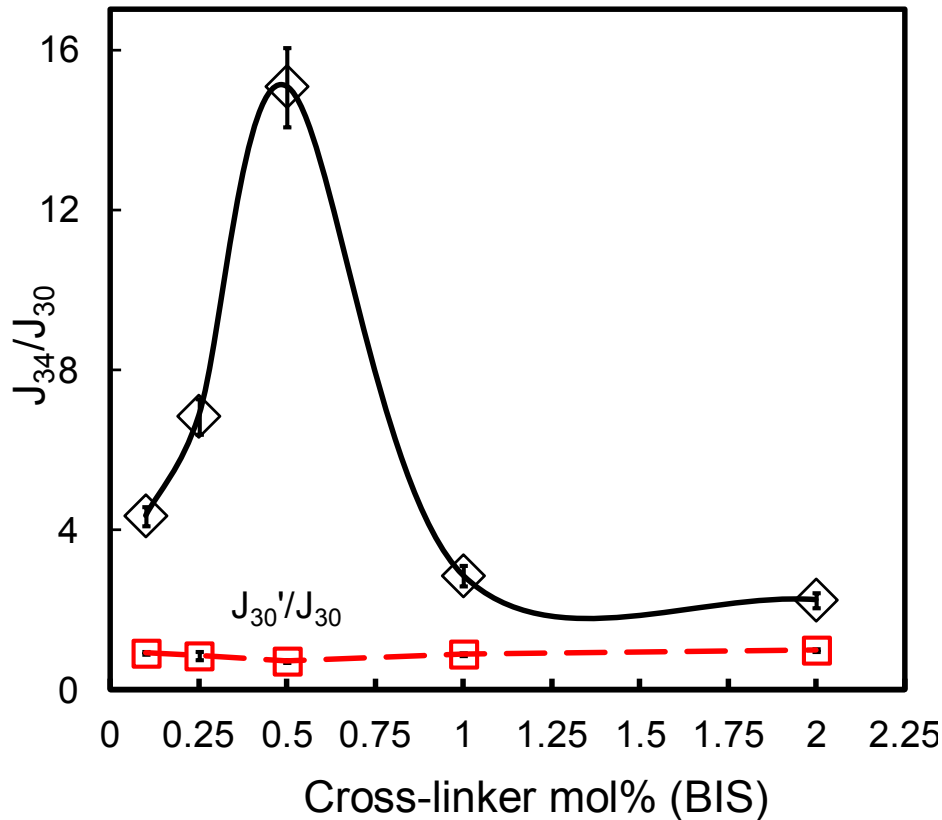


Figure 3.9. Dependence of thermally on-off ratio on the cross-linker amounts in the range from 0.1-2.0 mol% in for PNIPAAm-PVDF Millipore membrane (P=1.4 bar). For all the membranes, the NIPAAm concentration for polymerization solution was 5 wt%. Data was corrected with viscosity and normalized by permeability at 30°C.

3.3.4.3 Effects of Monomer Concentration

Since this temperature-dependent permeation is due to the conformation change of PNIPAAm chain on the surface and also in the membrane pores, the response of functionalized PVDF membranes can be regulated by the control of

grafting amount of NIPAAm. Figure 3.10 shows the relationship of flux and NIPAAm concentration. The flux was decreased as the increase of NIPAAm concentration. Wang et al[190] has proved the linear relationship between grafting amount and NIPAAm concentration in the range of 0-15%. Therefore, more pores will be occupied by the polymer with the monomer amount increase, which leads to the reduction of water permeability. According to the Hagen-Poiseuille's law, the mean effective pore diameter was calculated base on Eq. 1 and the result is shown in Figure 3.10. It shows the effective pore diameter decreased from 230 nm to 100 nm (650 nm for blank PVDF) with the increase of monomer amount from 1 to 5 wt% due to the increase of pore coverage by PNIPAAm hydrogels. By adjusting the monomer concentration, one would expect to control the morphology of the membrane pore and further regulate the temperature responsive behavior. This result is consistent with the previous reports by Lue and Wang's group[179, 186] and also a further proof of PNIPAAm inside the membrane pores.

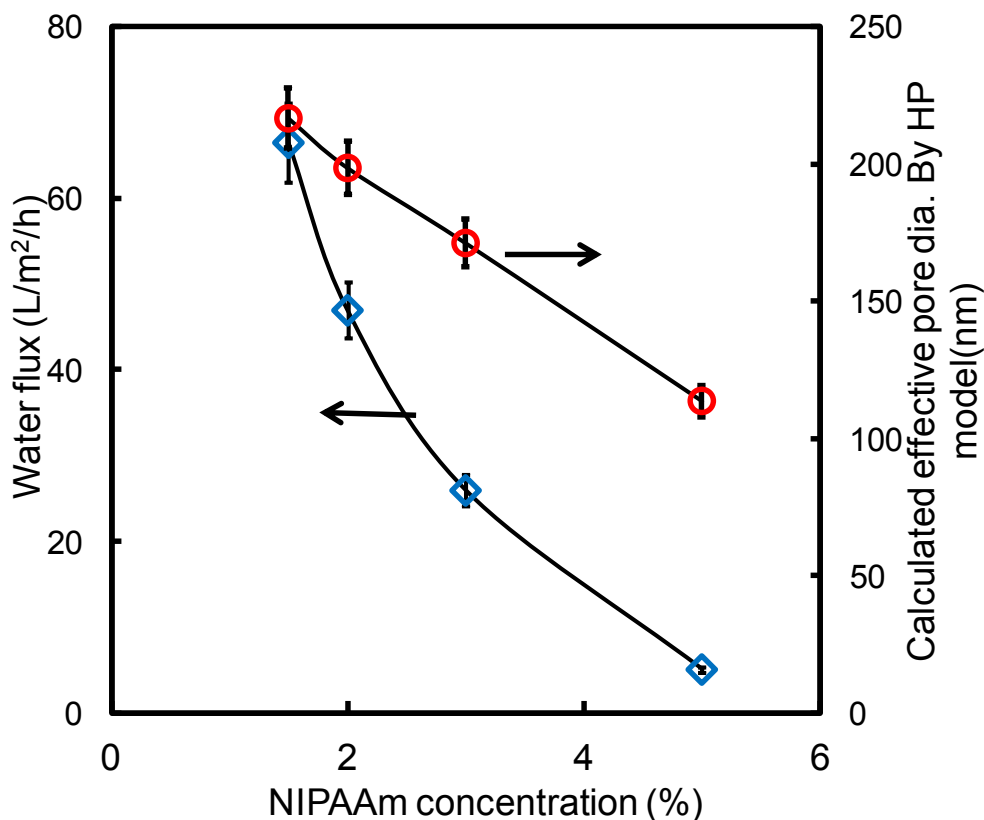


Figure 3.10. Effect of monomer (NIPAAm) concentration on water flux at 1.4 bar and calculated effective pore size for PNIPAAm-PVDF Millipore membrane. cross-linker concentration = 1mol%.

3.3.5 Quantification of Temperature Dependent Unsteady-state Membrane Flux

In order to reveal the dynamics of thermo-responsive gating behavior, the unsteady-state hydraulic flux through the PNIPAAm-PVDF membrane was plotted against controlled step changes in solvent feed temperature as shown in Figure 3.11. The feed temperature was raised by 4 degrees from 30.0°C to 34.0°C within an interval of 180 seconds. The observed change in steady-state flux was found to occur over a relatively short time interval of approximately 20 minutes. The second run (red circle, Figure 3.11) shows agreeable reproducibility in absolute flux measurements as well as reversibility of temperature flux

response over a similar time interval. The reversible flux response supports the conclusion that the stable network of cross-linked hydrogel and porous PVDF support provides increased mechanical robustness over extended periods of use and higher operating pressures.

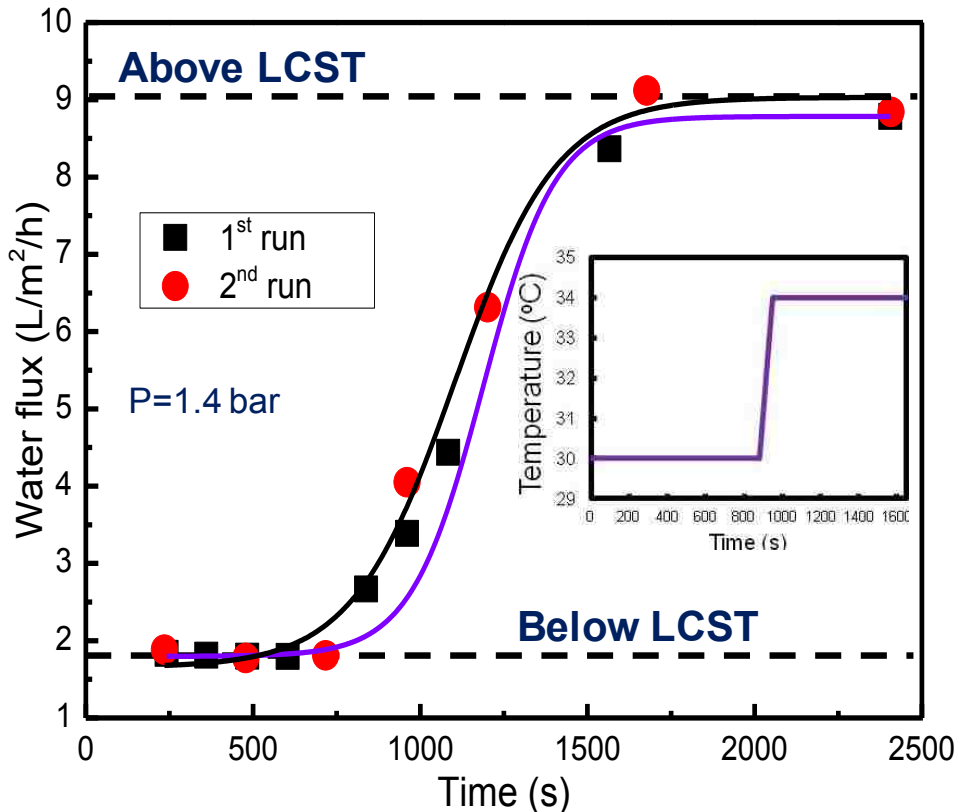


Figure 3.11. Dynamic and Reversible flux response versus ramp change in feed temperature above LCST and below LCST through PNIPAAm-PVDF Millipore membrane at P = 1.4 bar. The inset is the experimental temperature step change approximation. For the polymerization, the NIPAAm concentration was 5 wt%, cross-linker was 0.1mol%.

3.3.6 Temperature and pH Dependent Hydraulic Permeability of PNIPAAm-FPAA-PVDFHE Membrane

The flux of aqueous solutions through the PNIPAAm-FPAA-PVDFHE Ultura membrane was investigated as functions of both temperature (in the

temperature range from 22°C to 45°C) and pH (pH=4, 6.3, 7.3). The water permeability data are plotted against temperature and fitted with error function[171].

$$erf(T) = A + B \int_0^T \exp\left[-\frac{(T - T_c)^2}{(\Delta T)^2}\right] dT \quad \text{Eq. 3-4}$$

Where A and B are independent constants, T_c is the LCST (°C), and ΔT is the temperature transition change from open-state to closed-state (°C). By using this model, the experimental parameters, such as open-state permeability, close-state permeability, switching temperature, switching range can be determined. The regression was performed through a nonlinear least-squares curve fitting (lsqnonlin) in MATLAB®. The results are shown in Figure 3.12 and the fitted data are in Table 3.2. For comparison, the temperature has no effects on the full-scale FPAA-PVDFHE Ultura membrane as shown in the inset of Figure 3.12. In general, the water flux through the PNIPAAm-FPAA-PVDFHE Ultura membrane is both temperature and pH dependent. The water flux decreases with the increase of water pH from 4 to 7.3 at a fixed temperature. The volume fraction of hydrogel in FPAA-PVDFHE and PNIPAAm-FPAA-PVDFHE membranes are estimated to be 51% and 92% (pH=6.5) respectively, by using **Eq. 3-1** and **Eq. 3-3**. The volume fraction can significantly affect the transport of solute through the membrane pores and can be easily optimized by changing the grafting ratio of the hydrogel or using a membrane with different size.

Table 3.2. Temperature responsive water flux fitting parameters (Eq. 3-4) by error function ($T_c = LCST$; ΔT are in $^{\circ}C$)

pH	A	B	T_c	ΔT	R^2
4	17.5	50.0	32.4	1.0	0.998
6.3	13.8	30.4	32.3	1.5	0.986
7.3	3.3	4.2	34	5.7	0.995

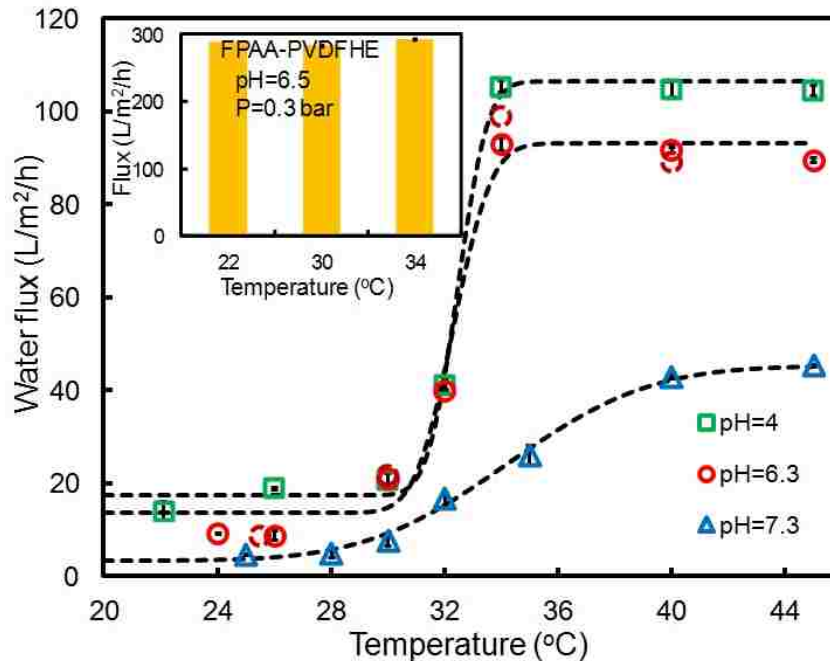


Figure 3.12. Temperature and pH effects on the pure water flux at 3.8 bar through PNIPAAm-FPAA-PVDFHE Ultura membrane. For the polymerization, the NIPAAm concentration was 13 wt%, cross-linker was 1mol%. The inset is the temperature effect on the full-scale FPAA-PVDFHE Ultura membrane (pH=6.5, P=0.3 bar). All the flux Data were corrected with viscosity. Data are fitted by error function. Dark red broken circles represent the flux data obtained with different temperature at pH=6.3 after the run at pH=7.3 to check the stability and reversibility.

It should be noted that after the run at pH=7.3, another run with different temperatures at pH=6.3 was conducted (dark red broken circle in Figure 3.12). The same flux data indicates that the pH and temperature-dependent changes in water flux are completely reversible. The change in flux in response to pH can be caused by the conformation change of acrylic acid polymer chain in the PNIPAAm-FPAA-PVDFHE Ultura membrane. It also shows that at higher temperature, the pH sensitivity is also enhanced. When the temperature is higher than 32°C (above LCST), the water flux exhibits a more marked increase with the pH decreasing from 7.3 to 4 (Figure 3.12). This may be because the PNIPAAm polymer collapses and becomes hydrophobic at temperature above LCST. More ionized carboxylate groups at higher temperature[191], allows the enhanced interaction between PAA chains and water[189]. As a consequence, pH sensitivity at higher temperature is increased. Furthermore, the temperature sensitivity increases in the lower pH range. As shown in Figure 3.12, the flux showed more obvious change at pH=4 than pH=7.3. This phenomenon can be explained that the PNIPAAm chain will play a predominant role when the PAA polymer chain exhibit a helical conformation at lower pH[151, 192, 193]. More PNIPAAm chain will interact with water leading to a higher temperature sensitivity.

Furthermore, as documented, the PNIPAAm-PAA copolymer can shift the LCST to higher temperature, or even worse, can cause the loss of temperature responsivity at higher pH value[194]. However, in this work, the results (Figure 3.12 and Table 3.2) shows pH and temperature response are independent and the pH values has negligible effect on LCST. This may be because PNIPAAm and

PAA are chemically independent with the formed interpenetrating network (IPN)[195] by post polymerization of NIPAAm (cross-linked) within the cross-linked PAA gel network. It also offers more favorable mechanical properties when compared with individual cross-linked network[122]. Therefore, it can broaden the system to very sensitive application, such as, drug delivery. Also, the alterable water flux can be utilized as a sensor and valve to control the liquid transfer process by temperature response.

Since the polymer was not covalently bonded with the membrane, a natural question might be raised about the stability of the membrane. Firstly, the reversible temperature and pH responsive properties can be cycled repeatedly as shown in Figure 3.11 and Figure 3.12. Secondly, to check the long term stability of the membrane, the water flux and responsive properties of a same membrane sample were tested over two experimental periods which were 6 months apart. The water flux slightly decreases from 14 L/m²/h to 12 L/m²/h at pH=6.3 and T=23°C during the 6 months time interval. In addition, the temperature responsive on-off ratio was reduced from 6.8 to 6.4 calculated from the ratios of permeability at 40°C to that of 25°C at pH 6.3. The on-off ratio also slightly decreased from 4.6 to 4.3 for pH 4 to pH 7 at T=25°C. These data confirm the stability of the responsive membranes and the promising potential in controlled separation or drug release applications.

3.3.7 Dextran Rejection through PNIPAAm-PVDF Membranes

The dramatic change of pore size of the thermo-sensitive membranes makes it possible to separate molecules with different size. To evaluate the

temperature effect on the separation behavior, dextran was utilized and the rejections with respect to temperature are shown in Figure 3.13 and Figure 3.14. The dextran molecular weight is 2,000,000 g/mol and the feed concentration is 2 g/L. For both PNIPAAm-PVDF (Millipore) and PNIPAAm-FPAA-PVDFHE (Ultura) membranes, the flux of solution increases, while the dextran rejection decreases with the increasing of temperature. The reduction of rejection can be explained by the pore size increasing, which leads to more molecules transport through the pore at higher temperature. To further prove the rejection results, GPC experiment was conducted to evaluate the dextran concentration before and after the dextran permeation and the result is shown in Figure 3.15. PNIPAAm-PVDF Millipore membrane (5% NIPAAm with 5% cross-linker) (Figure 3.13) was used as an example and the result shows that as expected, at lower temperature with higher rejection (almost 100%), the dextran concentration in the permeate is almost 0, which is consistent with that of TOC results.

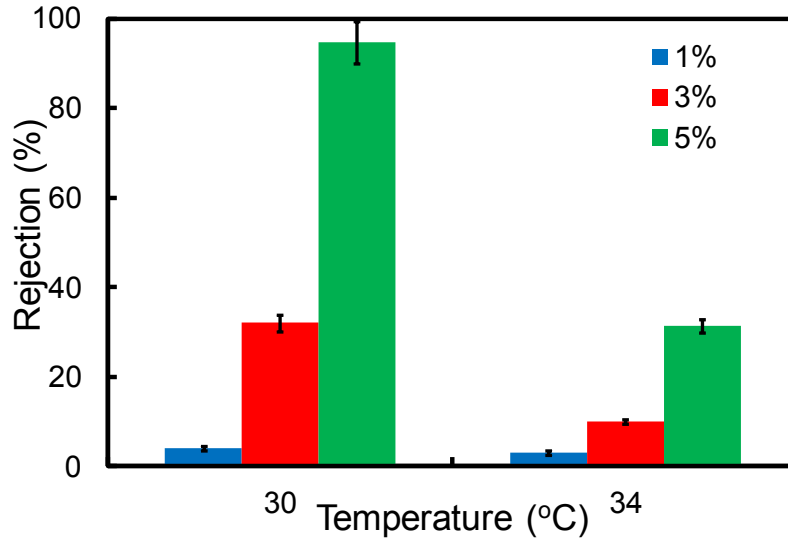


Figure 3.13. The effects of temperature and monomer concentration on dextran rejection with PNIPAAm-PVDF Millipore membrane (5mol% cross-linker) ($M_w=2,000,000$ g/mol; stoke radius $r_s= 26.1$ nm, calculated from $r_s=0.27 \cdot M_w^{0.498}$).

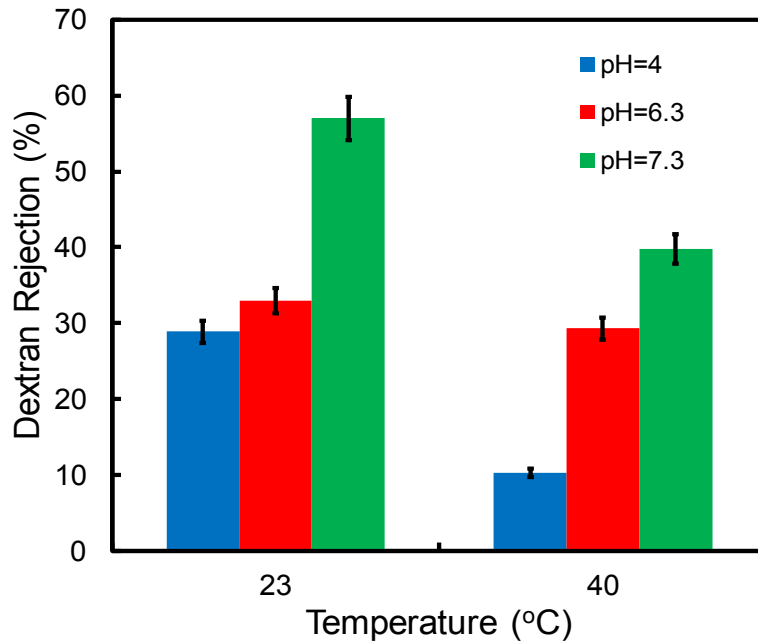


Figure 3.14. The effects of temperature and pH on dextran rejection of PNIPAAm-FPAA-PVDF Ultura membrane ($M_w=2,000,000$ g/mol; stoke radius $r_s= 26.1$ nm, calculated from $r_s=0.27 \cdot M_w^{0.498}$).

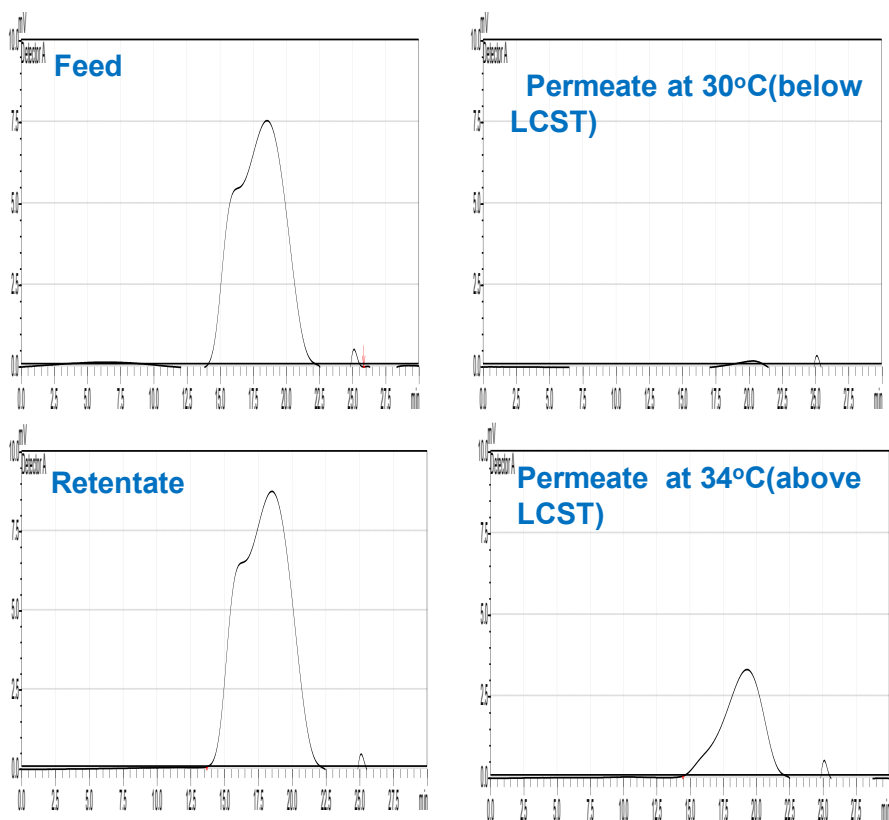


Figure 3.15. GPC results of dextran rejection with PNIPAAm-PVDF Millipore membrane below and above LCST (PNIPAAm-PVDF membrane was made of 5% NIPAAm and 5% cross-linker).

The monomer concentration effect on the dextran rejection was also investigated as shown in Figure 3.13. The dextran rejection is obviously increased from 5% to 95% (30°C) with the monomer concentration increasing from 1% to 5%. The pH effect on the dextran rejection through PNIPAAm-FPAA-PVDFHE Ultra membrane was also investigated as shown in Figure 3.14. It indicates that at constant temperature, the dextran rejection increase with the increase of pH from 4 to 7.3. This result is in good agreement with the swelling and shrinking of PAA chain in membrane pores. At pH 7.3 above pKa (~4.5), the PAA chain swells and reduces the pore size which subsequently decrease the pore size of the membrane and increase the mass transfer resistance,

resulting the high dextran rejection. For better comparison, the dextran rejection through full-scale FPAA-PVDFHE Ultura membrane at different pH was also studied, which shows no rejection at pH=4 and 6.3, and only 9% rejection at pH=7.3. This confirms that the significant increase of dextran rejection through PNIPAAm-FPAA-PVDFHE Ultura membrane is due to the formed temperature responsive PNIPAAm chains in the membrane.

3.3.8 Na₂SO₄ Rejection through PNIPAAm-FPAA-PVDFHE Ultura Membranes

To further illustrate temperature effects on the nanofiltration type separation properties, single salt rejection studies were performed using 100 mg/L and 1000 mg/L Na₂SO₄ at different temperatures as shown in Figure 3.16. The salt rejection is based on both steric exclusion and donnan exclusion. Therefore, Na₂SO₄ rejection through full-scale FPAA-PVDFHE Ultura membrane was firstly studied as a control experiment to eliminate the charge effect by PAA. The result shows 12.2% rejection at 25°C, 11.5% at 30°C and 5.3% at 34°C at pH=6.5, which is attributed to the high salt diffusion through the membrane at higher temperature [196]. On the other hand, for PNIPAAm-FPAA-PVDFHE Ultura membrane, the rejection increased to 32% at temperature below LCST and 25% at temperature above LCST because of the more dominated steric exclusion than donnan exclusion. It should be noted that the increase of the salt concentration from 100 mg/L to 1000 mg/L reduces the Na₂SO₄ rejection from 30% to 5% (25°C), which is reasonable because as the salt concentration increases, the electrostatic repulsion between polymer chains reduces, so the interaction

between salt and membrane decreases leading to the less rejection of salt[196]. These results will be more important because this separation properties through polymer filled membrane can be switched from molecules selective from ultra-filtration to micro-filtration or even just filtration (transport of all molecules) through only the temperature and pH change.

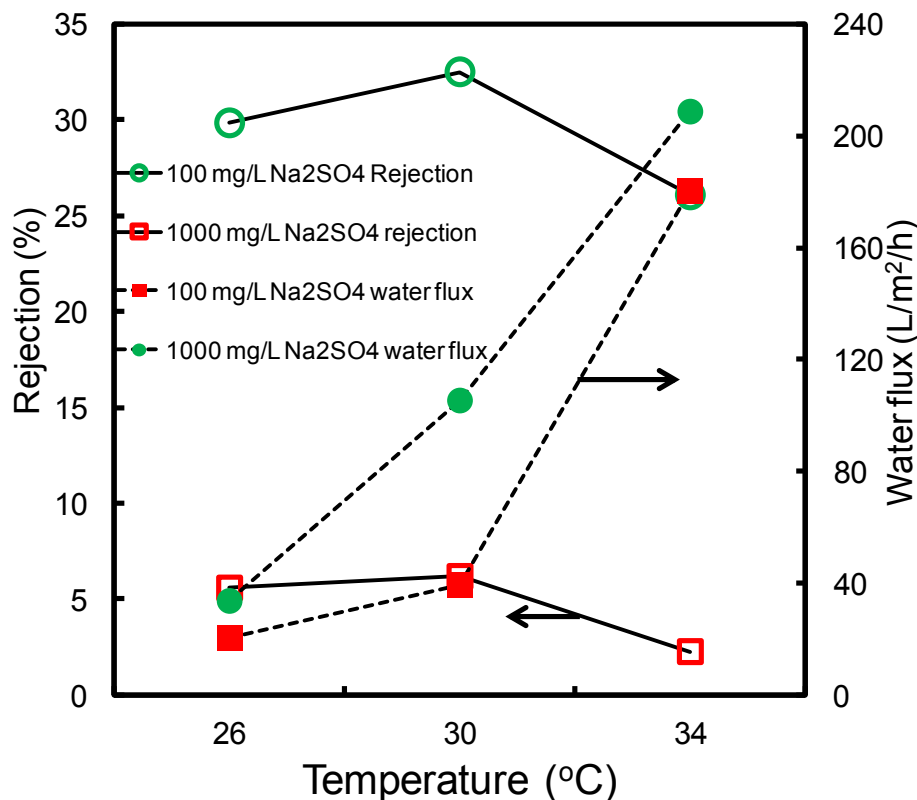


Figure 3.16. Na₂SO₄ rejection through PNIPAAm-FPAA-PVDFHE Ulitura membrane at different temperatures (feed conc.=100 mg/L and 1000 mg/L, P=3.8 bar, pH=6.5).

3.3.9 Catalytic Dechlorination

In our previous publication[197], PNIPAAm-PAA hydrogel has been used as support to immobilized nanoparticles and used in the degradation of toxic chloro-organics with improved reactivity by the temperature responsive polymer. In this work, the hydrogel was filled within the membrane to increase the

mechanical strength and can be used under convective flow to reduce the mass transfer resistance. Another advantage is that the nanoparticles amount in the membrane pore can be controlled. As shown in Figure 3.17, after 3 runs, the iron loading amount is increased to about 15 mg. The corresponding flux is also shown in Figure 3.17. With the increase of nanoparticles amount in the membrane, more membrane pores are occupied, causing the reduction of flux. Since the nanoparticles are formed by iron exchange followed by reduction, the free $-COOH$ groups from PAA can also be utilized to capture ferrous ion again. Therefore, the iron loading amount can keep increasing. However this will sacrifice the effective membrane pore size, which in turn requires high pressure for the reaction. By adjusting the iron loading amount, the optimized reaction reactivity can be obtained.

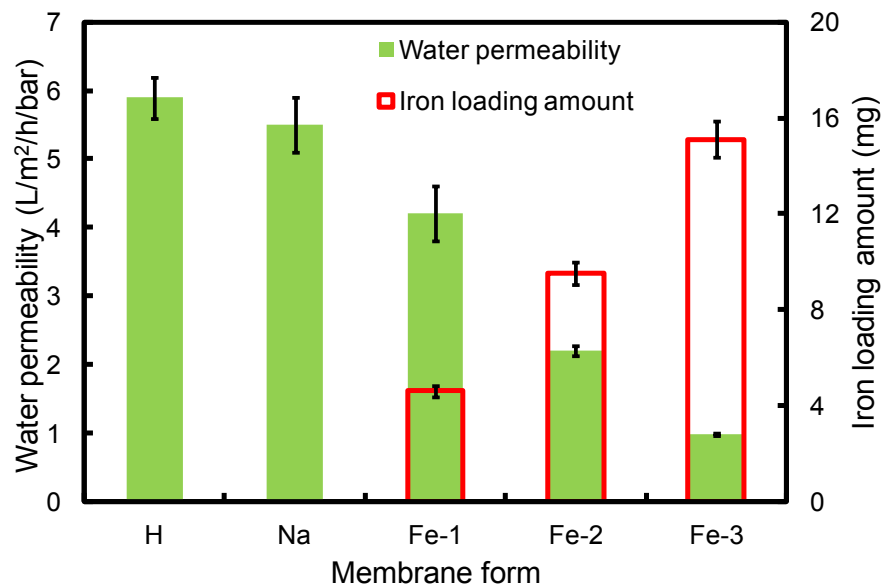


Figure 3.17. Iron loading amount by three times of ion exchange under convective flow and corresponding water permeability through PNIPAAm-FPAA-PVDFHE Ultura membrane. Fe-1, Fe-2 and Fe-3 are iron nanoparticles formed by the 1st, 2nd and 3rd ion exchange.

The nanoparticles were studied for the degradation of trichloroethylene (TCE), an ubiquitous pollutant. The detailed information about using Fe or Fe/Pd nanoparticle for dechlorination can be found in our publications[150, 173, 198]. Pd is used to catalyze the reaction. The reactivity can be calculated by the pseudo-first order model[109, 140]:

$$\frac{dC}{dt} = -k_{SA} \alpha_S \rho_m C \quad \text{Eq. 3-5}$$

Where, C is TCE concentration in water (mg/L); k_{SA} is surface area normalized reactivity(L/m²h); α_S is the specific surface area of nanoparticles (m²/g); ρ_m is the mass concentration of nanoparticles (g/L), t is the time (h).

Figure 3.18 shows the successful degradation of TCE by Fe/Pd nanoparticles (50 nm size as shown in the inset SEM image) with 70% of TCE degradation and 90% of chloride formation as the product within 3 h. The surface area normalized reactivity was calculated to be 0.15 L/m²/h by using **Eq. 3-5**, which is consistent with reported dechlorination reactivity by Fe/Pd nanoparticles[118, 140, 198]. Our previous study shows three times increase of reactivity by using Fe/Pd nanoparticles immobilized in PNIPAAm-PAA hydrogel[197]. Our future work will involve the effect of temperature on reactivity by Fe/Pd nanoparticles within temperature responsive PNIPAAm-FPAA-PVDF membrane. Furthermore, the cooperative work for full-scale membrane manufacturing will continue to optimize the membranes for direct reactive nanoparticles synthesis. For the first time, direct in-situ synthesis of NPs in the full-scale membranes is conducted and thus will enhance the application for on-site groundwater treatment.

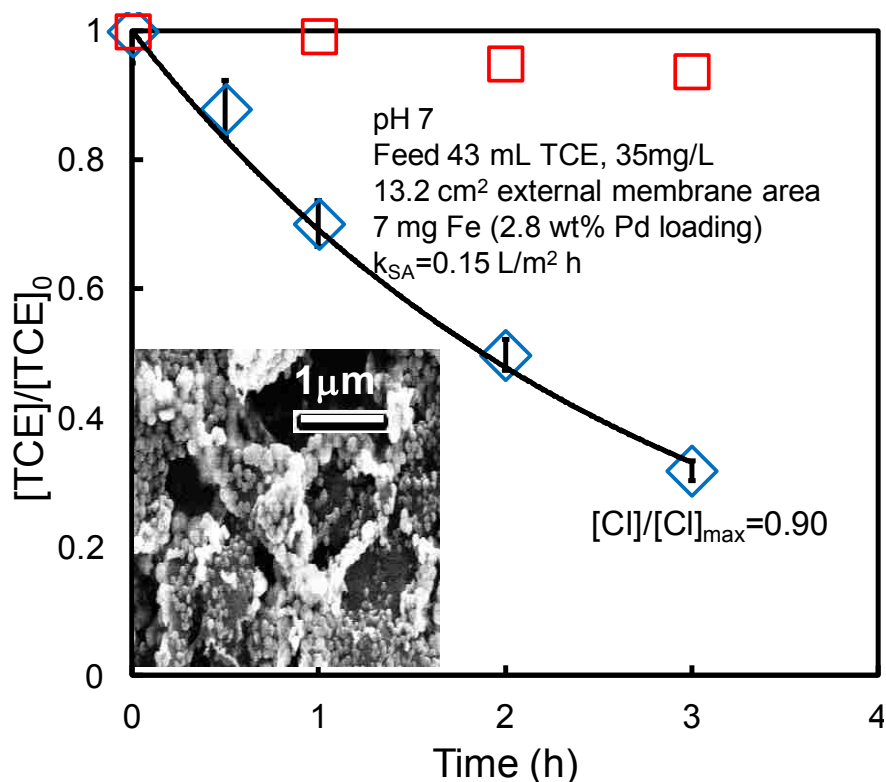


Figure 3.18. TCE dechlorination using Fe/Pd nanoparticles (diamond symbols) in PNIPAAm-FPAA-PVDF Ultura membrane .The inset figure is the SEM image of nanoparticles in membrane pore. The diamond symbols represent the control experiment with only membrane (no metal particles).

3.4 Conclusion

In this study, temperature responsive PNIPAAm-PVDF and both pH and temperature PAA-PNIPAAm-PVDF membranes prepared by pore-filling method with wide range of both monomer concentration and cross-linker were investigated systematically. A rapid and reversible swelling and shrinking of PNIPAAm chains can enlarge and reduce the effective pore size of the membrane. The water flux through the temperature responsive membrane varied by up to 15 times for temperature changes from 30 °C (below LCST) to 34 °C (above LCST). The system can be employed as a sensor or a valve with

temperature response. Dextran solution was used to evaluate the separation properties by this temperature responsive membrane and the result showed dramatic separation performance change by temperature change. To our knowledge, full-scale pore functionalization of PVDF microfiltration membranes to obtain responsive behavior has not been reported in the literature. Direct synthesis of catalytic metal nanoparticles with various loading amounts was established for toxic chloro-organics degradation. This functionalized membrane with tunable size-selectivity and temperature-responsive features can advance the separation process.

3.5 Broad Application Prospect

Conventional separation is mainly based on the size exclusion. However, a novel separation system with diverse separation performance ranging from MF, UF to NF in one single platform via the change of external stimuli can be developed via the utilization of responsive membranes. This system has the potential to be extended to the application in the areas of bioseparation and water treatment, tissue engineering, drug delivery and antifouling surfaces. In addition, the physical property of the membrane pores (such as, pore size and microstructure) and surface composition could be modified through various fabrication methods leading to the improvement of the efficiency of many technological processes.

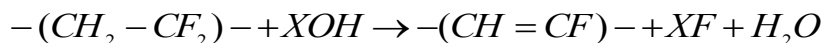
Chapter 4 - Polymerization and Functionalization of Membrane Pores for Water Related Applications

4.1 Introduction

Poly(vinylidene fluoride) (PVDF) is widely studied and used polymers, especially for industrial application due to its excellent chemical and mechanical and UV stability properties[199-201]. PVDF membranes have been extensively used in ultrafiltration and microfiltration for separation process and wastewater treatment, and currently are explored as contactor, and bioseparation[199, 200, 202-205]. A new interesting application is involving the use of PVDF blends to make artificial muscles[206]. In addition, there is increasing interest in membranes with environmentally sensitive functionalities for applications ranging from drug delivery, cell encapsulation, electronic devices, sensors to water softening[207-211].

To obtain desirable applications, PVDF membranes can be chemically and/or physically modified. Methods are currently used including coating[212], adsorption[213], grafting functional groups or graft polymerization to the membranes[189, 200, 214, 215], and chemically modification of membrane materials[216]. Due to its good chemical resistance and high filtration efficiency, PVDF membranes has been widely used for water treatment[217]. In our previous work, we described modification methods to endow PVDF with pH and temperature responsive properties via dip-coating or solvent phase in-situ polymerization[116, 198, 209]. These functionalized membrane were subsequently used as a support to immobilized Fe or Fe/Pd nanoparticles to

remove toxic chloro-organics from groundwater[11, 116]. In this paper, we extend previous studies and present a new method to form covalently bonded PAA onto the PVDF membranes involving chemical treatment of the pristine membrane with alkaline solutions. The reaction mechanism with alkaline degradation of PVDF is shown as following[218-222]:



Where X= Na or K or Li.

The dehydrofluorinated PVDF polymer has formed conjugated double bonds or polyenes structure which can be attacked with specific reactants to introduce functional groups, such as acrylic acid (AA). This creation of covalent bonding can eliminate the concerns on the stability of polyacrylic acid chain on the PVDF membrane prepared by dip-coating or in-situ hydrogel cross-linking method.

The purpose for the creation of functionalized membranes is to be utilized for immobilization of metal nanoparticles for degrade toxic chlorinated organics. As expected, more metal loading leads to higher reaction rate, which requires higher surface area of the support PVDF membranes. Therefore, in this paper, another improvement was developed to modify the pristine PVDF structure. Since PVDF membranes are usually made by phase inversion method induced by immersion of a cast solution in a polymer non-solvent bath[223, 224], the membrane morphology, porosity, flux and retention properties can be affected by the casting and immersion parameters[199, 225, 226]. Herein, in this work, the

sponge-like PVDF membrane is designed to get higher ion adsorption capacity resulting higher nanoparticles loading.

The main goals of present study are to: (1) create dehydrofluorinated membranes for the introduction of proper functional groups through covalently bonding; (2) investigate the effect of alkaline treatment time on the membrane structure; (3) study the pH responsive behavior of functionalized PVDF membrane; (4) prepare sponge-like PVDF membrane with high surface area.

4.2 Experimental

4.2.1 Materials

Sodium hydroxide(NaOH), acrylic acid (AA), ammonium persulfate (APS), ferrous chloride tetrahydrate ($\text{FeCl}_2 \cdot 4\text{H}_2\text{O}$), sodium borohydride (NaBH_4), trichloroethylene (TCE), N, N-dimethylformamide (DMF), lithium chloride (LiCl) were purchased from Sigma-Aldrich. Deionized ultra-filtered water (DIUF) was purchased from Fisher Scientific. The PVDF membrane and PVDF powder(Kynar 761) ($M_w=350,000$ g/mol) was kindly offered by Ultura Inc. Oceanside, CA. Polyvinylpyrrolidone (PVP) ($M_w=40,000$ g/mol) was purchased from Polysciences, Inc. Ultra-high purity (UHP) nitrogen gas used in flux experiments was purchased from Scott Specialty Gases. All the chemicals were used without further purification.

4.2.2 Dehydrofluorination of PVDF Membrane (Def-PVDF)

A piece of PVDF membrane was soaked in 15 wt% NaOH solution in 40 mL DIUF for 10 min. Then, the membrane was sandwiched between two glass

plates and placed in an oven at 70°C to react for 1h, 3h and 22h, respectively. The final membranes were washed with DIUF until the pH became neutral.

4.2.3 PAA functionalization of PVDF membranes (PAA-Def-PVDF)

The dehydrofluorinated PVDF membrane was functionalized with polyacrylic acid (PAA) by free radical polymerization. The polymerization reaction was performed in aqueous phase. The polymerization solution contained 11.1 wt% acrylic acid (monomer) and 0.4 wt% of APS (initiator). The PVDF membrane was dipped in the polymerization solution for 5 min, sandwiched between two glass plates and placed in an oven at 90°C for 2 h.

4.2.4 Preparation of Spongy PVDF Membranes (SPVDF)

The spongy PVDF membranes were made by phase inversion method. The casting solution was made of 20wt% PVDF, 2wt% PVP, and 78wt% DMF and heated to 50°C. A film of PVDF solution was first casted on a glass plate (23-25% humidity), and then immersed in water solution at 50 °C for coagulation. After 10s, the formed membrane was put in pure water at 23 °C to wash and le dried in the oven. The full-scale SPVDF was also fabricated under same condition in Ultura Inc. Oceanside CA to check the feasibility of continuous manufacture of membranes.

4.2.5 Attenuated Total Reflectance Fourier Transform Infrared (ATR-FTIR)

Attenuated total reflectance Fourier transform infrared (ATR-FTIR) (Varian 7000e) was used to determine the presence of functional groups in dehydrofluorinated PVDF and functional membranes. The samples were placed

on the diamond crystal and the spectrum was obtained between 500 and 4000 cm^{-1} for 32 scans at a resolution of 8 cm^{-1} .

4.2.6 Scanning Electron Microscopy (SEM)

The surface and cross-section morphology of the blank PVDF, Def-PVDF, functionalized membranes, and spongy PVDF were studied by Hitachi S-4300 Scanning Electron Microscope (SEM). The samples were mounted on the sample studs and a thin layer of gold was sputtered on the sample surface for imaging purpose. The SEM measurements were performed at an accelerating voltage of 10 kV.

4.2.7 X-ray Photoelectron Spectroscopy (XPS) Analysis of Membrane Surface

The surface composition of membrane was characterized using an X-ray photoelectron spectroscopy (Thermo Scientific K-Alpha) with Al/K ($h\nu=1486.6$ eV) anode mono X-ray source. The sample was directly mounted on a sample holder then transferred into the analyzer chamber. The whole spectra of all the elements with much high resolution were recorded with the Avantage software. Each survey spectra was the average of five survey scans.

4.2.8 Water flux Measurement

The water permeability was measured at different pH to study the pH responsive flux behavior of PAA-Def-PVDF. The tested membrane was mounted in a stirred cell (Millipore). The stirred cell containing the feed water with different pH. The cell was pressurized at different pressures using pure nitrogen. Once the membrane flux reached steady-state, volume flux was measured in triplicates by

recording the volume passed in a given time interval. A final run was conducted at pH 4 to test for reversibility.

4.2.9 Na_2SO_4 Rejection

Na_2SO_4 rejection experiments were performed using a stirred membrane cell provided by Millipore with a membrane cross-sectional area of 13.2 cm^2 including a stirring device to minimize the effects of concentration polarization. The feed Na_2SO_4 concentration is 100 mg/L. The permeate sodium concentration is measured with a Varian AA220 series atomic absorption spectrophotometer.

4.2.10 Synthesis of Fe/Pd Nanoparticles in Membrane and Dechlorination

The method for the synthesis of nanoparticles is developed by our group and described anywhere else [8, 150, 197]. The Fe/Pd nanoparticles were made by ion-exchange with Fe^{2+} , sodium borohydride reduction and post palladium coating. The dechlorination was conducted in 40 mL vial. Samples were loaded with nanoparticles and TCE solution at 30 mg/L. The TCE concentration was determined after a certain time interval by extracting the sample with pentane and analyzed by gas chromatography (HP Series II model 58590) with a mass spectrometer (GC-MS). The detailed information about nanoparticles synthesis and dechlorination can be found in literatures[150, 198, 209].

4.3 Results and Discussion

4.3.1 Dehydrofluorination and PAA Functionalization of PVDF

Membranes

The PVDF membranes were treated with 15wt% of sodium hydroxide for different hours. Prior to the treatment, the PVDF membranes were white in appearance. After treatment, a color change was observed for all the membranes from light yellow, deep yellow to even black as shown in Figure 4.1. The ATR-FTIR spectra of blank PVDF, Def-PVDF and PAA-Def-PVDF membranes are shown in Figure 4.2. The characteristic peaks at 1403 and 1600 cm^{-1} are corresponding to $-\text{CH}_2$ and $\text{C}=\text{C}$, respectively (Figure 4.2(B), (C), (D)). This is due to the formation of polyene on the treatment with a change in fluorocarbon groups of PVDF (1000-1250 cm^{-1}) (Figure 4.2(A)). As the increase of treatment time, the intensity of carbon double bond increases. It should be noted that the $\text{C}=\text{C}$ bond is inactive in infrared leading to the lower absorbance intensity at 1600 cm^{-1} [218]. The hydrocarbon at peaks 1350-1450 cm^{-1} and 800-900 cm^{-1} don't change significantly with treatment. As documented in the literatures[218], the polyene could further react with the hydroxyl anion from the base solution, leading to the formation of hydroxyl groups. But oxygen is not observed in the ATR-FTIR spectra of dehydrofluorinated PVDF.

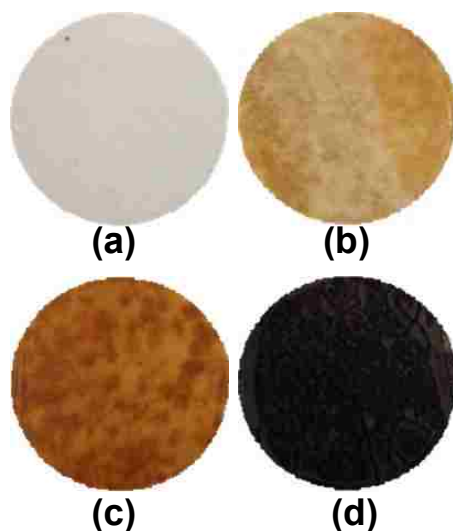


Figure 4.1. Change in color of the PVDF membranes after treatment with 15% of NaOH for different hours at 70°C: (a) 0h, (b) 1h, (c) 3h, (d) 22h.

As for the PAA functionalized Def-PVDF membranes, the appearance of a obvious peak at 1720 cm^{-1} belongs to the $-\text{COOH}$ stretching vibration. It worth to note that no cross-linker was used for the PAA functionalization. Since PAA is highly hydrophilic, they will be washed out if it's not cross-linked. This result together with the ATR-FTIR spectra obviously demonstrate the PAA was successfully covalently grafted onto the surface of the PVDF membrane.

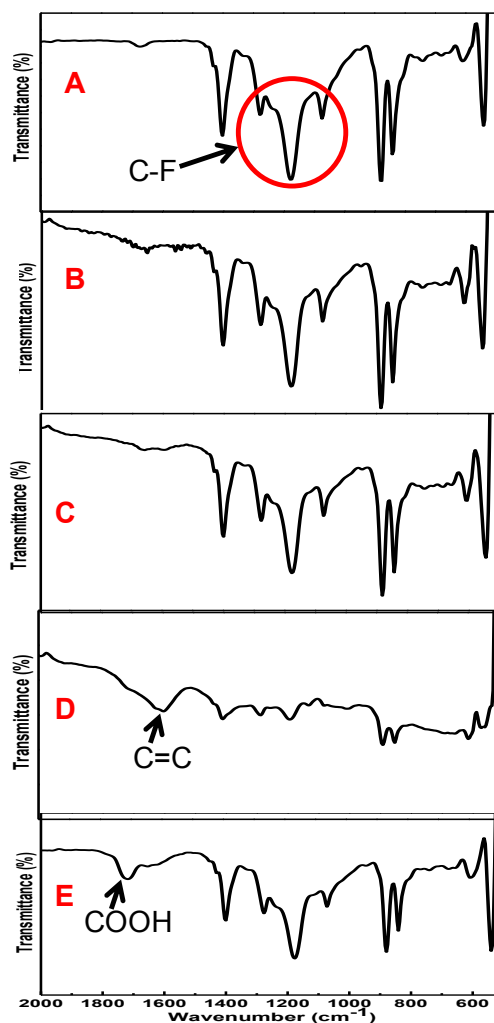


Figure 4.2. ATR-FTIR spectrum of blank PVDF, Def-PVDF and PAA-Def-PVDF membranes. **A:** blank PVDF; **B:** Def-PVDF with 1h NaOH treatment; **C:** Def-PVDF with 3h NaOH treatment; **D:** Def-PVDF with 22h NaOH treatment; **E:** PAA-Def-PVDF (3h's treatment).

4.3.2 SEM Analysis

The morphologies of the blank and functionalized PVDF membranes were characterized by SEM as shown in Figure 4.3. Blank PVDF membrane (Figure 4.3(A)) shows fairly porous structure with mostly circular shape and uniform pore size. The effect of treatment time with NaOH on the structure of membrane was also investigated by SEM shown in Figure 4.3(B) and (C). When treated with less

time (such as, 1h or 3h), no change of membrane surface was observed as shown in Figure 4.3(B). While when treated for 22h, large pores are formed on the membrane surface (Figure 4.3(C)). The membrane is also easy to crack with less mechanical strength due to the loss of fluorine by dehydrofluorination. From Figure 4.3(D), it can be clearly seen that PAA is grafted on the membrane surface and also has a little effect on the structure of the PVDF membrane.

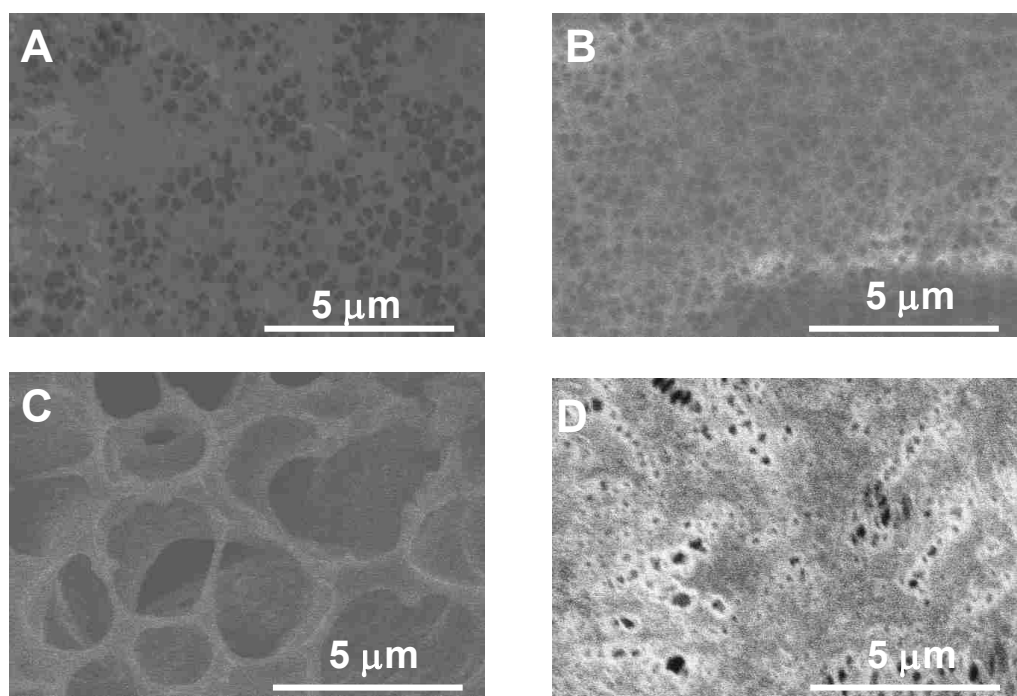


Figure 4.3. SEM image of blank PVDF (A), dehydrofluorinated PVDF-3h (B) and -22h (C) and PAA-Def-PVDF(D).

4.3.3 XPS Analysis of PAA-PVDF Membranes

The surface compositions of the blank membrane, dehydrofluorinated PVDF membrane and PAA functionalized dehydrofluorinated PVDF membrane were investigated by XPS. Figure 4.4 shows the respective survey spectra of these membranes. Compared with blank PVDF membrane (Figure 4.4(A)), the dehydrofluorinated PVDF membrane (Figure 4.4(B)) shows a higher level of

noise due to the change of surface roughness after treated with NaOH solution. The dehydrofluorination is proved by a reduction of fluorine intensity, and relative increase of carbon intensity. The decrease in fluorine concentration and increase in oxygen concentration with time is also shown in Figure 4.5. These quantitative data indicates that most of dehydrofluorination happens in the first hour of the treatment and the rate slows down. As shown in Figure 4.4C, the increase of carbon and oxygen intensity indicates the PAA was grafted on the membranes. Figure 4.6 show the respective C1s core-level spectra of the blank PVDF and PAA-Def-PVDF membranes. The blank PVDF membrane can be fitted with two main peaks at 286eV for CH₂ groups and 290.6eV for CF₂ groups[209, 218]. On the other hand, the C1s spectra of PAA-Def-PVDF membrane can be fitted with five chemical species. The peak with binding energy at 288.5eV belongs to the O-C=O species of the grafted acrylic acid (AA) groups[209]. The peak with binding energy at 286.4eV can be assigned to CO of AA groups and the peak with binding energy at 284.6eV is assigned to CH₂ groups from grafted PAA polymer [217].

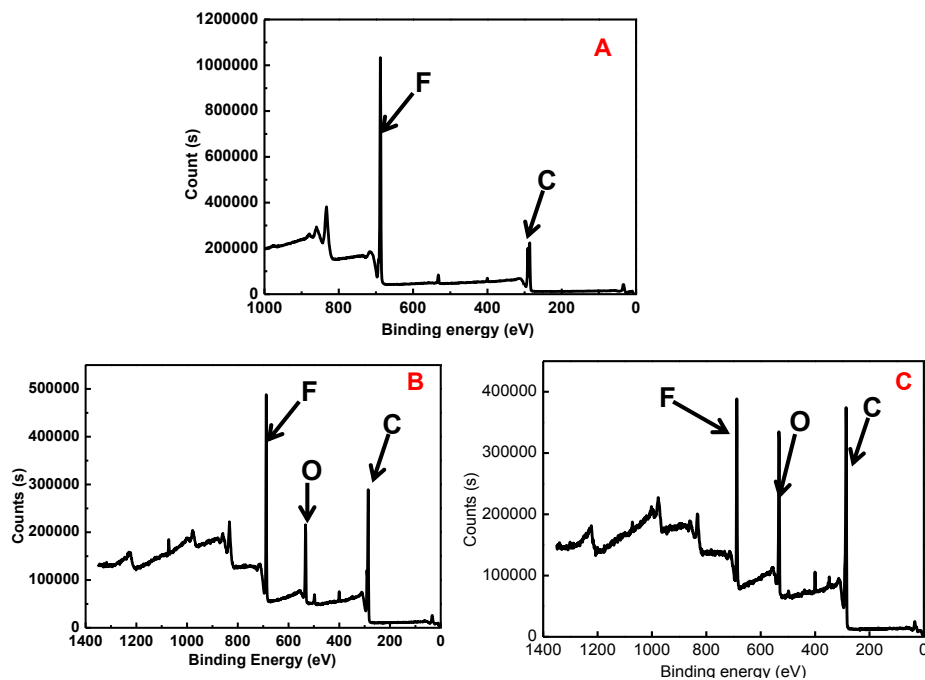


Figure 4.4. XPS survey spectra of PVDF (A), Def-PVDF(B), and PAA-Def-PVDF(C).

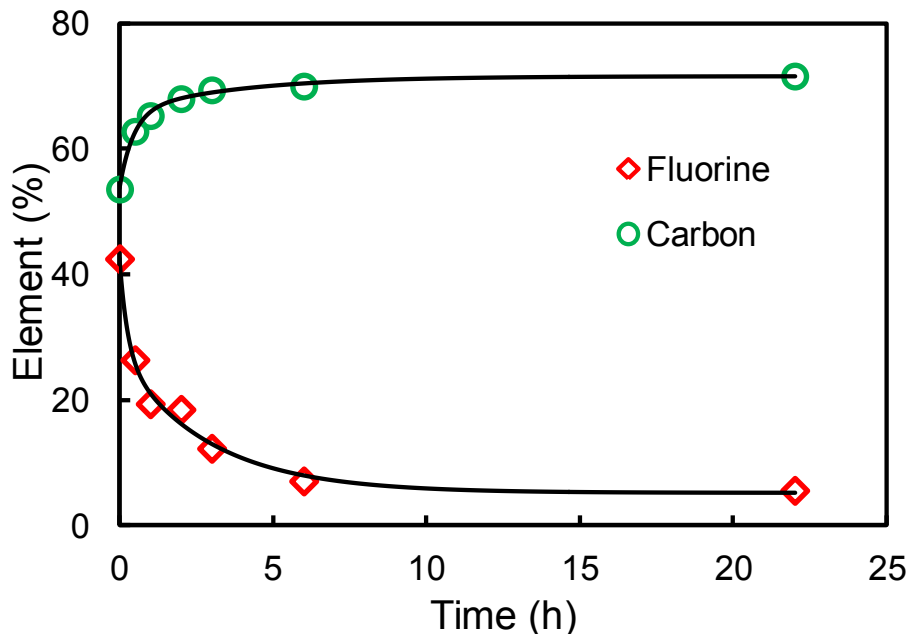


Figure 4.5. Changes in XPS elemental percentages of fluorine and carbon with different treatment time with 6 M NaOH.

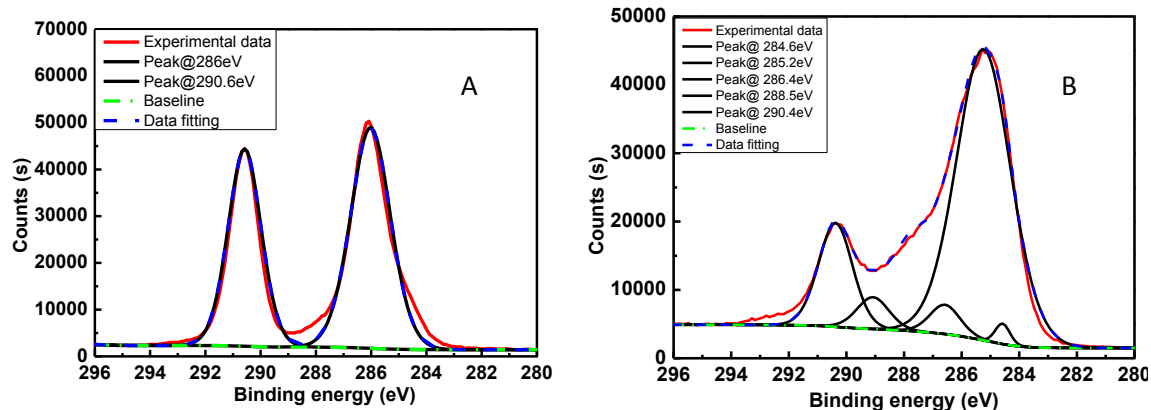


Figure 4.6. XPS C1s core-level spectra of blank PVDF (A) and PAA-Def-PVDF (B) membranes.

4.3.4 Thermal Analysis of Membranes

Figure 4.7 shows the DSC curves of the pristine PVDF, def-PVDF and PAA-Def-PVDF membranes. It's well known that the pristine PVDF membrane is partially crystalline polymer because of its symmetrical structure with a melting point at about 173°C [189]. After dehydrofluorination, the melting point for the Def-PVDF membrane doesn't change as shown in Figure 4.7(b). However, after the covalently binding of PAA on the dehydrofluorinated PVDF membranes, the structural symmetrical structure of PVDF is partially destroyed, resulting the decrease of melting point to 168°C (Figure 4.7(d)). On the other hand, the PAA functionalized PVDF membranes by pore-filling methods showed no obvious change of melting point (Figure 4.7(c)) due to the formation of blends without any chemical bonding. Thus, the DSC results suggest that the grafting of PAA chains on the membrane should impart the membranes with the enhanced and stable functionalities.

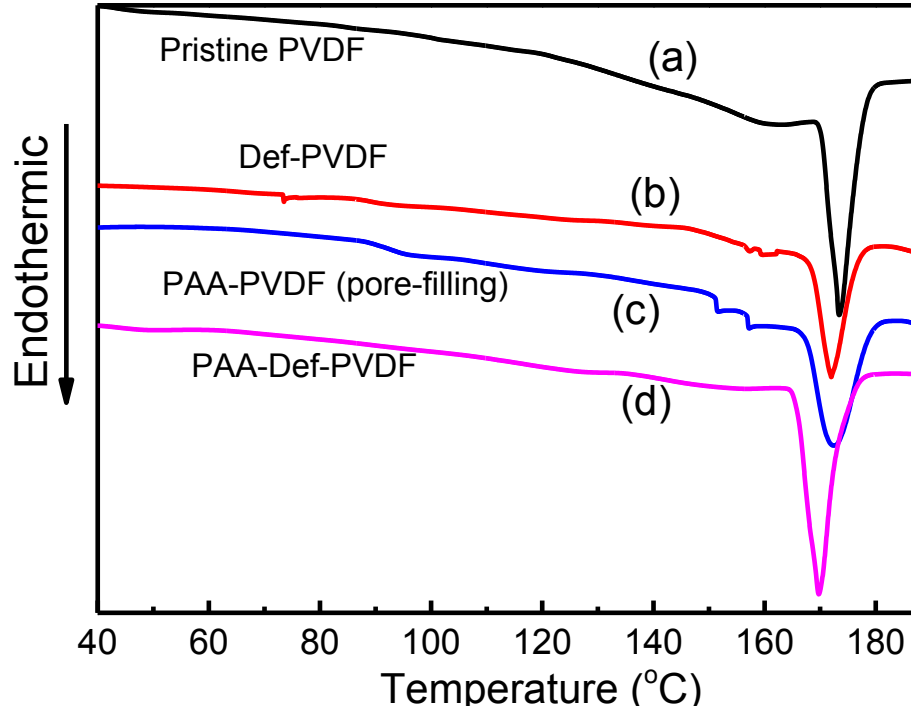


Figure 4.7. DSC thermogram of (a)pristine PVDF, (b) Def-PVDF, (c)PAA-PVDF by pore filling method and (d) PAA-Def-PVDF.

4.3.5 pH Responsive Flux of PAA Functionalized Def-PVDF

Since PAA was presented in the membranes, water permeation through the membrane with pH response would be expected. The pH effects on the water flux of PAA-Def-PVDF functionalized membrane are shown in Figure 4.8. For better comparison, the flux of pristine PVDF membrane, and Def-PVDF under different pressures are also shown in the Figure. As expected, when the membrane was functionalized with PAA, the flux decreases. It also shows that as the pH of feed solution increases, the water flux decreases. This is consistent with previous findings, where similar tests were done with PAA functionalized PVDF membrane by pore-filling method[150]. The change in flux in response to different pH is caused by the conformation change of acrylic acid polymer chain in the membrane. The linear relationship between water flux and applied

pressure and constant flux at pH 4 under different runs indicate that the PAA functionalization on the membrane is very stable.

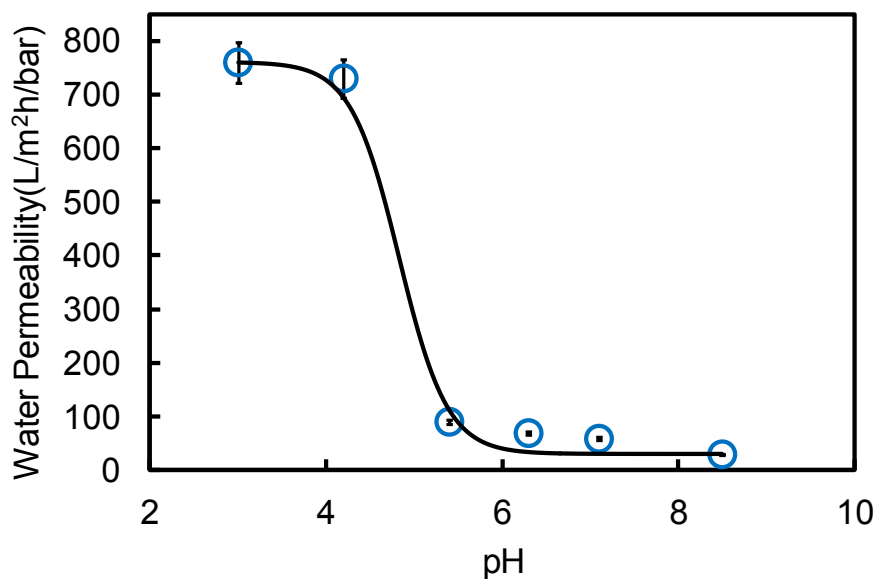


Figure 4.8. pH effect on the pure water permeability of the PAA-Def-PVDF functionalized membrane.

4.3.6 Ca²⁺ Pick-up

The amount of –COOH groups in the functionalized membrane can be characterized by the amount of entrapped Ca²⁺ because the free –COOH groups have high affinity to Ca²⁺. Therefore, 100 mL 1000 mg/L Ca²⁺ solution was permeated through the membrane. The feed and permeate samples were collected and the Ca²⁺ concentration was analyzed by a Varian AA220 series atomic absorption spectrophotometer (AAs). The amount of Ca²⁺ picked up is about 0.015 mmol/cm² membrane area. Based on the ion exchange principles, the assumption is that 1 mol Ca²⁺ can bind to 2 mol carboxyl. Therefore, the calculated –COOH amount is 0.03 mmol/cm². Our previous publication[150] showed that for PAA-PVDF membrane made by pore-filling methods, Ca²⁺

picked up can be ranged from 0.008 to 0.014 mmol/cm² with different cross-linking degree. Here, proper cross-linker amount are required to keep the PAA functionalization stable without washing out. However, too much cross-linking will block the pore and increase the mass transfer resistance. In comparison, the method presented in this work through covalently bonding PAA onto the membrane surface can avoid this problem.

4.3.7 Na₂SO₄ Rejection

The effect of pH on the ion exclusion of the PAA functionalized Def-PVDF membrane is also evaluated and the result is shown in Figure 4.9. When the pH is at 8, the average solute rejection is about 70%. While, at lower pH (around pH=4), the observed rejection is decreased to 10%. This dramatic decrease of solute rejection is because of the helix-coil transitions of the PAA chain based on the pH change[227, 228]. At lower pH, the PAA chain is protonated, which can reduce the overall charge and thus decrease the electrostatic interaction between membranes and permeate ions[229]. When the pH increases to pH=8, the PAA is ionized with enhanced electrostatic interaction and thus higher rejection.

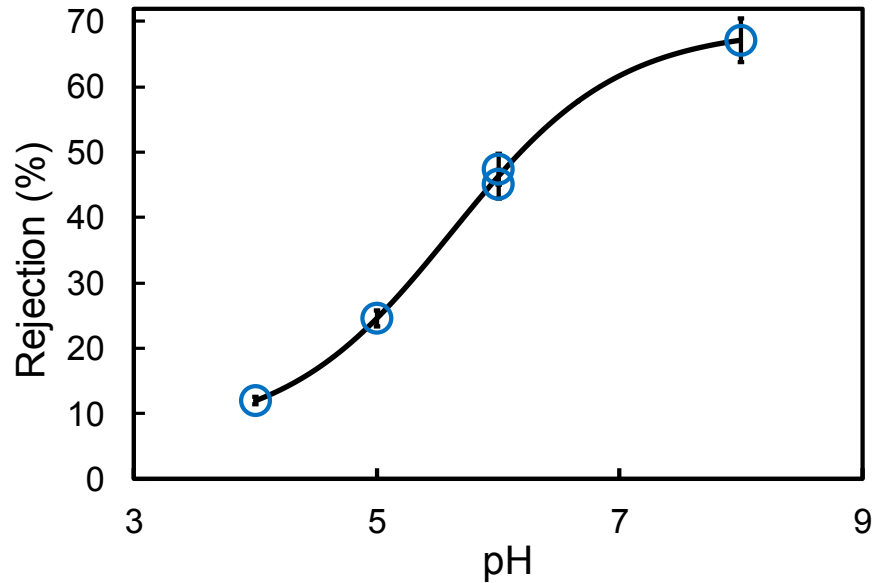


Figure 4.9. Effect of feed solution pH on the ion exclusion (P=0.7 bar) of a 100 mg/L Na₂SO₄ solution through PAA-Def-PVDF membrane.

The dependence of Na₂SO₄ rejection on permeate flux for a PAA functionalized PVDF membrane is shown in Figure 4.10. The observed decline in rejection at higher flux, is in direct contrast to experimental trends generally observed for ion separations in dense media, such as, reverse osmosis (RO), nanofiltration (NF). For NF type membranes, solution rejection increases with the increasing flux due to the reduced effect of diffusion. The microporous membranes used in this study show non-uniform distribution within the pore geometry, primarily due to the incomplete pore coverage resulting from non-uniform functionalization or low chain length to pore ratio. At higher applied pressures, there is enhanced flow through the region without the coverage of PAA chains due the reduction of hydrodynamic thickness of PAA layer[15]. Commercial nanofiltration membranes is reported 95 to 99% Na₂SO₄ rejection. However, these membranes have about 1 nm pore size and are operated under pressures ranging from 10 to 40 bar[230, 231]. This specific experiments involve

the pressure at only about 0.7bar. Therefore, the development of much more effective membranes will require much higher PAA loading and the limitation of the core region.

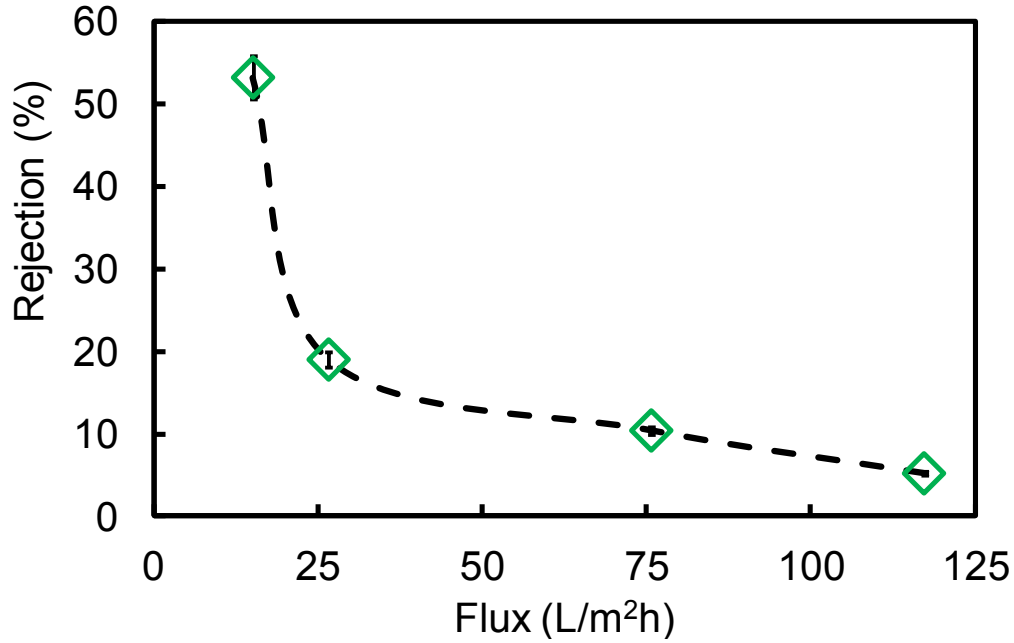


Figure 4.10. Effect of operating pressures on the ion exclusion of a 100 mg/L Na₂SO₄ solution at pH=6.5 through PAA-Def-PVDF membrane.

4.3.8 Reductive Dechlorination

The nanoparticles were used for the dechlorination of TCE, an ubiquitous pollutant. Figure 4.11 shows the successful degradation of TCE with time by Fe/Pd nanoparticles. It can be modeled as a pseudo-first-order heterogeneous reaction[109, 140, 232]:

$$\frac{dC}{dt} = -k_{SA} \alpha_S \rho_m C \quad \text{Eq. 4-1}$$

Where, C is TCE concentration in water (mg/L); k_{SA} is surface area normalized reactivity(L/m²h); α_S is the specific surface area of nanoparticles (m²/g); ρ_m is the mass concentration of nanoparticles (g/L), t is the time (h).

Under the reaction conditions described in Figure 4.11, the k_{SA} is calculated to be 0.11 L/m²h, which is consistent with the literature reported dechlorination reactivity by Fe/Pd nanoparticles[8, 112, 118, 144].

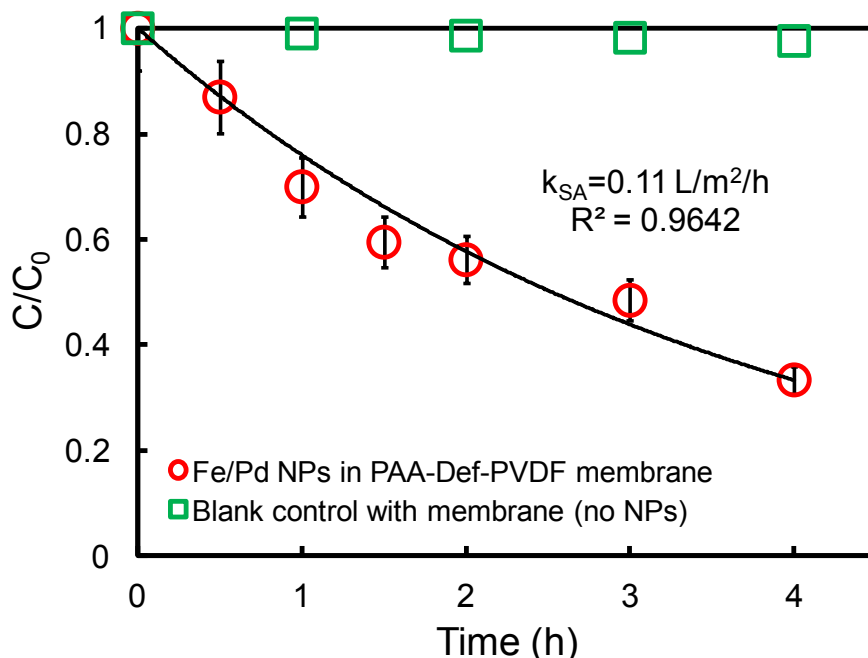


Figure 4.11. TCE dechlorination by Fe nanoparticles immobilized in PAA-Def-PVDF membrane. Vol.=43 mL, initial pH=6.8, initial TCE concentration: 30 mg/L, iron loading amount: 0.2 g/L (Pd=1.4wt% of Fe), Temp.= 25 °C.

4.3.9 Spongy PVDF Membranes (SPVDF)

The SPVDF membrane was prepared by phase-inversion method in lab-scale first. The full-scale SPVDF was also developed to check the feasibility of continuous manufacturing membrane. Both membranes show the same water permeability. In this study, full-scale SPVDF was used to enhance the membrane uniformity and stability. The morphologies of spongy PVDF membranes are shown in Figure 4.12. The cross-section image shows highly inhomogeneous structure with large voids and cavities of different size and shape under the skin layer. The magnified views of the upper and the lower parts of the membrane

cross-section (Figure 4.12(b), (c), (d)) supplies more detailed information on the membrane structure. The membrane exhibits a large number of sponge-like cavities beneath the upper skin layer. The void volume of sponge-like PVDF membrane can be estimated as follows[233]:

$$\text{Void volume(\%)} = [(V_m - V_p)/V_m] \times 100 = \frac{L \times A - (W_m/\rho_p)}{L \times A} \times 100 \quad \text{Eq. 4-2}$$

Where, V_m and V_p are the membrane volume and volume occupied by PVDF polymer respectively. L is the PVDF membrane thickness (cm), A the membrane area (cm^2), W_m is the mass (g) and ρ_p is the density of PVDF and is about 1.78 g/cm^3 . The properties of SPVDF was compared with our previous PVDF from Millipore as shown in Table 4.1. The SPVDF membrane shows high porosity at about 78.6% and almost 4 times higher surface area compared with PVDF (Millipore). Although the SPVDF showed less permeability, the skin layer can enhance antifouling property and the highly porous structure can eliminate the mass transfer resistance[233].

Table 4.1. Comparison of SPVDF and PVDF(Millipore)

Membrane	Thickness (μm)	Porosity	BET surface area(m^2/g)	Permeability ($\text{L}/\text{m}^2/\text{h}/\text{bar}$)
SPVDF	175	78.6%	7.7	32
PVDF(Millipore)	125 ^a	70% ^a	2.1	4400 ^b

^a: Supplied by manufacturer; ^b: Smuleac et al[150].

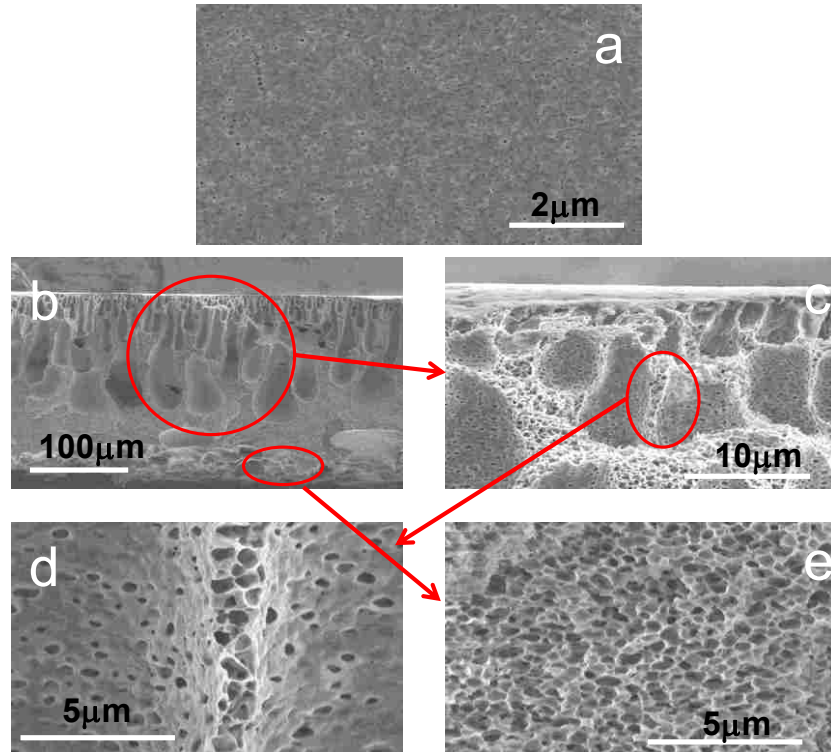


Figure 4.12. SEM images of surface and cross-section spongy PVDF morphology under different magnification (a) surface, ×15k; (b) cross-section of whole picture, ×300; (c) skin surface and macroporous matrix, ×4k; (d) microporous matrix under skin surface, ×10k; (e) interconnected fibrous structure in the microporous matrix, ×10k.

With more surface area, a higher grafting yield will be expected. Therefore, these two membranes were functionalized with acrylic acid under same condition. The morphology of membrane after functionalization was characterized by the SEM and is shown in Figure 4.13. The PAA-SPVDF surface shows less porosity and becomes rough (Figure 4.13(a) and Figure 4.12(a)). In addition, by contrast, different regions of cross-sections clearly show the structure difference. As shown in Figure 4.13(b) and (c), the pore inside the SPVDF substrate are filled with small clusters, indicating the formation of PAA. The permeability was measured and the ion exchange capacity was evaluated by Ca^{2+} pick up on

these two functionalized membranes. The results are shown in Table 4.2. As expected, the PAA functionalization on SPVDF shows high grafting yield at about 81.1wt% compared to 13wt% for that on PVDF(Millipore). The adsorption capacity of the PAA-SPVDF increases in the first 1h, then varies a little and remains constant at 3.2 mg/cm^2 (265.1 mg/g). The PAA-SPVDF membrane shows high ion-exchange performance with almost 10 times higher than PAA-PVDF(Millipore) as shown in Table 4.2. The SEM-EDS spectra shows the elemental composition and distribution of species and gives the atom ratio of 3.3 (oxygen over Ca) (Figure 4.14). This value agrees well with the established PAA-metal binding stability constant[234].

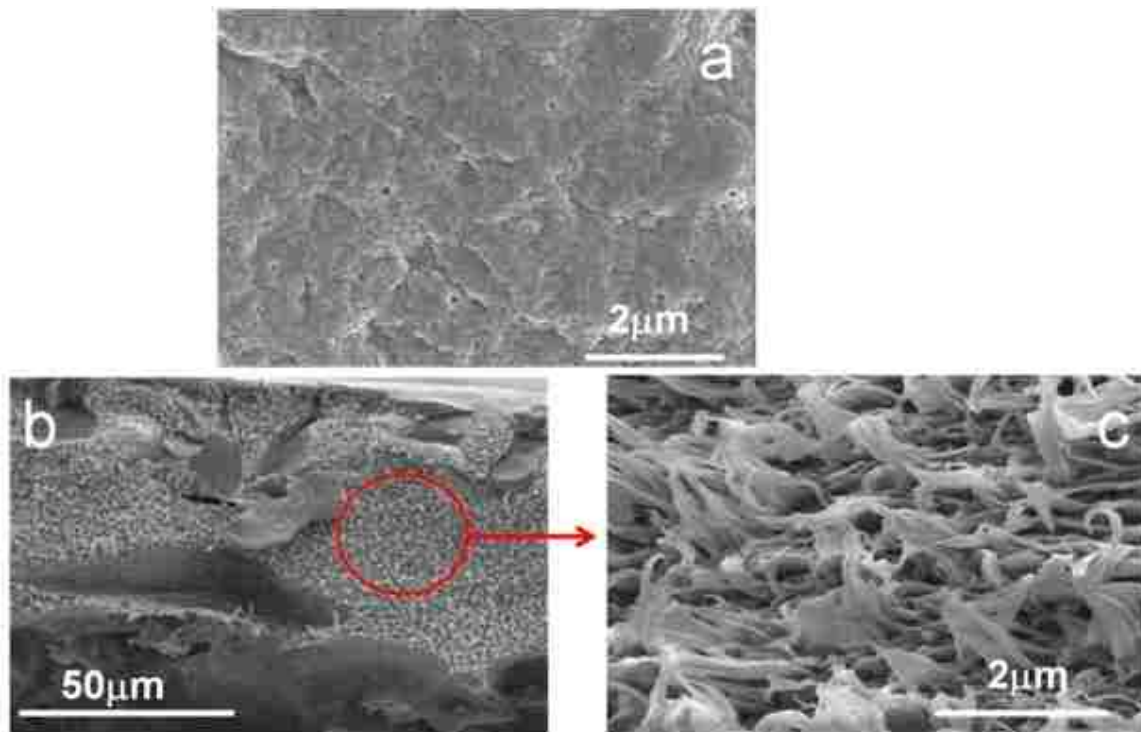


Figure 4.13. SEM image of surface and cross-section of PAA-SPVDF morphology (a) surface, x15k; (b) overall of cross-section, x1k; (c)magnified structure, x15k.

Table 4.2. Comparison of PAA functionalization of SPVDF and PVDF(Millipore); adsorption data obtained using 1000 mg/L CaCl₂ solution at pH 6.3

Membrane	Weight gain (%) [*]	Permeability (L/m ² /h/bar)	Adsorption capacity(mg Ca ²⁺ /cm ²)	Adsorption capacity (mg Ca ²⁺ /g membrane) ^{**}
PAA-SPVDF	81.1	5.8	3.2	265.1
PAA-PVDF(Millipore) ^a	13	23	0.32	14.4

* Weight gain from acrylic acid functionalization in pores

** g membrane refers to total weight without support fabric

^a: Smuleac et al. [33]

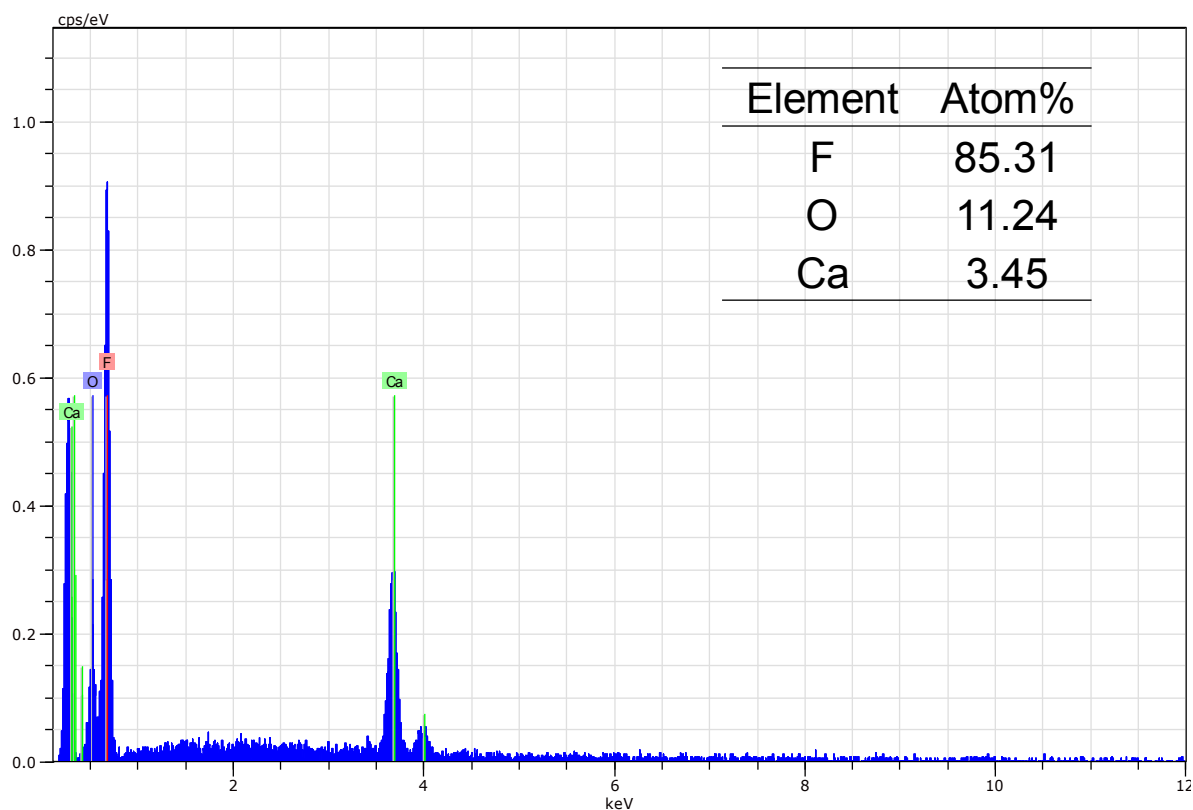


Figure 4.14. SEM-EDS spectra of PAA -SPVDF membranes loaded with calcium ions.

4.4 Conclusion

The PVDF membrane treated with alkaline solution leads to a modified polymer (Def-PVDF) with conjugated double bonds confirmed by ATR-FTIR and XPS spectra. The introduced double bonds make it suitable for the covalently attached PAA polymer. The PAA-Def-PVDF membrane shows pH responsive behavior on both the hydraulic permeability and solute retention. This porous medium offers less resistance to solvent transport, allowing for higher permeation rates at much lower operating pressures with less energy consumption. The PAA-Def-PVDF membrane was also utilized as a support to immobilize metal nanoparticles to remove toxic chlorinated compounds (such as, TCE) from water. The asymmetric membrane with macroporous sponge-like structure was successfully prepared by phase inversion method in both lab-scale and large-scale. The modified PVDF membrane shows high surface area, high porosity and higher yield of PAA functionalization compared to normal PVDF membrane. The ion-exchange capacity of Ca^{2+} is 3.2 mg/cm^2 (265.1 mg/g) with 10 times higher than normal functionalization. The PAA-SPVDF membrane can be used to remove heavy metal ion from water due to its good ion-exchange property. These two modifications of PVDF can extend the development of functionalized membrane with more applications.

4.5 Broad Application Prospect

The introduction of double bonds through alkaline treatment allows the enhancement of surface hydrophilicity of membrane surface and creates active sites for covalently attachment of different functional groups with high stability

and advanced membrane performance. For example, the PAA functionalized membrane allows the higher solute rejection at higher permeation rate with less energy consumption compared to conventional nanofiltration process. In addition, other groups, such as, hydroxyl and sulfonic acid can also be attached to the membrane through different chemical treatment methods. The membrane fabrication methods have been improved due to the increasing demanding of membrane properties and performance. Some novel and advanced methods including thermally induced phase separation(TIPS), non-solvent Induced phase separation (NIPS) and electro-spinning have been reported allowing membranes with good properties, interesting morphology and high performance.

Chapter 5 - Nanofiltration of Sugar Containing Salt: Interaction between Sugar and Salt on Retention

5.1 Introduction

Nanofiltration (NF) is a relatively new membrane process between ultrafiltration (UF) and reverse osmosis (RO)[235, 236]. The NF pore size is about 1 nm corresponding to molecular weight cut-off (MWCO) of 300-500 Da[237]. NF are also slightly charged due to the dissociation of surface functional groups. Similar to RO membranes, NF can separate inorganic salts and organic molecules. Compared to RO, NF membranes are characterized to have higher flux, higher rejection of divalent ions, as well as low rejection of mono-valent ions[238, 239]. Due to the advantages of low operating pressure, high flux, low maintenance and operating cost, NF has been applied water treatment, food and beverage processing, paper and pharmaceutical industries[240-244]. Most of NF membranes are made of polyamide, polyester, polyurea or polyurethane formed by famous interfacial polymerization[236, 242, 245]. The interfacial polymerization technique is a polymerization reaction taking place at the interface between two immiscible aqueous phase and organic phase[246, 247]. The solvents, monomers, monomer concentration, ratios as well as reaction temperature and time can affect the morphology, composition, pore size, porosity and the separation performance of the thin composite nanofiltration membranes[240, 242, 248-250]. The interfacial polymerization with piperazine (PIP) and trimesoyl chloride (TMC) are the common materials to be widely used in the fabrication of thin composite layer for NF.

In order to optimize the NF application, it's important to understand the rejection mechanisms of charged solutes, uncharged solutes and mixture of solutes. The major mechanism for the rejection of uncharged solutes is based on size exclusion. For charged solutes, besides size exclusion, the rejection is also involved with electrostatic interaction between charged membrane and charged species[251, 252]. The process streams in food industry usually contains organic components (sugar, protein etc), NaCl, multi-valent salt and etc. A lot of efforts have been devoted to develop suitable membranes for food industry especially for separation of sugar and salts[253-256]. Wang, *et al.* reported the separation of sugar from NaCl solution by NF membranes from Dow Chemical and showed that the rejection of sucrose depends on the NaCl concentration but the sucrose concentration has no effect on the rejection of NaCl [256]. Bargeman *et al.* has also studied the effects of membrane characteristics on the separation of sugar and salt mixture through five different commercial NF membranes with different pore radius and effective thickness[257].

However, commercial available NF membranes is varied in characteristics such as pore size and surface charge, leading to variety performance[84]. In particular, most commercial NF membranes can reject 99% sucrose/lactose, and in the meanwhile, also reject divalent ions (such as, calcium) at high level (90 to 99%)[258]. The development of NF membranes with lower divalent salt rejections while maintaining over 98% sucrose/lactose is highly desirable in order to obtain high quality sucrose/lactose and eliminate the calcium scaling in evaporators with less energy consumption. In addition, the NF permeate with calcium salt (and

phosphates present in dairy) can be converted to Ca-phosphate fertilizer. Thus, to do selective NF separations, minimization of surface charge through modification of interfacial polymerization process and coating technique are required to fabricate NF membranes with high selectivity and high flux. Therefore, this type of NF membrane was developed in full-scale (over 1500 ft) by Urtura, Inc. Oceanside, CA. The goals of this paper are to: (1) evaluate selective rejection of membrane module (2514 spiral wound) with mixtures of sucrose and calcium chloride; (2) investigate the interaction between multi-valent salt (CaCl_2) and sucrose through the change of concentration; (3) understand and evaluate the experimental results by Donnan-Steric-Pore-Model (DSPM) and extended Nernst-Planck model.

5.2 Experimental

5.2.1 Materials

SNF-20 membrane was the target membrane developed by Urtural Inc. Oceanside, CA. For comparison, commercial NF3A membrane provided by Ultra Inc. was also used. These two NF membranes are three-layer thin film and are polysulfone based membranes with a polyamide top layer. $\text{CaCl}_2 \cdot 2\text{H}_2\text{O}$, sucrose, glucose were obtained from Fisher Scientific.

5.2.2 Membrane Characterization

5.2.2.1 Scanning Electron Microscope (SEM)

The surface and cross-section morphology of two NF membranes were studied by Hitachi S-4300 Scanning Electron Microscope (SEM). Membranes

were frozen in liquid nitrogen, fractured, mounted on the sample studs and a thin layer of gold was sputtered on the sample surface for imaging purpose. The SEM measurements were performed at an accelerating voltage of 10 kV.

5.2.2.2 Atomic Force Microscopy (AFM)

The membrane surface was also characterized by AFM (Agilent PicoPlus 3000) using a resonance frequency of approximately 150 kHz in tapping mode. The average roughness (the average deviation of the peaks and valleys height from the mean value) was determined on $2\ \mu\text{m} \times 2\ \mu\text{m}$ membrane area. All AFM images were processed and presented using Gwyddion software.

5.2.3 Apparatus

Membrane permeability experiments were carried out using a cross-flow cell as shown in Figure 5.1. Membrane module (2514 spiral wound, 0.06m (2.5 inch) diameter and 0.36 m(14 inch) long) was used with surface area of $0.59\ \text{m}^2(6.4\ \text{ft}^2)$. The retentate and the permeate are fed back into the tank, so the feed salt concentration keeps constant throughout the testing period. The pressure was set by changing the concentrate and total recycle valves. After the pressure was set, the solution was allowed to permeate through the membrane for at least 30 minutes to achieve steady state. To measure the flux, the permeate was collected in a graduated cylinder for a specified amount of time. This was done 3 times to ensure stability, and multiple samples of both the permeates and the feed were collected for analysis. The concentrate flow rate was kept constant at 2 GPM for every test performed. Pure water fluxes were

measured using RO permeate water to determine the permeability (L_P) of individual membrane (**Eq. 5-1**). The pressure varied from 3.4 to 10.4 bar.

$$L_P = \frac{J_W}{\Delta P} \quad \text{Eq. 5-1}$$

The retention experiments were conducted with neutral components (glucose and sucrose) and mixture of sucrose and CaCl_2 . To investigate the influence of CaCl_2 on the sucrose retention, experiments were performed using feeds with a sucrose concentration of 10 g/L in combination with different concentration of CaCl_2 (2 g/L and 4 g/L). The effect of sucrose concentration on the rejection of CaCl_2 was also studied by using 2 g/L CaCl_2 and sucrose with different concentrations (2 g/L and 10 g/L). Prior to the experiment with different solutions, pure water fluxes were determined at 10.4 bar to evaluate if the membrane has changed or fouled by the previous experiments.

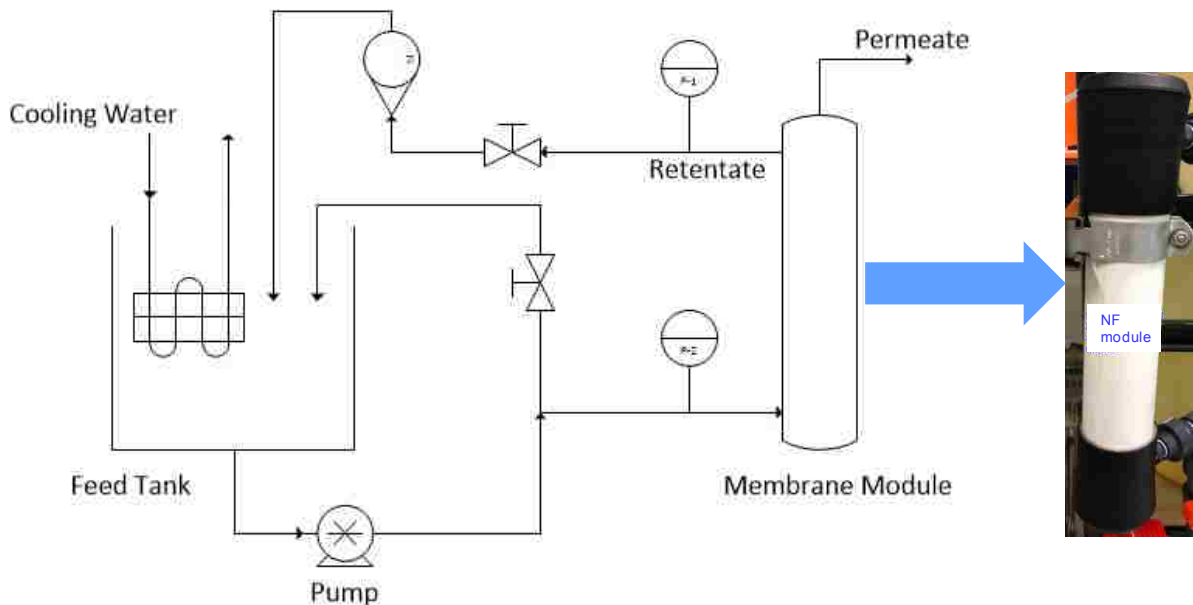


Figure 5.1. Schematic of cross-flow permeating experimental set-up.

5.2.4 Analysis

Sucrose and glucose concentration were measured by total organic carbon analyzer. Carbon standards were prepared in the range from 1-100 mg/L and were used to generate a calibration curve. Samples were automatically introduced to the TOC analyzer (experimental error < 2% with $R^2 = 0.9998$). Ultra-high purity nitrogen was used as the carrier gas at 87.0 psi and a flow rate of 150 mL/min.

The concentration of CaCl_2 were analyzed by conductivity measurements or by using a Varian SpectrAA 220 Fast Sequential atomic absorption spectrometer equipped with a Fisher Scientific hollow cathode lamp. The error of analysis was < 2% with $R^2 = 0.9996$.

5.2.5 Theory

The membrane pore size and thickness was characterized by uncharged solutes (glucose, sucrose or lactose) via fitting the experimental rejection data with Donnan-Steric-Pore-Model [259, 260], expressed as:

$$j_i = -D_{i,p} \frac{dc_i}{dx} + K_{i,c} c_i V \quad \text{Eq. 5-2}$$

$$\text{Where, } j_i = J_v C_{i,p} \quad \text{Eq. 5-3}$$

Where j_i is solute flux ($\text{mol/m}^2/\text{s}$); $D_{i,p}$ is diffusivity (m^2/s); c_i is the solute concentration in the membrane (mol/m^3); V is solute velocity (m/s); x is the distance normal to membrane surface (m).

For uncharged solutes, the transport involves only the diffusion and convection. The $D_{i,p}$ is related with the hindered nature of diffusion ($K_{i,d}$) as following:

$$D_{i,p} = K_{i,d} D_{i,\infty} \quad \text{Eq. 5-4}$$

Assume the membrane pore is uniformly distributed, $K_{i,d}$ and $K_{i,c}$ is related to the ratio of solute size and pore size (λ) as shown in the suggested equations[238]:

$$K_{i,d} = 1.0 - 2.30\lambda + 1.154\lambda^2 + 0.224\lambda^3 \quad \text{Eq.5-5}$$

$$K_{i,c} = (2 - \Phi)(1.0 + 0.054\lambda - 0.988\lambda^2 + 0.441\lambda^3) \quad \text{Eq. 5-6}$$

$$\Phi = \frac{C_{i,x=0}}{C_{i,m}} = \frac{C_{i,x=\Delta x}}{C_{i,p}} = \left(1 - \frac{r_s}{r_p}\right)^2 = (1 - \lambda)^2 \quad \text{Eq. 5-7}$$

Where λ is the ratio of solute radius to pore radius, $C_{i,m}$ is the concentration at membrane surface (mol/m^3); $C_{i,p}$ is the permeate concentration (mol/m^3); $C_{i,x=0}$ is the solute concentration at upper surface ($x = 0$); $C_{i,x=\Delta x}$ is the solute concentration at the lower surface ($x = \Delta x$); r_s is the stokes radius of ions and solutes (m); r_p is the effective pore radius (m).

Eq. 5-2 is integrated across the membrane from the upper surface ($x = 0$) to ($x = \Delta x$) and combined with **Eq. 5-5** to obtain the following expression for rejection:

$$R = 1 - \frac{K_{i,c} \Phi}{1 - \exp(-Pe_m)(1 - \Phi K_{i,c})} \quad \text{Eq. 5-8}$$

Where Peclet number(Pe_m), is defined as,

$$Pe_m = \frac{K_{i,c}}{K_{i,d}} \frac{V\Delta x}{D_{i,\infty} A_k} \quad \text{Eq. 5-9}$$

When Pe_m is close to limit, the asymptotic rejection can be obtained:

$$R_{lim} = 1 - \Phi K_{i,c} \quad \text{Eq. 5-10}$$

The Hagen-Poiseuille equation can be expressed as following:

$$J_w = \frac{r_p^2 (\Delta P - \Delta \pi)}{8\mu (\Delta x / A_k)} \quad \text{Eq. 5-11}$$

The membrane parameters r_p and $\Delta x / A_k$ can be obtained by fitting the solute rejection data by using **Eq. 5-8**.

The bulk diffusivity D_∞ is calculated with Stokes-Einstein equation:

$$D_\infty = \frac{kT}{6\pi\eta r_s} \quad \text{Eq. 5-12}$$

Where k is the Boltzmann constant, T is the temperature, η is the dynamic viscosity and r_s is the radius of the solutes.

The relative viscosity of sucrose related to that of pure water is calculated by the following equation:

$$\eta_{rel} = b \cdot \exp(En_i) \quad \text{Eq. 5-13}$$

Where, b and E are fitting parameters. According to the literature[261], $b=1$ for better prediction of sucrose viscosity at lower concentration; $E=57.19$.

The mole fraction n_i is defined as:

$$n_i = \frac{m}{(55.51 + m)} \quad \text{Eq. 5-14}$$

Where, m is the molality of the solution. Thus, the concentration profile in the concentration polymerization layer can be calculated.

For charged solutes, the extended Nernst-Planck equation was used to study the transport the ions/solutes inside the membranes[262, 263]:

$$j_i = -D_{i,p} \frac{dc_i}{dx} - \frac{z_i c_i D_{i,p}}{RT} F \frac{d\Psi}{dx} + K_{i,c} c_i V \quad \text{Eq. 5-15}$$

j_i is the flux of ion i and the terms on the right side represents transport due to diffusion, electric field and convection, respectively. In this work, the model is used to calculate the effective charge density by fitting the experimental data with single CaCl_2 rejection.

$$z_{\text{Ca}^{2+}} C_{\text{Ca}^{2+}}^0 + z_{\text{Cl}^-} C_{\text{Cl}^-}^0 = 0 \quad \text{Eq. 5-16}$$

$$z_{\text{Ca}^{2+}} c_{\text{Ca}^{2+}} + z_{\text{Cl}^-} c_{\text{Cl}^-} = -X_d \quad \text{Eq. 5-17}$$

Where $C_{\text{Ca}^{2+}}^0$ and $C_{\text{Cl}^-}^0$ are the bulk concentration of Ca^{2+} and Cl^- , respectively; $c_{\text{Ca}^{2+}}$ and c_{Cl^-} are the concentration of Ca^{2+} and Cl^- , and X_d is effective charge density. X_d is assumed to be constant at all points. Eq. 5-15 is rewritten as following:

$$\frac{dc_i}{dx} = \frac{J_v}{K_{i,d} D_{i,\infty}} (K_{i,c} c_i - C_{i,p}) - \frac{z_i c_i}{RT} F \frac{d\Psi}{dx} \quad \text{Eq. 5-18}$$

To solve this equation, Bowen et al[263]. suggested the use of following equations. For this work, CaCl_2 was used as a single salt.

$$\frac{d\Psi}{dx} = \frac{\frac{z_{\text{Ca}^{2+}} J_v}{D_{\text{Ca}^{2+},b} K_{\text{Ca}^{2+},d}} (K_{\text{Ca}^{2+},c} c_{\text{Ca}^{2+}} - C_{\text{Ca}^{2+},p}) + \frac{z_{\text{Cl}^-} J_v}{D_{\text{Cl}^-,b} K_{\text{Cl}^-,d}} (K_{\text{Cl}^-,c} c_{\text{Cl}^-} - C_{\text{Cl}^-,p})}{\frac{F}{RT} (z_{\text{Ca}^{2+}}^2 c_{\text{Ca}^{2+}} + z_{\text{Cl}^-}^2 c_{\text{Cl}^-})} \quad \text{Eq. 5-19}$$

Eq.s 5-18 and **5-19** can be solved by using the following boundary conditions at:

$$x = 0 \quad C_i = C_{i,m}; \quad x = \Delta x \quad C_i = C_{i,p} \quad \text{Eq. 5-20}$$

Where $C_{i,m}$ and $C_{i,p}$ are the feed and permeate concentrations at the interfaces of the membrane.

C_i and c_i can be correlated by the following equation.

$$\frac{\gamma_i c_i}{\gamma_i^0 C_i^0} = \Phi \exp\left(-\frac{z_i F}{RT} \Delta \psi_D\right) \quad \text{Eq. 5-21}$$

Where γ_i is the activity coefficient of species i , and Φ is sterical partitioning term. As diluted systems are studied in this work, the activity coefficients were assumed to be unity.

To correlate the experimental data with the model described above, a calculation routine illustrated in Figure 5.2 was used to obtain the effective charge density X_d . Briefly, an initial guess of X_d is provided to start the calculation routine with a few known inputs listed on the top row in Figure 5.2. A careful examination of **Eq.s 5-18** through **5-21** gives a multipoint boundary value problem (BVP) for ordinary differential equations (ODEs). The complexity of the problem requires solving the problem numerically. Function *bvp4c* embedded in MATLAB was adapted in this work for BVP ODE calculation (see *Appendix*). Specifically, an initial guess of $C_{i,p}$ equal to $C_{i,m}$ is provided to the solver as an unknown parameter which will be solved through iterations. Boundary conditions $c_{i,m}$ and $c_{i,p}$ were calculated by simultaneously solving **Eq.s 5-16** and **5-21** for Ca^{2+} and Cl^- respectively through MATLAB solver *fsolve*. c_i across the membrane

thickness and $C_{i,p}$ were calculated using solver *bvp4c* numerically by 30 equally spaced points. The calculated $C_{i,p}$ is then compared with the experimental $C_{i,p}$. The difference of the two was minimized through a global minimization function *patternsearch* which prevents the search being trapped in local minima in this nonlinear problem.

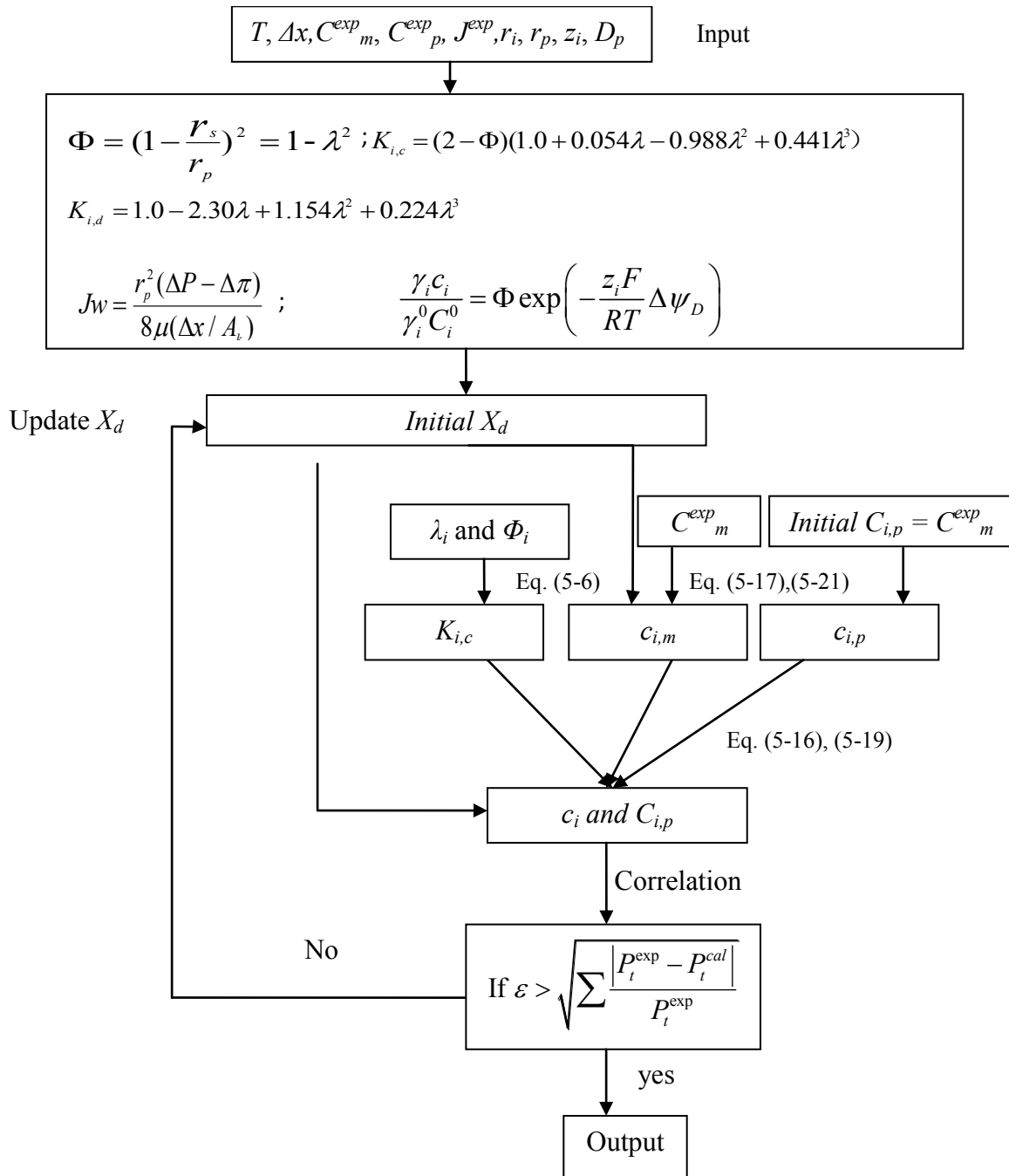


Figure 5.2. Schematic diagram of numeric calculation procedure for effective charge density of nanofiltration membrane using extended Nernst-Planck model.

5.3 Results and Discussion

5.3.1 Membrane Characterization

Membrane structure morphology can affect the separation mechanism and performance. The thickness of membrane is directly related to the resistance of mass transfer. The reduction of membrane thickness can improve the membrane permeability. Therefore, it's important to examine the membrane morphology using SEM and AFM.

5.3.1.1 SEM

Figure 5.3 shows the SEM images of SNF20 and NF3A membranes. It's observed that both membranes comprises three layers of different polymeric materials: polyester backing to increase the stability (not shown in the picture), porous polysulfone layer to reduce the resistance of transport, and the dense but active polyamide layer for selective separation[264]. The surface globular structure is caused by the formation of polymer[265]. From the cross-section images of both membranes, the thickness the active layer can be determined at about 132 nm for SNF20 and 103 nm for NF 3A, respectively. It should be noted that the drying process may cause the observed thickness is less than the real thickness of active layer.

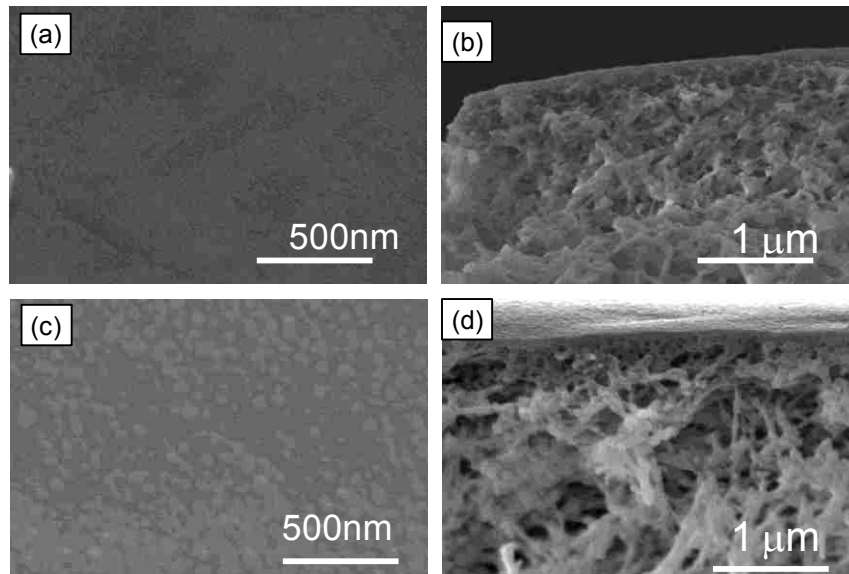


Figure 5.3. SEM image of surface (a) and cross-section (b) of SNF20 membranes, surface (c) and cross-section (d) of NF3A membranes.

5.3.1.2 AFM

AFM was chosen to characterize the surface morphology of SNF20 and NF3A membrane as shown in Figure 5.4. As shown in the figure, the image has light and dark regions. The light region represents the highest points in the membrane, while the dark regions usually contains pores. Average roughness is defined as average deviation of the peaks and valleys from the mean plane and root mean squared (RMS) roughness is the RMS deviation of the peaks and valleys. Roughness is one of the important surface properties, which can affect the mass transfer and is related to the initial membrane fouling behavior. Membranes with higher roughness is tend to be fouled than smooth membranes[266]. The RMS is determined to be 4.7 nm for SNF20 and 10.4 nm for NF3A membrane, respectively. Literatures has reported that NF90 membrane (Dow, USA)has roughness at about 27.8 nm[266]. It's obvious that the SNF20

membrane surface with smaller RMS is considered to be smooth with less fouling potential.

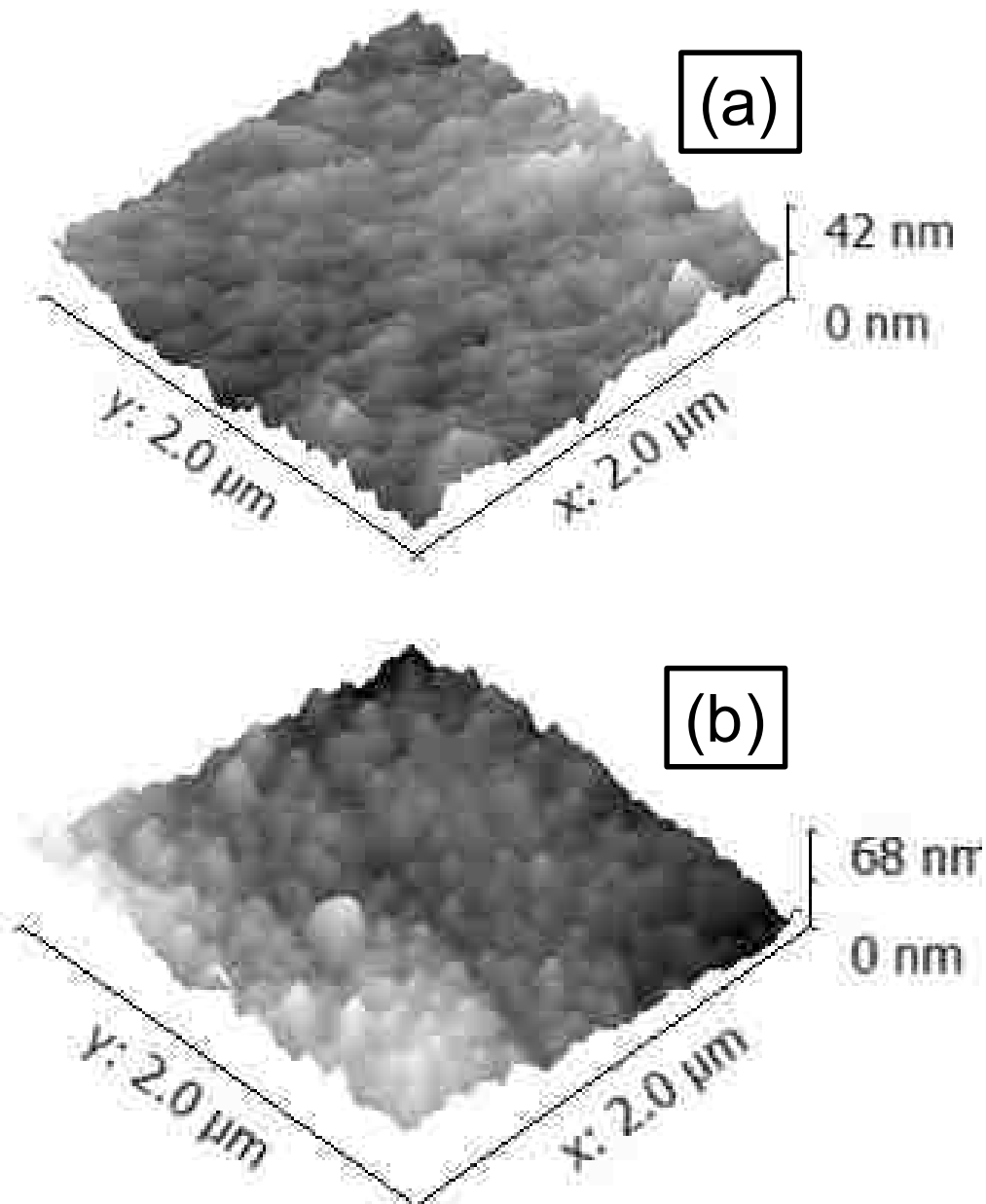


Figure 5.4. AFM image of SNF20 (a) and NF3A(b) membrane.

5.3.1.3 Water Permeability

Membrane module testing was done to establish realistic data that would be expected in a larger scale spiral wound membrane module system. This mode

of testing is unique capability and has many benefits over batch or dead-end cells. The convection caused by the flow across the membrane surface reduces concentration polarization of ions[267, 268]. The module also tests a much high surface area than the batch or dead-end cells, minimizing the effect of any inconsistencies in the membrane. Many tests have been done on the membrane modules to test for rejection and flux using different salts, salt concentrations, and temperatures.

Pure water permeability of SNF20 and NF3A membranes as a function of the applied pressure is shown in Figure 5.5. All the graphs are linear following the Hagen-Poiseuille equation. From Figure 5.5(a) and (b), the water permeability of SNF20 membrane is calculated to be 12.6 L/m²/h/bar, while for NF3A membrane, it is 6.4 L/m²/h/bar. The literature reported permeability of two commercial NF membranes (CK and DK from Osmonics, USA) ranging from 2.4 to 7.9 L/m²/h/bar[238, 257, 269]. By comparison, it's obvious that the water permeability of newly developed SNF20 membrane is much higher than NF3A and commercial NF membranes. In addition, the pure water fluxes for both membranes are almost the same as the flux with 2 g/L sucrose as shown in Figure 5.5(a) and (b), which demonstrates that the concentration polarization is minor for concentration at 2 g/L.

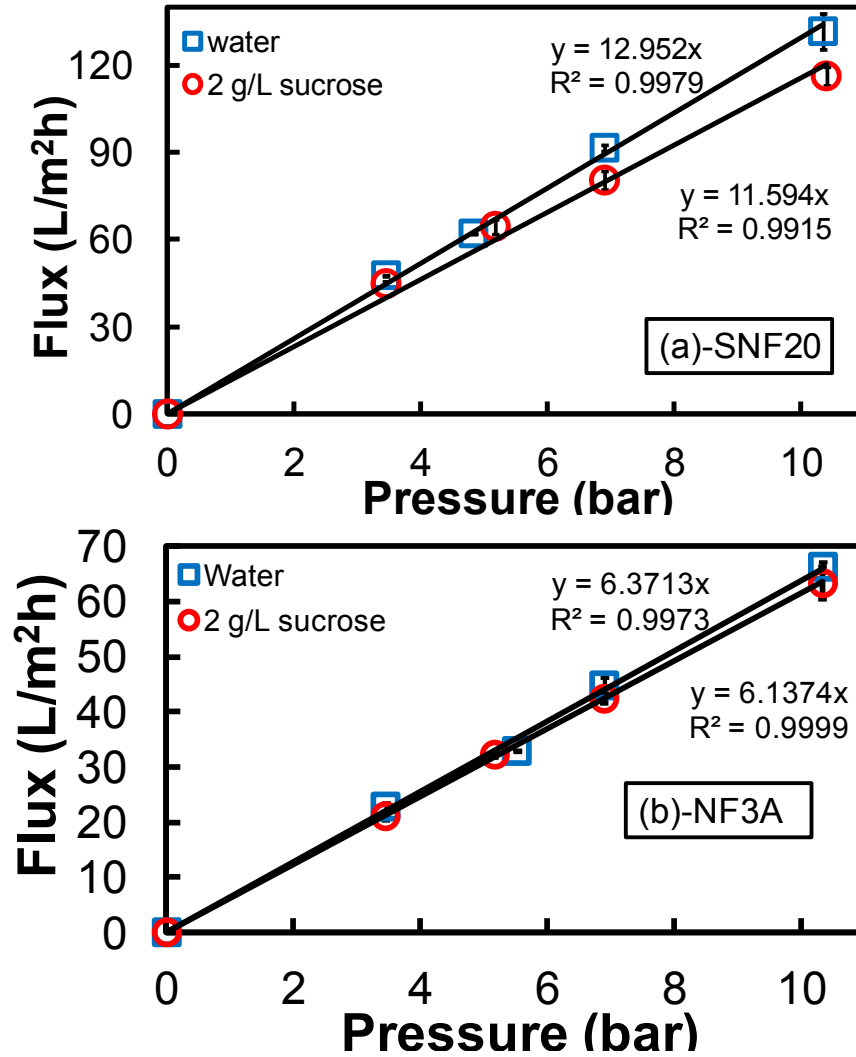


Figure 5.5. Pure water flux and the flux at 2 g/L sucrose versus the pressure of SNF20 (a) and NF3A (b).

5.3.2 The Retention of Single Solute

5.3.2.1 Sucrose and Glucose Rejection

The structural characterization of membrane can be determined by two important parameters (effective pore radius, r_p and the ratio of effective thickness to porosity, $\Delta x / A_k$) through the rejection of two uncharged solutes: glucose and sucrose. The rejection data of sucrose and glucose can be fitted

with DSPM model. The data used in this model for calculation is shown in Table 5.1. Figure 5.6 shows the rejection of two uncharged solutes (glucose and sucrose) for SNF20 and NF3A membranes respectively. Both membranes can reject sucrose well (>99%). It can be seen that the sugar rejection is approached to the limiting rejection when the flux is increased. Based on the rejection data, the effective pore radius, r_p and $\Delta x / A_k$ can be estimated by fitting the experimental data and the results are shown in Table 5.2. The average pore radius for SNF20 membrane is estimated to be 0.53 nm, and $\Delta x / A_k$ is 0.99 μm . While for NF3A membrane, the r_p and $\Delta x / A_k$ are 0.48 nm and 1.67 μm , respectively. The smaller pore size for NF3A membrane explains why the rejection of glucose for NF3A membrane is higher than that of SNF20 membrane. In addition, compared with the $\Delta x / A_k$ of NF(Dow Chemicals, USA) and Desal 5DK (Osmonics, USA) as shown in Table 5.2, the smaller $\Delta x / A_k$ for SNF20 membrane explains the higher water permeability of SNF20 membrane. Using the thickness measured by SEM as shown in Figure 5.3, the porosity (A_k) for SNF20 and NF3A is calculated to be 0.13 and 0.06, respectively. That confirms that the SNF20 membrane has both thinner layer and higher porosity compared with other membranes.

Table 5.1. Input data for bulk values for DSPM model calculation

Sugar	Solute radius (nm), r_s	Conc. (g/L)	Bulk diffusion coefficient (m^2/s)	η (Pa·s)
Sucrose	0.471 [238]	2	4.62×10^{-10}	1.01×10^{-3}
Sucrose	0.471	10	4.50×10^{-10}	1.03×10^{-3}
Glucose	0.365 [238]	2	8.65×10^{-10}	0.94×10^{-3}

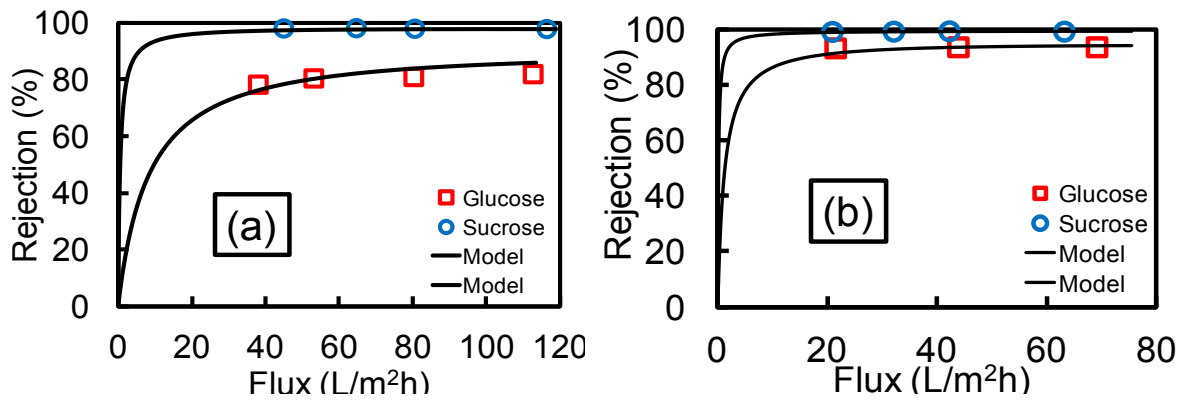


Figure 5.6. Rejection of sucrose and glucose as a function of permeate flux for SNF20 module (a) and NF3A module (b). The line shows fitting with Donnan-Steric-Pore model.

Table 5.2. Calculated pore radius (r_p) and effective thickness over porosity($\Delta x/A_k$)for SNF20 and NF3A membrane obtained by using Donnan-Steric-Pore Model (Eq. 5-2).

Membrane	Glucose		Sucrose	
	r_p (nm)	$\Delta x/A_k$ (μm)	r_p (nm)	$\Delta x/A_k$ (μm)
SNF20	0.52	0.98	0.54	1.00
NF3A	0.46	1.73	0.5	1.61
Desal 5DL(Osmonics, USA)[257]	0.45	2.54	-	-
Desal 5DK(Osmonics, USA)[257]	0.42	2.59	-	-

5.3.2.2 CaCl_2 Rejection

The influence of CaCl_2 concentration on the CaCl_2 rejection for SFN20 and NF3A membrane was investigated and is shown in Figure 5.7. For both membranes, the rejection is decreased with the increase of CaCl_2 concentration. The rejection of CaCl_2 is based on the steric and electrostatic interaction between membrane and salt ions. At low concentration, the high rejection of CaCl_2 is due to the electrostatic repulsion. At higher concentration, the electrostatic interaction reduces and the interaction between salt and membrane decreases leading to lower rejection[270]. The extended Nernst-Planck model can also be used to determine the electrical characteristic of membrane by fitting the experimental data of CaCl_2 rejection. The data used in the model calculation is shown in Table 5.3 and the fitting results is shown in Figure 5.7. It shows that the model fits well with the CaCl_2 rejection of all three concentrations for both

SNF20 and NF3A membranes. It also indicates that the rejection of CaCl_2 increases with the enhancement of pressure, but the effect of pressure on the rejection is not significant for low concentration CaCl_2 . This may be because the solute transport at low concentration is mainly contributed by the diffusion[271].

The effective charge density, X_d can be determined from the model and it's increased with the concentration increases. Figure 5.8 shows the X_d difference as a function of CaCl_2 concentration for SNF20 and NF3A, respectively. The dependence of $|X_d|$ on the salt concentration follows Freundlich isotherm:

$$\log_{10}|X| = s \log_{10} C_b + q \quad \mathbf{5-22}$$

For the case of SNF20, $s=0.9677$ and $q=0.661$. While for NF3A, $s=0.9358$ and $q=1.0113$. Similar relationship has been reported for HC50 (DDS Filtration Advanced Membrane Technology, Denmark) ($s=0.875$, $q=0.999$) and CA20 (Hoechst Separation Products, Germany) ($s=0.499$, $q=0.859$) reported in the literature[272].It indicates that NF3A membrane has higher effective charge density than SNF20 membrane, which is the reason why NF3A has higher salt rejection than SNF20 membrane. It also shows that the rejection of CaCl_2 increases with the enhancement of pressure, but the effect of pressure on the rejection is not significant for low concentration CaCl_2 . This may be because the solute transport at low concentration is mainly contributed by the diffusion[271]. Comparing the separation performance for both membranes, NF3A membrane

performs better than SNF20 due to the high effective charge density as shown in Figure 5.8.

Table 5.3. Input values for known parameters in modeling

Parameter	SNF20	NF3A	Source
r_p , nm	0.53	0.48	Table 5.2
z_i ,	Ca ²⁺ : 2; Cl ⁻ : -1		-
r_s , nm	Ca ⁺ : 0.114; Cl ⁻ : 0.167		[273]
$D_{i,\infty}$, m ² /s	Ca ²⁺ : 0.78e ⁻⁹ ; Cl ⁻ : 2.03e ⁻⁹		[274]
T, K	298		-
F, A / mol	96485		-
R, J/K/mol	8.314		-

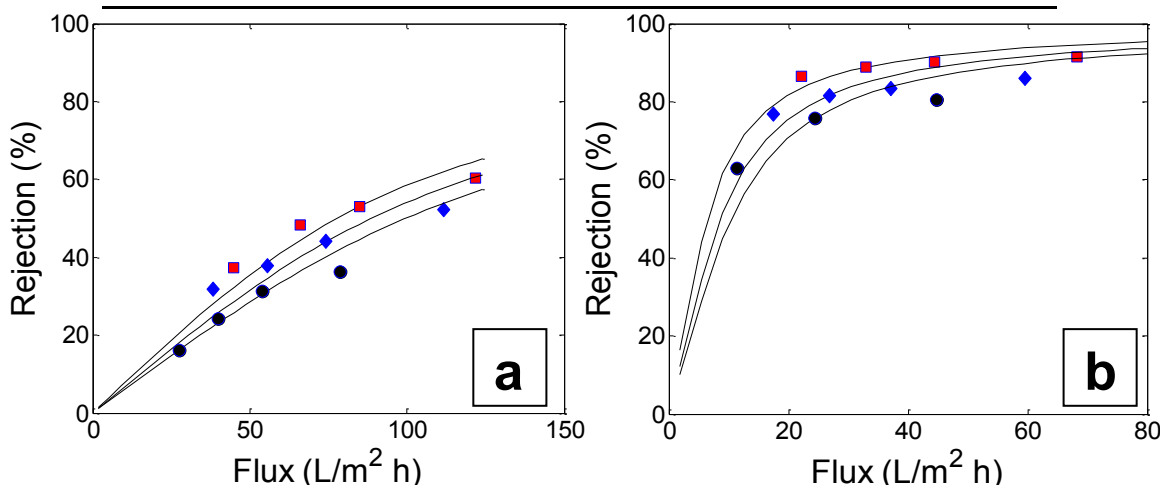


Figure 5.7. Rejection of CaCl₂ as a function of permeate flux for SNF20 module (a) and NF3A module (b) (square: 0.001 M; diamonds: 0.01M; circles: 0.05M). The modification of flux is through the change applied pressure. The line shows fitting with extended Nernst-Planck model.

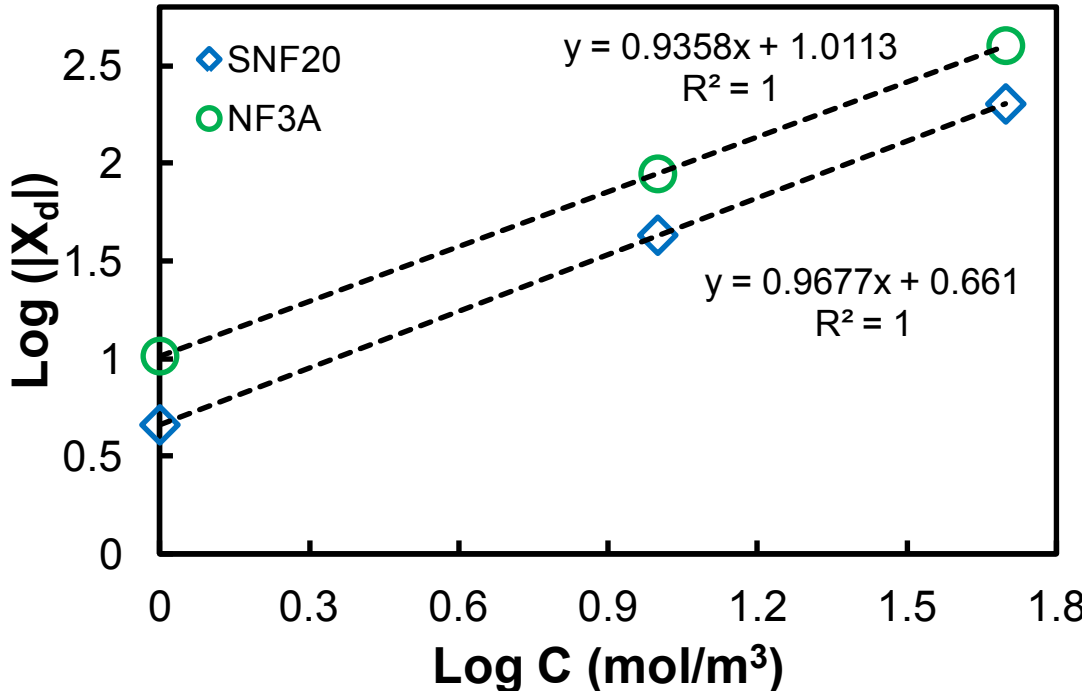


Figure 5.8. Calculated effective charge density (X_d) as a function of different CaCl_2 concentration. Logarithm coordinates are used for better comparison.

The extended Nernst-Planck model was successfully applied to describe the rejection of single solutes. Simulations were also performed in order to investigate the influence of effective charge density. **Figure 5.9** presents the rejection curves with different effective charge density. It indicates that the shape of the rejection curve doesn't change with the modification of effective charge profile. The influence of charge is not obvious with SNF20 membrane because the steric is important especially for the big ions such as Ca^{2+} , because of the small pore diameter. However, for membranes with larger pore size, the charge effect is more dominant. In this cases, the charge distribution along the pore should be taken into account[275].

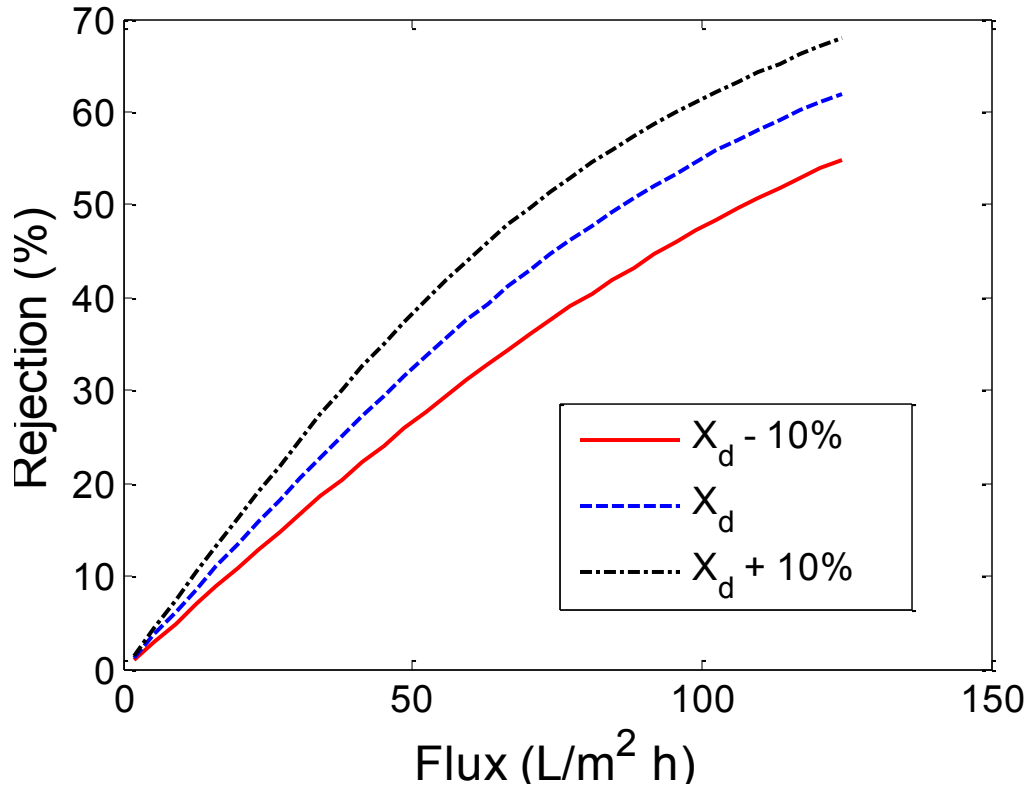


Figure 5.9. Rejection curve of 10 mol/m³ CaCl₂ solution through SNF20 membrane with different effective charge density.

5.3.3 Retention of Combined Sucrose and Salt

To investigate the separation performance of mixture, filtration experiments with mixture of CaCl₂ and sucrose with the increase of concentration of either CaCl₂ or sucrose. To study the effect of CaCl₂ concentration on the sucrose rejection, the CaCl₂ concentration was used to be 2 g/L and 4 g/L with constant sucrose concentration at 10 g/L and the result is shown in Figure 5.10. By the increase of CaCl₂ concentration, there is no obvious change of sucrose rejection as shown in Figure 5.10(a). This may due to the less pore swelling caused by the high concentration of counter ions in the electrical double-layer at the pore surface[238]. As comparison, the rejection of sucrose and CaCl₂ mixture

of NF3A is shown in Figure 5.11. It indicates that the rejection of sucrose and CaCl_2 mixture is lower than the individual rejection due to the pore swelling by high effective charge density of NF3A. Therefore, it's preferable to use membrane with low effective charge density at higher salt concentration in order to get enhanced sugar rejection[276]. In addition, the CaCl_2 rejection for SNF20 membrane slightly decreases with the increase of CaCl_2 concentration as shown in Figure 5.10(b). The observed results may because that the electrostatic interactions between the salt and membrane surface has been weakened at higher salt concentration[271, 277, 278].

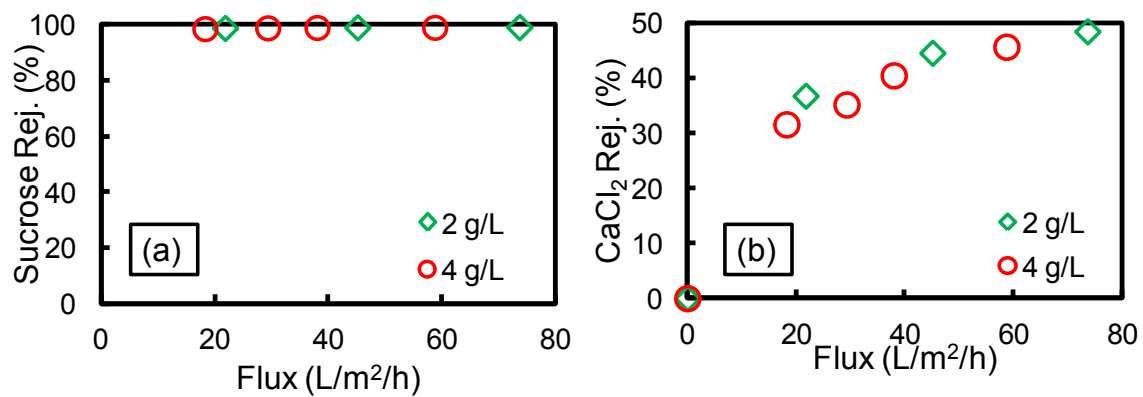


Figure 5.10. Rejection of sucrose (a) and CaCl_2 (b) for SNF20 membrane with different CaCl_2 concentration (2 g/L and 4 g/L) and constant sucrose concentration at 10 g/L. The flux is modified by the change of applied pressure.

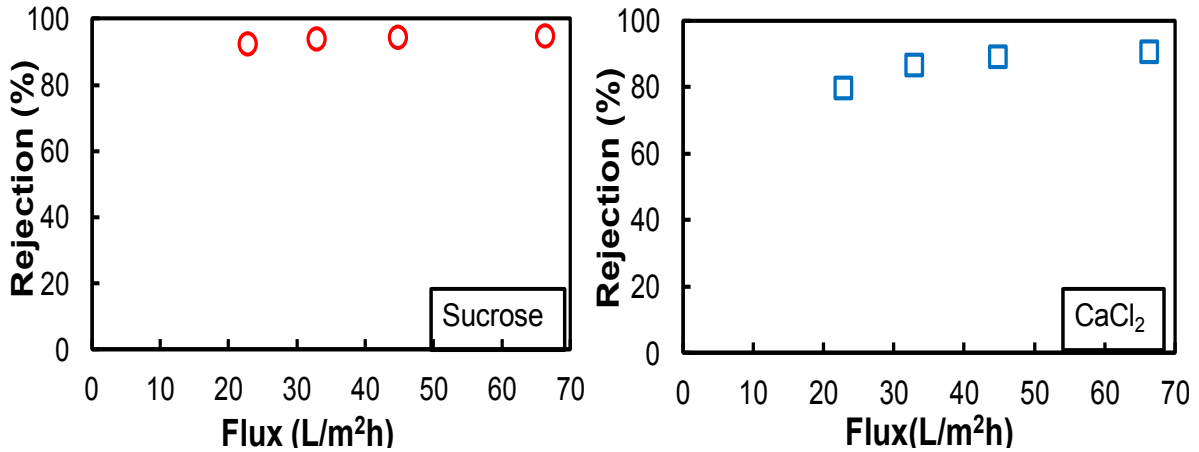


Figure 5.11. Rejection of sucrose and CaCl₂ for NF3A module as a function of permeate flux for feeds containing 2 g/L sucrose and 2 g/L CaCl₂. The flux is modified by the change of applied pressure.

As the increase of sucrose concentration, the rejection of CaCl₂ is slightly decreased as shown in Figure 5.12(a). The reduction of rejection may be ascribed to the hindered back diffusion of charged ions in the concentration polarization layer[261]. As shown in Figure 5.12(b), rejection of sucrose doesn't show any obvious change due to the less pore swelling discussed previously.

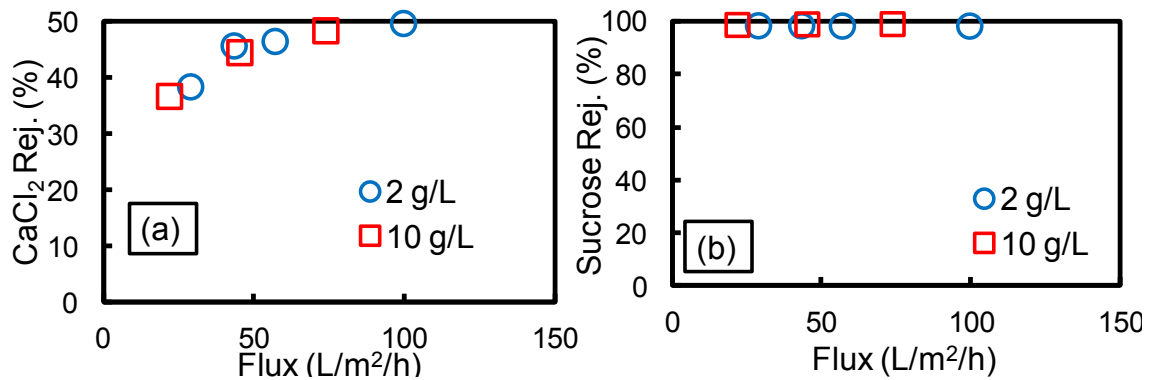


Figure 5.12. Rejection of CaCl₂ (a) and sucrose (b) for SNF20 membrane with different sucrose concentration (2 g/L and 10 g/L) and constant CaCl₂ concentration at 2 g/L. The flux is modified by the change of applied pressure.

5.3.4 Stability

Membrane fouling caused by solute or particles deposited onto membrane surface or into the pores can degrade separation performance[279]. The membrane fouling is a big obstacle for the widespread application of membrane techniques. Thus, to check the long-term stability and the fouling property of SNF20 membrane, the pure water flux tests were performed at 10.4 bar over a period over six months and the result is shown in Figure 5.13. The average water flux keeps constant at about 129.5 L/m²h (at 10.4 bar) over the course of testing. A feed composition of 10 g/L sucrose and 2 g/L CaCl₂ was also tested with the SNF20 membrane module. At an operating pressure of 10.4 bar, the rejection of sucrose in one month period remains almost no change at about 99.5%, while the CaCl₂ rejection is about 43.0%. This indicates the good stability and no fouling of the membrane module.

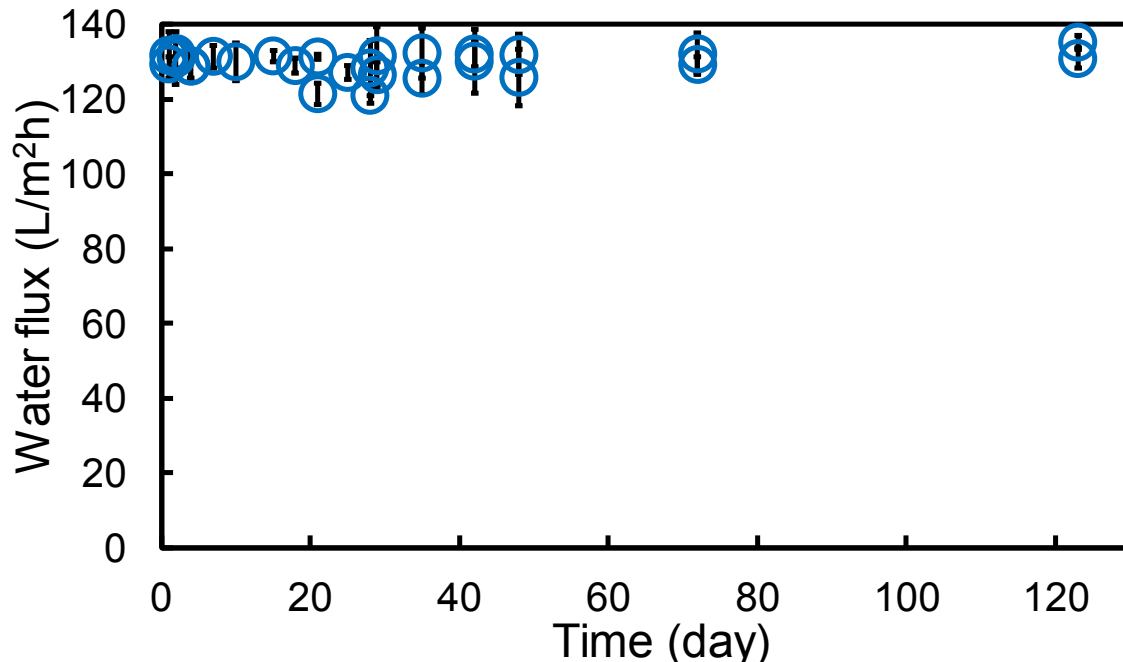


Figure 5.13. The long term stability of SNF20 module over six months' run. (The pure water flux was normalized with viscosity at 25°C; P=10.4 bar. Membrane area: 6.4 ft²).

5.4 Conclusion

In conclusion, SNF20 membranes show promising potential to be used for the separation of sugar in food industry. The SNF20 membrane shows higher water permeability and high rejection of sucrose (over 99%) compared with other reported NF membranes. The higher rejection of sucrose over glucose may have the potential to be used for selective separation of sugar with different degree of polymerization (DP). More importantly, the sucrose rejection is not affected by the salt concentration. This work shows that it's important to consider structural and charge properties of membranes for food industry application. It will be helpful to choose membranes with lower charge density for the selective separation of sucrose with the presence of divalent salts.

5.5 Broad Application Prospect

Traditional nanofiltration membranes have been developed for the application in drinking water production, wastewater treatment as well as a pretreatment of desalination due to their high rejection of divalent ions with higher flux. Current research in membrane science is focusing on the modification of membrane physical and chemical properties. The selective separation is based on the active layer obtained by interfacial polymerization between two highly reactive monomers. The nature of solvents, monomers, monomers concentration and ratio, and reaction time as well affect the structure, surface charge and compositions. For example, the reduction of surface charge via the modification of interfacial polymerization allows the selective separation of lactose and calcium to produce high quality of lactose and eliminate the calcium scaling in evaporator with low energy consumption. The coating with brush-like poly(ethylene glycol) (PEG) on the thin active layer to enhance the antifouling property. Therefore, the optimization of the membrane surface properties will allow the development of membranes with advanced performance.

Chapter 6 - Conclusion

This research advanced the frontiers of membrane science and improved membrane technologies for applications of tunable separation and remediation, especially for the removal of toxic chlorinated organics (trichloroethylene, TCE and polychlorinated biphenyls, PCBs etc). The integration of nanotechnology with temperature responsive membranes provides breakthrough in the area of catalytic membranes. Such integration has a combination of the features of high capacity of contaminants on membrane pore surface, controllable reaction rate, stimuli-responsiveness, and cost-effectiveness. Our work has led to significant improvement of current chlorinated organics degradation and advanced membrane technology.

6.1 Key Advancements to Science and Engineering

The key advancements to science and engineering achieved from this work were concluded as follows.

- Tunable and enhanced separation and reaction of toxic organic compound was achieved through functionalized membrane both pH and temperature responsive polymers.
- Advanced membrane functionalization techniques within microporous media were utilized to develop membrane with enhanced performance including controlled and tunable permeation rate, low energy requirement, good ion-exchange property.
- Mathematical modeling was used to better understand the responsive behavior and ion transport, providing the information necessary for more efficient utilization of functionalized membrane.

- Functionalized membrane was successfully scaled up in commercial scale with consistent performance, stability, and uniformity similar to that obtained in bench scale.

6.2 Specific Accomplishments

The specific accomplishments from this work were concluded as follows.

6.2.1 Stimuli-responsive Materials for Tunable Separation and Reaction

- Temperature responsive P(NIPAAm-AA) hydrogel with ion exchange groups (-COOH) for metal ion capture and subsequent conversion to nanostructured zero-valent metal in the matrix was synthesized.
- The swelling and polymer conformation transition below and above LCST was quantified for temperature responsive P(NIPAAm-AA) hydrogel.
- Peppas-Lucht model was also used to calculate the solvent and polymer interaction parameters to better understand the swelling behavior.
- The dechlorination of trichloroethylene (TCE) and 2,2'-dichlorobiphenyl (DiCB) with Fe/Pd NPs immobilized in temperature responsive P(NIPAAm-AA) hydrogel below and above LCST proved the enhanced reactivity with 3 fold increase for only 4°C temperature change.
- The combination of responsive hydrogel with macroporous membrane polyvinylidene fluoride (PVDF) support was developed to enhance the mechanical strength of membrane.
- Water flux through the temperature responsive membrane varied by up to 15 times for temperature changes from 30°C (below LCST) to 34°C (above LCST).

- Dextran solution was used to evaluate the separation properties using the temperature responsive membrane. The results quantified the rejection dependence on LCST transition.

6.2.2 Membrane Functionalization Techniques

- PVDF membrane was chemically treated with alkaline solution to create partial defluorinated membrane (Def-PVDF) with conjugated double bonds for covalent attachment of functional polymers. The effect of treatment time was also investigated and showed the membrane morphology was changed with longer treatment time as confirmed by SEM.
- Polyacrylic acid (PAA) was proven to be covalently attached to Def-PVDF membrane through the disappearance of double bonds by ATR-FTIR, and the reversible and stable pH responsive behavior of water and solutes.
- The Na_2SO_4 rejection through PAA-Def-PVDF membrane was also investigated to characterize the membrane and shows the rise of rejection with pH increases and reduction with the decrease of applied pressure.
- PAA-Def-PVDF membrane was successfully utilized as a support to immobilize metal nanoparticles to remove toxic chlorinated compounds (such as, TCE, PCB etc).
- Asymmetric membrane with macroporous sponge-like structure was successfully prepared by phase inversion method in both lab-scale and large-scale.
- The spongy PVDF membrane (SPVDF) shows high surface area, high porosity and higher yield of PAA functionalization compared to normal PVDF membrane.
- The PAA functionalized SPVDF membrane indicates very high ion-exchange capacity of Ca^{2+} is 3.2 mg/cm^2 (265 mg/g) with 10 times

higher than normal functionalization based on commercial MF PVDF.

6.2.3 Full-scale Membrane Validation and Evaluation

- The functionalization method and process were validated by scaling up through the evaluation of full-scale functionalized membrane.
- Selective permeation of CaCl_2 and high sucrose rejection was obtained through the evaluation of nanofiltration membranes with lower charge (SNF20) in comparison to the conventional negatively-charged commercial nanofiltration membrane (NF3A).
- The higher rejection of sucrose over glucose through SNF20 membrane have the potential application for selective separation of sugar with different degree of polymerization (DP).
- The SNF20 module shows high stability without fouling in a long-term (two months) test.
- Donnan-Steric-Pore-Model (DSPM) and extended Nernst-Planck model were used to evaluate the experimental results and shows the good fitting with single solute rejection.

6.3 Future work

This study has developed a platform for an improved membrane technology with functional moiety applicable for water remediation and tunable separation. Based on the knowledge obtained from current study, further study on the following aspects is recommended to improve the performance of functionalized membranes.

For the realization of the practical application of enhanced degradation of toxic chlorinated organics from groundwater by temperature responsive polymers, the modification of transition solution temperature (LCST) to the groundwater temperature will be necessary. Proposed approaches that could lead to the

targets include:(1) using positive temperature responsive polymer, such as, copolymer of acrylamide and acrylic acid[280], (2) introducing the hydrophobic moiety into the copolymer, such as, tert-butyl methacrylate (tBMA), butyl methacrylate (BMA), etc) as widely reported in the literatures[151, 152]. The proposed approach is supported by our preliminary study which is modified the LCST to 25°C via the incorporation of tBMA with PNIPAAm.

In addition, the *in-situ* synthesis of nanoparticles within the polyacrylic acid (PAA) functionalized membrane can be expanded to other metals (such as, Au, Ni, Pd, Pt and Cu) as long as the ions have interaction with carboxylic acid groups. It should be noted that the ion exchange highly depends on the ionization of carboxylic acid groups which is affected by the solution pH. Therefore the nature of functionalized polymer should be considered in future work. For example, the functionalization with quaternary amine groups are current undergoing work in the lab, which can be applied in a wide pH range from 2 to 12.

Nomenclature

Chapter 2

Q	swelling ratio
W_s	the weight of hydrogel at swelling state (g)
W_d	the weight of hydrogel at dry state (g)
χ_p	the polymer solvent interaction parameter
Φ_P	the polymer repeat unit volume fraction in the swollen state
V_{H_2O}	the water molar volume ($18 \text{ cm}^3\text{mol}^{-1}$)
λ	the number of links of repeating unit
M_r	molecular weight of repeating unit
ν^0	the cross-linking density (mol/cm^3)
W_s	the weights of absorbed solvent
W_p	the weights of dried hydrogel
ρ_p	the density of dried polymer
ρ_s	the density of solvent
k_{SA}	surface area normalized reactivity
k_{obs}	observed reactivity
C	chloro-organics concentration (mg/L)
α_s	specific surface area of the nanoparticles (m^2/g)

ρ_m the nanoparticle loading (g/L)

t reaction time

Chapter 3

J the volume flux (L/m²/h)

N the membrane pore density

A the membrane area

D the pore diameter

η the dynamic viscosity of water

L the membrane thickness

ΔP the transmembrane pressure difference

J_T represents the reported flux at temperature T

η_T the viscosity at temperature T

$\eta_{25^\circ\text{C}}$ the viscosity of water at 25°C

φ the volume fraction of the polymer in the membrane

D_f the pore diameter for blank membrane

D_0 the pore diameter for functionalized membrane

T_c the critical solution temperature for temperature responsive membrane (°C)

ΔT the temperature transition change from open-state to closed-state ($^{\circ}\text{C}$)

Chapter 4

V_m the membrane volume

V_p the volume occupied by PVDF polymer

L the PVDF membrane thickness (cm)

W_m the membrane mass (g)

ρ_p the density of PVDF (1.78 g/cm^3)

Chapter 5

L_P the membrane permeability ($\text{L/m}^2/\text{h}/\text{bar}$)

J_w pure water flux ($\text{L/m}^2/\text{h}$)

j_i the solute flux

$K_{i,d}$ the hindered nature of diffusion

$K_{i,c}$ convection of ions inside the membrane

K^{-1} hydrodynamic coefficient

G the lag coefficient

Φ equilibrium partition coefficient

c_i concentration in the membrane (mol/m^3)

m	the molality of the solution (mol/kg)
n_i	the mole fraction of the solute
$C_{i,m}$	the concentration at membrane surface (mol/m ³)
$C_{i,p}$	the permeate concentration (mol/m ³)
$c_{i,x=0}$	the solute concentration at upper surface ($x = 0$)
$c_{i,x=\Delta x}$	the solute concentration at the lower surface ($x = \Delta x$)
r_s	the stokes radius of ions and solutes (m)
r_p	the effective pore radius (m)
R	solute rejection
Pe_m	Peclet number
$D_{i,\infty}$	bulk diffusivity (m ² /s)
$D_{i,p}$	hindered diffusivity (m ² /s)
R_{lim}	the limiting rejection of solute
A_k	effective porosity of the membrane
T	absolute temperature (K)
F	Faraday constant (C/mol)

X	effective membrane charge(mol/m ³)
V	solute velocity (m/s)
λ	ratio of ionic or solute radius to pore radius
ψ	electric potential in axial direction inside the membrane(V)
z_i	the valence of ion

Name Designation

TCE	trichloroethylene
PCB	polychlorinated biphenyl
BP	biphenyl
DiCB	2,2'-dichlorobiphenyl
ATRP	atom transfer radical polymerization
RAFT	reversible free radical-fragmentation chain transfer
PVDF	poly(vinylidene fluoride)
PS	polysulfone
PES	polyether sulfone
DMA	dimethylacetamide
DMF	N,N-dimethylformamide

NMP	N-methylpyrrolidone
DMSO	dimethylsulfoxide
LCST	lower critical solution temperature
UCST	upper critical solution temperature
PP	polypropylene
NIPAAm	N-isopropylacrylamide
AA	acrylic acid
PEG600DMA	poly(ethylene glycol) 600 dimethacrylate
DMPA	4-(4-dimethylaminophenylazo) aniline
PDMS	polydimethylsiloxane
PE	polyethylene
PET	poly(ethylene terephthalate)
PC	polycarbonate
Bis	N, N'-methylenebisacrylamide
TEMED	N,N,N',N'-tetramethylethylenediamine
APS	ammonium persulfate
RMS	root mean squared

PVP	polyvinylpyrrolidone
Def-PVDF	dehydrofluorinated poly(vinylidene fluoride)
SPVDF	spongy poly(vinylidene fluoride)
PIP	piperazine
TMC	trimesoyl chloride
MF	microfiltration
UF	ultrafiltration
NF	nanofiltration
RO	reverse osmosis
ATR-FTIR	Attenuated total reflectance-Fourier transform infrared spectroscopy
SEM	scanning electron microscopy
TEM	transmission electron microscopy
BET	Brunauer–Emmett–Teller
GC-MS	gas chromatograph-mass spectrometer
TGA	thermogravimetric analysis
DSC	differential scanning calorimetry
AFM	atomic force microscopy

XPS	X-ray photoelectron spectroscopy
TOC	total organic carbon
GPC	gel permeation chromatography

Appendix

Determination of effective charge density of nanofiltration membranes based on experimental data via extended Nernst-Planck Equation (Chapter 5).

1. Step-by-Step Development of the Proposed Model

Step 1: Experimentally measure the water permeate flux (J_w) at various applied pressure for both SNF20 and NF3A membranes.

Step 2: Calculate water permeability (L_p)

$$L_p = \frac{J_w}{\Delta P}$$

Step 3: Experimentally measure sucrose and glucose rejection as a function of pressure.

Step 4: Assuming the membrane are homogenous and the pore is cylindrical, the separation performance can be described by extended Nernst-Planck model.

$$j_i = -D_{i,p} \frac{dc_i}{dx} + K_{i,c} c_i V$$

$$j_i = J_v C_{i,p}$$

$$D_{i,p} = K_{i,d} D_{i,\infty}$$

Assuming the membrane pore is uniformly distributed,

$$K_{i,c} = (2 - \Phi)(1.0 + 0.054\lambda - 0.988\lambda^2 + 0.441\lambda^3)$$

$$K_{i,d} = 1.0 - 2.30\lambda + 1.154\lambda^2 + 0.224\lambda^3$$

$$\Phi = \frac{c_{i,x=0}}{C_{i,m}} = \frac{c_{i,x=\Delta x}}{C_{i,p}} = \left(1 - \frac{r_s}{r_p}\right)^2 = (1 - \lambda)^2$$

Integrate the extended Nernst Planck equation from the upper surface ($x = 0$) to ($x = \Delta x$) in terms of $C_{i,m}$ and $C_{i,p}$ to obtain the following expression for rejection:

$$R = 1 - \frac{K_{i,c} \Phi}{1 - \exp(-Pe_m)(1 - \Phi K_{i,c})}$$

$$Pe_m = \frac{K_{i,c}}{K_{i,d}} \frac{V \Delta x}{D_{i,\infty} A_k}$$

$$D_{i,\infty} = \frac{kT}{6\pi\eta r_s}$$

When Pe_m is close to limit,

$$R_{\text{lim}} = 1 - \Phi K_{i,c}$$

Step 5: Calculate membrane pore size(r_p) and the ratio of effective thickness to porosity($\Delta x / A_k$) by fitting the experiment rejection data.

$$J_w = \frac{r_p^2 (\Delta P - \Delta \pi)}{8\mu (\Delta x / A_k)}$$

$$\Delta \pi = \sum C_{i,m} RT$$

Step 6: Experimentally measure the CaCl_2 rejection, feed, permeate concentration. For charged solute, electrical field is added into the extended Nernst Planck equation.

$$j_i = -D_{i,p} \frac{dc_i}{dx} - \frac{z_i c_i D_{i,p}}{RT} F \frac{d\Psi}{dx} + K_{i,c} c_i V$$

Rewrite to obtain,

$$\frac{dc_i}{dx} = \frac{J_v}{K_{i,d} D_{i,\infty}} (K_{i,c} c_i - C_{i,p}) - \frac{z_i c_i F}{RT} \frac{d\Psi}{dx}$$

The potential gradient term can be expressed as following, using CaCl_2 in this work,

$$\frac{d\Psi}{dx} = \frac{\frac{z_{\text{Ca}^{2+}} J_v}{K_{i,d} D_{\text{Ca}^{2+},\infty}} (K_{\text{Ca}^{2+},c} c_{\text{Ca}^{2+}} - C_{\text{Ca}^{2+},p}) + \frac{z_{\text{Cl}^-} J_v}{K_{i,d} D_{\text{Cl}^-,\infty}} (K_{\text{Cl}^-,c} c_{\text{Cl}^-} - C_{\text{Cl}^-,p})}{\frac{F}{RT} (z_{\text{Ca}^{2+}}^2 c_{\text{Ca}^{2+}} + z_{\text{Cl}^-}^2 c_{\text{Cl}^-})}$$

Step 7: Use the Matlab program to solve this ordinary differential equations. The boundary conditions used to solve this system were:

$$x = 0 \quad C_i = C_{i,m}; \quad x = \Delta x \quad C_i = C_{i,p}$$

Using the equilibrium conditions to obtain the ion concentration inside the membrane, which take the Donnan and steric effects into account:

$$\frac{\gamma_i c_i}{\gamma_i^0 C_i^0} = \Phi \exp\left(-\frac{z_i F}{RT} \Delta\psi_D\right)$$

The Matlab program utilize the command `bvp4c` to solve two point boundary value problems for ODE's by collocation.

Step 8: Use conditions of electroneutrality in the bulk and inside the membrane to solve for the effective charge density X_d .

For CaCl_2 ,

$$z_{\text{Ca}^{2+}} C_{\text{Ca}^{2+}}^0 + z_{\text{Cl}^-} C_{\text{Cl}^-}^0 = 0$$

$$z_{\text{Ca}^{2+}} c_{\text{Ca}^{2+}} + z_{\text{Cl}^-} c_{\text{Cl}^-} = -X_d$$

Step 9: Use the experimentally determined relationship between CaCl_2 rejection and flux to evaluate the most accurate estimation of the effective charge density X_d . Adjust $C_{i,p}$ until the experimental trend is best fitted with the model predictions.

2. Determination of effective charge density based on the data fitting with experimentally CaCl_2 rejection data

Matlab Program:

```
function MembraneModel

% Written by Li Xiao
% Revision Date: Jun 10 2014
% Revision Comment:
% Correlation package for modeling of membrane separation using a global
% minimum search

% This code is to correlate experimental data with the model.

clear all
clc

global Jvexp Cpexp Cbexp rp deltax

[file,dir] = uigetfile('*.xls');
data = xlsread(fullfile(dir,file));
Jvexp = data(:,1); %Flux in m3/m2/s
```



```

Cbexp = data(:,2)*[1 2];
Cpexp = data(:,3); %Permeat Concentration in mol/m3

rp = 5.15E-10; %m
deltax = 9.12e-7; %m

Xd0 = -1000;
Xd1b = -3500;
Xdub = 0;

options = psoptimset('PlotFcns',{@psplotbestf,@psplotmeshsize,@psplotbestx},...
                    'Display','iter','TimeLimit',8*3600);
Xd = patternsearch(@Opt,Xd0,[],[],[],[],Xd1b,Xdub,[],options);
Xd

for i = 1:length(Jvexp)
    Cp(i) = PermeatConc(Xd,Jvexp(i),Cbexp(i,:)',rp);
end

Jvdis = 5e-7:1e-6:3.5e-5;
for i = 1:length(Jvdis)
    Cpdis(i) = PermeatConc(Xd,Jvdis(i),Cbexp(1,:)',rp);
end
figure(2)
plot(Jvdis*3.6e6,(1-
Cpdis./Cbexp(1,1))*100,'MarkerSize',10,'Marker','none','LineStyle','-');hold on
plot(Jvexp*3.6e6,(1-
Cpexp./Cbexp(:,1))*100,'MarkerSize',10,'Marker','square','LineStyle','none',...
'MarkerFaceColor',[1 0 0]);hold off
xlabel('Flux (L/m^2 h)');
ylabel('Rejection (%)');
legend('Regression','Experiment')

function obj = Opt(Xd)

global Jvexp Cpexp rp Cbexp

for i = 1:length(Jvexp)
    obj(i) = abs(PermeatConc(Xd,Jvexp(i),Cbexp(i,:)',rp) - Cpexp(i))/Cpexp(i);
end
obj = sum(obj);

function C = PermeatConc(Xdin, Jvin,C0in, rpin)

global Cp Jv deltax Kc Xd C0 rp
Xd = Xdin;
C0 = C0in;
Jv = Jvin;
Cp = C0(1);
rp = rpin;

ri = [1.94E-10; 0.79E-10]; %m

```

```

theta = (1-ri./rp).^2;
Kc =(2-theta).*(1+0.054*ri./rp-0.988*(ri./rp).^2+0.441*(ri./rp).^3);

solinit = bvpinit(linspace(0,deltax,30),@npinit,Cp);
sol = bvp4c(@f,@npb,solinit);
C = sol.parameters;

function dcdx = f(x,c,Cp)      % Define simultaneous ODE equations
global Jv Kc

Dp = [0.78e-9;2.03e-9];
z = [2;-1];
dcdx = Jv./Dp.*(Kc.*c-[Cp;-Cp*z(1)/z(2)])-z.*c.*sum(Jv.*z./Dp.*(Kc.*c-[Cp;-
Cp*z(1)/z(2)]))/(sum(z.^2.*c));

function bd = npb(ca,cb,Cp)
global xd C0 rp
T = 298;
z = [2;-1];
ri = [1.94E-10; 0.79E-10]; %m

theta = (1-ri./rp).^2;
F = 96487; %Faraday constant, 96487 C mol-1
R = 8.314; %Gas constant
phiD0 = 0.1;
options = psoptimset('Display','off');
phiDa = fsolve(@(phiDa)abs(sum(z.*C0.*theta.*exp(-F.*z./R/T*phiDa)) - xd),phiD0,options);
c0_m = C0.*theta.*exp(-F.*z./R/T*phiDa);
phiDb = fsolve(@(phiDb)abs(sum(z.*[Cp;-Cp*z(1)/z(2)].*theta.*exp(-F.*z./R/T*phiDb)) -
xd),phiD0,options);
cp_m = Cp.*theta.*exp(-F.*z./R/T*phiDb);
bd = [ca(1)-c0_m(1);cb(1)-cp_m(1);ca(1)-ca(2)-xd];

function cinit = npinit(x)
global C0 Cp deltax xd rp
T = 298;
z = [2;-1];
ri = [1.94E-10; 0.79E-10]; %m

theta = (1-ri./rp).^2;
F = 96487; %Faraday constant, 96487 C mol-1
R = 8.314; %Gas constant
phiD0 = 0.1;
options = psoptimset('Display','off');
phiDa = fsolve(@(phiDa)abs(sum(z.*C0.*theta.*exp(-F.*z./R/T*phiDa)) - xd),phiD0,options);
c0 = C0.*theta.*exp(-F.*z./R/T*phiDa);
phiDb = fsolve(@(phiDa)abs(sum(z.*[Cp;-Cp*z(1)/z(2)].*theta.*exp(-F.*z./R/T*phiDa)) -
xd),phiD0,options);
cp = Cp.*theta.*exp(-F.*z./R/T*phiDb);
cinit = c0 - (c0-cp).*x./deltax;

```

References

- [1] W.-L. Huang, E.W. Welch, E.A. Corley, Public sector voluntary initiatives: the adoption of the environmental management system by public waste water treatment facilities in the United States, *Journal of Environmental Planning and Management*, (2013) 1-21.
- [2] S.L. Postel, For Our Thirsty World, Efficiency or Else, *Science*, 313 (2006) 1046-1047.
- [3] A. Bhatnagar, W. Hogland, M. Marques, M. Sillanpää, An overview of the modification methods of activated carbon for its water treatment applications, *Chem. Eng. J.*, 219 (2013) 499-511.
- [4] M. Lu, M. Duke, D. Zhao, R. Semiat, *Functional Nanostructured Materials and Membranes for Water Treatment*, John Wiley & Sons, 2013.
- [5] I. Rusyn, W.A. Chiu, L.H. Lash, H. Kromhout, J. Hansen, K.Z. Guyton, Trichloroethylene: Mechanistic, epidemiologic and other supporting evidence of carcinogenic hazard, *Pharmacol. Ther.*, 141 (2014) 55-68.
- [6] B. Lauby-Secretan, D. Loomis, Y. Grosse, F. El Ghissassi, V. Bouvard, L. Benbrahim-Tallaa, N. Guha, R. Baan, H. Mattock, K. Straif, Carcinogenicity of polychlorinated biphenyls and polybrominated biphenyls, *The lancet oncology*, 14 (2013) 287.
- [7] R. Gioia, A.J. Akindele, S.A. Adebusoye, K.A. Asante, S. Tanabe, A. Buekens, A.J. Sasco, Polychlorinated biphenyls (PCBs) in Africa: a review of environmental levels, *Environmental Science and Pollution Research*, (2013) 1-12.

- [8] J. Xu, D. Bhattacharyya, Membrane-based bimetallic nanoparticles for environmental remediation: Synthesis and reactive properties, *Environ. Prog.*, 24 (2005) 358-366.
- [9] D. Bhattacharyya, J. Xu, L. Bachas, D. Meyer, Y. Tee, Bimetallic nanoparticles: Membrane-based synthesis for applications to PCB and TCE dechlorination., *Abstracts of Papers of the American Chemical Society*, 229 (2005) U936-U936.
- [10] Y.-H. Tee, L. Bachas, D. Bhattacharyya, Degradation of Trichloroethylene by Iron-Based Bimetallic Nanoparticles, *The Journal of Physical Chemistry C*, 113 (2009) 9454-9464.
- [11] D. Bhattacharyya, Functionalized membranes and environmental applications, *Clean Techn Environ Policy*, 9 (2007) 81-83.
- [12] D.E. Meyer, M. Williams, D. Bhattacharyya, Reverse Osmosis, in: *Kirk-Othmer Encyclopedia of Chemical Technology*, John Wiley & Sons, Inc., 2000.
- [13] R. Patil, *Membrane Processes for Sustainable Energy Applications*, THE UNIVERSITY OF TOLEDO, 2013.
- [14] H. WANG, Y.-f. LIU, D.-m. PENG, F.-d. WANG, M.-x. LU, The development of membrane separation technology and its application prospect, *Applied Chemical Industry*, 3 (2013) 036.
- [15] A.M. Hollman, N.T. Scherrer, A. Cammers-Goodwin, D. Bhattacharyya, Separation of dilute electrolytes in poly(amino acid) functionalized microporous membranes: model evaluation and experimental results, *J. Membr. Sci.*, 239 (2004) 65-79.

- [16] S.R. Lewis, V. Smuleac, L. Xiao, D. Bhattacharyya, Tunable Separations, Reactions, and Nanoparticle Synthesis in Functionalized Membranes, in: Responsive Membranes and Materials, John Wiley & Sons, Ltd., 2012, pp. 97-142.
- [17] H. Yin, J. Wang, Z. Xie, J. Yang, J. Bai, J. Lu, Y. Zhang, D. Yin, J.Y.S. Lin, A highly permeable and selective amino-functionalized MOF CAU-1 membrane for CO₂-N₂ separation, Chem. Commun., 50 (2014) 3699-3701.
- [18] A.R. Ladhe, P. Frailie, D. Hua, M. Darsillo, D. Bhattacharyya, Thiol Functionalized Silica-Mixed Matrix Membranes for Silver Capture from Aqueous Solutions: Experimental Results and Modeling, J. Membr. Sci., 326 (2009) 460-471.
- [19] K. Bang Mo, Membrane-based solvent extraction for selective removal and recovery of metals, J. Membr. Sci., 21 (1984) 5-19.
- [20] Functionalization Methods for Membrane Surfaces, in: Surface Engineering of Polymer Membranes, Springer Berlin Heidelberg, 2009, pp. 64-79.
- [21] E. Sackmann, Supported Membranes: Scientific and Practical Applications, Science, 271 (1996) 43-48.
- [22] B. Oleksandr, K. Viktor, T. Tacibaht, G. Yasser, L. Igor, Polymeric Membranes: Surface Modification by "Grafting to" Method and Fabrication of Multilayered Assemblies, in: Nanoscience and Nanotechnology for Chemical and Biological Defense, American Chemical Society, 2009, pp. 289-305.

- [23] A. Bottino, G. Capannelli, O. Monticelli, P. Piaggio, Poly(vinylidene fluoride) with improved functionalization for membrane production, *J. Membr. Sci.*, 166 (2000) 23-29.
- [24] M. Jaroslav, Coatings and surface modification technologies: a finite element bibliography (1995–2005), *Modell. Simul. Mater. Sci. Eng.*, 13 (2005) 935.
- [25] A. Bhattacharya, B.N. Misra, Grafting: a versatile means to modify polymers: Techniques, factors and applications, *Prog. Polym. Sci.*, 29 (2004) 767-814.
- [26] Z. Xu, L. Wan, X. Huang, Functionalization Methods for Membrane Surfaces, *Surface Engineering of Polymer Membranes*, (2009) 64-79.
- [27] Y. Lvov, G. Decher, H. Moehwald, Assembly, structural characterization, and thermal behavior of layer-by-layer deposited ultrathin films of poly(vinyl sulfite) and poly(allylamine), *Langmuir*, 9 (1993) 481-486.
- [28] Y. Wang, A.S. Angelatos, F. Caruso, Template Synthesis of Nanostructured Materials via Layer-by-Layer Assembly†, *Chem. Mater.*, 20 (2007) 848-858.
- [29] N.A. Kotov, Layer-by-layer self-assembly: The contribution of hydrophobic interactions, *Nanostruct. Mater.*, 12 (1999) 789-796.
- [30] A. Bhattacharya, B. Misra, Grafting: a versatile means to modify polymers: techniques, factors and applications, *Prog. Polym. Sci.*, 29 (2004) 767-814.
- [31] C. Oehr, M. Müller, B. Elkin, D. Hegemann, U. Vohrer, Plasma grafting — a method to obtain monofunctional surfaces, *Surf. Coat. Technol.*, 116–119 (1999) 25-35.

- [32] V. Sciaratta, U. Vohrer, D. Hegemann, M. Müller, C. Oehr, Plasma functionalization of polypropylene with acrylic acid, *Surf. Coat. Technol.*, 174–175 (2003) 805-810.
- [33] J. Hautojärvi, K. Kontturi, J.H. Näsman, B.L. Svarfvar, P. Viinikka, M. Vuoristo, Characterization of graft-modified porous polymer membranes, *Industrial & engineering chemistry research*, 35 (1996) 450-457.
- [34] J. Elisseeff, Hydrogels: Structure starts to gel, *Nat Mater*, 7 (2008) 271-273.
- [35] E.M. Gabriel, G.E. Gillberg, In situ modification of microporous membranes, *J. Appl. Polym. Sci.*, 48 (1993) 2081-2090.
- [36] T.-H. Young, L.-W. Chen, Pore formation mechanism of membranes from phase inversion process, *Desalination*, 103 (1995) 233-247.
- [37] H. Strathmann, K. Kock, The formation mechanism of phase inversion membranes, *Desalination*, 21 (1977) 241-255.
- [38] M.A.C. Stuart, W.T.S. Huck, J. Genzer, M. Muller, C. Ober, M. Stamm, G.B. Sukhorukov, I. Szleifer, V.V. Tsukruk, M. Urban, F. Winnik, S. Zauscher, I. Luzinov, S. Minko, Emerging applications of stimuli-responsive polymer materials, *Nat Mater*, 9 (2010) 101-113.
- [39] F. Reyes-Ortega, 3 - pH-responsive polymers: properties, synthesis and applications, in: M.R. Aguilar, J.S. Román (Eds.) *Smart Polymers and their Applications*, Woodhead Publishing, 2014, pp. 45-92.
- [40] A.M. Mika, R.F. Childs, J.M. Dickson, B.E. McCarry, D.R. Gagnon, A new class of polyelectrolyte-filled microfiltration membranes with environmentally controlled porosity, *J. Membr. Sci.*, 108 (1995) 37-56.

- [41] S. Åkerman, K. Åkerman, J. Karppi, P. Koivu, A. Sundell, P. Paronen, K. Järvinen, Adsorption of drugs onto a poly(acrylic acid) grafted cation-exchange membrane, *Eur. J. Pharm. Sci.*, 9 (1999) 137-143.
- [42] D. Wandera, S.R. Wickramasinghe, S.M. Husson, Stimuli-responsive membranes, *J. Membr. Sci.*, 357 (2010) 6-35.
- [43] T. Chen, R. Ferris, J. Zhang, R. Ducker, S. Zauscher, Stimulus-responsive polymer brushes on surfaces: Transduction mechanisms and applications, *Prog. Polym. Sci.*, 35 94-112.
- [44] A. Chan, R.P. Orme, R.A. Fricker, P. Roach, Remote and local control of stimuli responsive materials for therapeutic applications, *Adv. Drug Del. Rev.*, 65 (2013) 497-514.
- [45] B. Keszler, J.P. Kennedy, Amphiphilic networks. VII. Synthesis and characterization of pH-sensitive poly(sulfoethyl methacrylate)-1-polyisobutylene networks, *J. Polym. Sci., Part A: Polym. Chem.*, 32 (1994) 3153-3160.
- [46] Y.-H. Chen, Y.-C. Chung, I.J. Wang, T.-H. Young, Control of cell attachment on pH-responsive chitosan surface by precise adjustment of medium pH, *Biomaterials*, 33 (2012) 1336-1342.
- [47] J. Hu, S. Liu, Responsive Polymers for Detection and Sensing Applications: Current Status and Future Developments, *Macromolecules*, 43 (2010) 8315-8330.
- [48] D. Li, Q. He, Y. Cui, J. Li, Fabrication of pH-Responsive Nanocomposites of Gold Nanoparticles/Poly(4-vinylpyridine), *Chem. Mater.*, 19 (2007) 412-417.

- [49] O.J. Cayre, N. Chagneux, S. Biggs, Stimulus responsive core-shell nanoparticles: synthesis and applications of polymer based aqueous systems, *Soft Matter*, 7 (2011) 2211-2234.
- [50] S. Åkerman, P. Viinikka, B. Svarfvar, K. Putkonen, K. Järvinen, K. Kontturi, J. Näsman, A. Urtti, P. Paronen, Drug permeation through a temperature-sensitive poly(N- isopropylacrylamide) grafted poly(vinylidene fluoride) membrane, *Int. J. Pharm.*, 164 (1998) 29-36.
- [51] Y.-J. Choi, T. Yamaguchi, S.-i. Nakao, A Novel Separation System Using Porous Thermosensitive Membranes, *Industrial & Engineering Chemistry Research*, 39 (2000) 2491-2495.
- [52] F.P. Nicoletta, D. Cupelli, P. Formoso, G. De Filpo, V. Colella, A. Gugliuzza, Light responsive polymer membranes: a review, *Membranes*, 2 (2012) 134-197.
- [53] F. Ercole, T.P. Davis, R.A. Evans, Photo-responsive systems and biomaterials: photochromic polymers, light-triggered self-assembly, surface modification, fluorescence modulation and beyond, *Polymer Chemistry*, 1 (2010) 37-54.
- [54] L. Chen, W. Wang, B. Su, Y. Wen, C. Li, Y. Zhou, M. Li, X. Shi, H. Du, Y. Song, L. Jiang, A Light-Responsive Release Platform by Controlling the Wetting Behavior of Hydrophobic Surface, *ACS Nano*, 8 (2014) 744-751.
- [55] T. Shiga, Deformation and viscoelastic behavior of polymer gels in electric fields, in: *Neutron Spin Echo Spectroscopy Viscoelasticity Rheology*, Springer, 1997, pp. 131-163.

- [56] R. Tomer, D. Dimitrijevic, A.T. Florence, Electrically controlled release of macromolecules from cross-linked hyaluronic acid hydrogels, *J. Controlled Release*, 33 (1995) 405-413.
- [57] Q. Wu, L. Wang, H. Yu, J. Wang, Z. Chen, Organization of Glucose-Responsive Systems and Their Properties, *Chem. Rev.*, 111 (2011) 7855-7875.
- [58] A. Matsumoto, R. Yoshida, K. Kataoka, Glucose-Responsive Polymer Gel Bearing Phenylborate Derivative as a Glucose-Sensing Moiety Operating at the Physiological pH, *Biomacromolecules*, 5 (2004) 1038-1045.
- [59] S. Kitano, Y. Koyama, K. Kataoka, T. Okano, Y. Sakurai, A novel drug delivery system utilizing a glucose responsive polymer complex between poly (vinyl alcohol) and poly (N-vinyl-2-pyrrolidone) with a phenylboronic acid moiety, *J. Controlled Release*, 19 (1992) 161-170.
- [60] J. Kost, T.A. Horbett, B.D. Ratner, M. Singh, Glucose-sensitive membranes containing glucose oxidase: Activity, swelling, and permeability studies, *J. Biomed. Mater. Res.*, 19 (1985) 1117-1133.
- [61] Y. Liu, G.V. Lowry, Effect of Particle Age (Fe⁰ Content) and Solution pH On NZVI Reactivity: H₂ Evolution and TCE Dechlorination, *Environ. Sci. Technol.*, 40 (2006) 6085-6090.
- [62] J.M. Thompson, B.J. Chisholm, A.N. Bezbaruah, Reductive dechlorination of chloroacetanilide herbicide (alachlor) using zero-valent iron nanoparticles, *Environmental Engineering Science*, 27 (2010) 227-232.

- [63] F. Fu, D.D. Dionysiou, H. Liu, The use of zero-valent iron for groundwater remediation and wastewater treatment: A review, *J. Hazard. Mater.*, 267 (2014) 194-205.
- [64] C. Noubactep, Metallic iron for water treatment: A critical review, *CLEAN–Soil, Air, Water*, 41 (2013) 702-710.
- [65] C.L. Chun, D.R. Baer, D.W. Matson, J.E. Amonette, R.L. Penn, Characterization and Reactivity of Iron Nanoparticles prepared with added Cu, Pd, and Ni, *Environ. Sci. Technol.*, 44 (2010) 5079-5085.
- [66] Z.H. Zheng, S.H. Yuan, Y. Liu, X.H. Lu, J.Z. Wan, X.H. Wu, J. Chen, Reductive dechlorination of hexachlorobenzene by Cu/Fe bimetal in the presence of nonionic surfactant, *J. Hazard. Mater.*, 170 (2009) 895-901.
- [67] Y. Xie, Z. Fang, X. Qiu, E.P. Tsang, B. Liang, Comparisons of the reactivity, reusability and stability of four different zero-valent iron-based nanoparticles, *Chemosphere*, 108 (2014) 433-436.
- [68] V. Nagpal, A.D. Bokare, R.C. Chikate, C.V. Rode, K.M. Paknikar, Reductive dechlorination of gamma-hexachlorocyclohexane using Fe-Pd bimetallic nanoparticles, *J. Hazard. Mater.*, 175 (2010) 680-687.
- [69] K. Murugesan, V. Bokare, J.-R. Jeon, E.-J. Kim, J.-H. Kim, Y.-S. Chang, Effect of Fe–Pd bimetallic nanoparticles on *Sphingomonas* sp. PH-07 and a nano-bio hybrid process for triclosan degradation, *Bioresour. Technol.*, 102 (2011) 6019-6025.

- [70] Y.H. Tee, L. Bachas, D. Bhattacharyya, Degradation of Trichloroethylene and Dichlorobiphenyls by Iron-Based Bimetallic Nanoparticles, *J. Phys. Chem. C*, 113 (2009) 9454-9464.
- [71] X. Chen, X. Yao, C. Yu, X. Su, C. Shen, C. Chen, R. Huang, X. Xu, Hydrodechlorination of polychlorinated biphenyls in contaminated soil from an e-waste recycling area, using nanoscale zerovalent iron and Pd/Fe bimetallic nanoparticles, *Environmental Science and Pollution Research*, 21 (2014) 5201-5210.
- [72] H.-L. Lien, W.-X. Zhang, Nanoscale Pd/Fe bimetallic particles: catalytic effects of palladium on hydrodechlorination, *Appl. Catal., B*, 77 (2007) 110-116.
- [73] W.-x. Zhang, Nanoscale Iron Particles for Environmental Remediation: An Overview, *J. Nanopart. Res.*, 5 (2003) 323-332.
- [74] A.-H. Lu, E.L. Salabas, F. Schüth, Magnetic Nanoparticles: Synthesis, Protection, Functionalization, and Application, *Angew. Chem. Int. Ed.*, 46 (2007) 1222-1244.
- [75] F. He, D. Zhao, Hydrodechlorination of trichloroethene using stabilized Fe-Pd nanoparticles: Reaction mechanism and effects of stabilizers, catalysts and reaction conditions, *Appl. Catal., B*, 84 (2008) 533-540.
- [76] Y. Leng, K. Sato, J.-G. Li, T. Ishigaki, M. Iijima, H. Kamiya, T. Yoshida, Iron nanoparticles dispersible in both ethanol and water for direct silica coating, *Powder Technol.*, 196 (2009) 80-84.
- [77] Y.-T. Wei, S.-c. Wu, S.-W. Yang, C.-H. Che, H.-L. Lien, D.-H. Huang, Biodegradable surfactant stabilized nanoscale zero-valent iron for in situ

treatment of vinyl chloride and 1, 2-dichloroethane, *J. Hazard. Mater.*, 211 (2012) 373-380.

[78] H. Kim, H.-J. Hong, Y.-J. Lee, H.-J. Shin, J.-W. Yang, Degradation of trichloroethylene by zero-valent iron immobilized in cationic exchange membrane, *Desalination*, 223 (2008) 212-220.

[79] X. Wang, C. Chen, H. Liu, J. Ma, Preparation and characterization of PAA/PVDF membrane-immobilized Pd/Fe nanoparticles for dechlorination of trichloroacetic acid, *Water Res.*, 42 (2008) 4656-4664.

[80] L. Wu, S. Ritchie, Enhanced dechlorination of trichloroethylene by membrane - supported Pd - coated iron nanoparticles, *Environ. Prog.*, 27 (2008) 218-224.

[81] M. Ballauff, Y. Lu, "Smart" nanoparticles: preparation, characterization and applications, *Polymer*, 48 (2007) 1815-1823.

[82] J.M.K. Timmer, Properties of nanofiltration membranes: model development and industrial application, Technische Universiteit Eindhoven Eindhoven, 2001.

[83] C.K. Diawara, Nanofiltration Process Efficiency in Water Desalination, *Separation & Purification Reviews*, 37 (2008) 302-324.

[84] P. Veerababu, B.B. Vyas, P.S. Singh, P. Ray, Limiting thickness of polyamide-polysulfone thin-film-composite nanofiltration membrane, *Desalination*, 346 (2014) 19-29.

[85] J. Lai, R. Fang, L.-Q. Wang, K. Tu, C. Zhao, X. Qian, S. Zhan, Enzyme-based hydrogels containing dextran as drug delivery carriers: Preparation, characterization, and protein release, *J. Appl. Polym. Sci.*, 113 (2009) 3944-3953.

- [86] M. Yoshida, J. Lahann, Smart Nanomaterials, ACS Nano, 2 (2008) 1101-1107.
- [87] R. Wang, K. Hashimoto, A. Fujishima, M. Chikuni, E. Kojima, A. Kitamura, M. Shimohigoshi, T. Watanabe, Light-induced amphiphilic surfaces, Nature, 388 (1997) 431-432.
- [88] R. Hoogenboom, 2 - Temperature-responsive polymers: properties, synthesis and applications, in: M.R. Aguilar, J.S. Román (Eds.) Smart Polymers and their Applications, Woodhead Publishing, 2014, pp. 15-44.
- [89] N.C. Estillore, R.C. Advincula, Stimuli-Responsive Binary Mixed Polymer Brushes and Free-Standing Films by LbL-SIP, Langmuir, 27 (2011) 5997-6008.
- [90] N.S. Satarkar, D. Biswal, J.Z. Hilt, Hydrogel nanocomposites: a review of applications as remote controlled biomaterials, Soft Matter, 6 (2010) 2364-2371.
- [91] I. Tokarev, S. Minko, Stimuli-responsive hydrogel thin films, Soft Matter, 5 (2009) 511-524.
- [92] N.S. Satarkar, J.Z. Hilt, Magnetic hydrogel nanocomposites for remote controlled pulsatile drug release, J. Controlled Release, 130 (2008) 246-251.
- [93] S. Wang, M. Liu, K. Kang, Magnetic Nanoparticles and Thermally Responsive Polymer for Targeted Hyperthermia and Sustained Anti-Cancer Drug Delivery, in: W.J. Welch, F. Palm, D.F. Bruley, D.K. Harrison (Eds.) Oxygen Transport to Tissue XXXIV, Springer New York, 2013, pp. 315-321.
- [94] B. Sahoo, K.S.P. Devi, R. Banerjee, T.K. Maiti, P. Pramanik, D. Dhara, Thermal and pH Responsive Polymer-Tethered Multifunctional Magnetic

Nanoparticles for Targeted Delivery of Anticancer Drug, *ACS applied materials & interfaces*, 5 (2013) 3884-3893.

[95] L.A. Tziveleka, P. Bilalis, A. Chatzipavlidis, N. Boukos, G. Kordas, Development of Multiple Stimuli Responsive Magnetic Polymer Nanocontainers as Efficient Drug Delivery Systems, *Macromol. Biosci.*, 14 (2014) 131-141.

[96] H.G. Schild, Poly(N-isopropylacrylamide): experiment, theory and application, *Prog. Polym. Sci.*, 17 (1992) 163-249.

[97] C. Gorey, I.C. Escobar, N-isopropylacrylamide (NIPAAm) modified cellulose acetate ultrafiltration membranes, *J. Membr. Sci.*, 383 (2011) 272-279.

[98] H. Du, R. Wickramasinghe, X. Qian, Effects of Salt on the Lower Critical Solution Temperature of Poly (N-Isopropylacrylamide), *J. Phys. Chem. B*, 114 (2010) 16594-16604.

[99] D. Gan, L.A. Lyon, Synthesis and Protein Adsorption Resistance of PEG-Modified Poly(N-isopropylacrylamide) Core/Shell Microgels, *Macromolecules*, 35 (2002) 9634-9639.

[100] D.E. Bergbreiter, B.L. Case, Y.-S. Liu, J.W. Caraway, Poly(N-isopropylacrylamide) Soluble Polymer Supports in Catalysis and Synthesis, *Macromolecules*, 31 (1998) 6053-6062.

[101] Y. Lu, Y. Mei, M. Drechsler, M. Ballauff, Thermosensitive Core–Shell Particles as Carriers for Ag Nanoparticles: Modulating the Catalytic Activity by a Phase Transition in Networks, *Angew. Chem. Int. Ed.*, 45 (2006) 813-816.

[102] L. Rusen, V. Dinca, B. Mitu, C. Mustaciosu, M. Dinescu, Temperature responsive functional polymeric thin films obtained by matrix assisted pulsed

laser evaporation for cells attachment–detachment study, *Appl. Surf. Sci.*, 302 (2014) 134-140.

[103] G.R. Whittell, M.D. Hager, U.S. Schubert, I. Manners, Functional soft materials from metallopolymers and metallosupramolecular polymers, *Nat Mater*, 10 (2011) 176-188.

[104] N. Sahiner, H. Ozay, O. Ozay, N. Aktas, New catalytic route: Hydrogels as templates and reactors for in situ Ni nanoparticle synthesis and usage in the reduction of 2- and 4-nitrophenols, *Applied Catalysis A: General*, 385 (2010) 201-207.

[105] J.J. Wang, F. Liu, Imparting antifouling properties of silicone hydrogels by grafting poly(ethylene glycol) methyl ether acrylate initiated by UV light, *J. Appl. Polym. Sci.*, 125 (2012) 548-554.

[106] Y.-H. La, B.D. McCloskey, R. Sooriyakumaran, A. Vora, B. Freeman, M. Nassar, J. Hedrick, A. Nelson, R. Allen, Bifunctional hydrogel coatings for water purification membranes: Improved fouling resistance and antimicrobial activity, *J. Membr. Sci.*, 372 (2011) 285-291.

[107] S.L. Doty, T.Q. Shang, A.M. Wilson, J. Tangen, A.D. Westergreen, L.A. Newman, S.E. Strand, M.P. Gordon, Enhanced metabolism of halogenated hydrocarbons in transgenic plants containing mammalian cytochrome P450 2E1, *Proceedings of the National Academy of Sciences*, 97 (2000) 6287-6291.

[108] J.F. Brown, D.L. Bedard, M.J. Brennan, J.C. Carnahan, H. Feng, R.E. Wagner, Polychlorinated Biphenyl Dechlorination in Aquatic Sediments, *Science*, 236 (1987) 709-712.

- [109] L.J. Matheson, P.G. Tratnyek, Reductive Dehalogenation of Chlorinated Methanes by Iron Metal, *Environ. Sci. Technol.*, 28 (1994) 2045-2053.
- [110] P. Clancy, Nanoparticles: Self-assembly finds its own limits, *Nat Nano*, 6 (2011) 540-541.
- [111] T. Pradeep, Anshup, Noble metal nanoparticles for water purification: A critical review, *Thin Solid Films*, 517 (2009) 6441-6478.
- [112] C.-B. Wang, W.-X. Zhang, Synthesizing Nanoscale Iron Particles for Rapid and Complete Dechlorination of TCE and PCBs, *Environ. Sci. Technol.*, 31 (1997) 2154-2156.
- [113] M.A. Shannon, P.W. Bohn, M. Elimelech, J.G. Georgiadis, B.J. Marinas, A.M. Mayes, Science and technology for water purification in the coming decades, *Nature*, 452 (2008) 301-310.
- [114] P.G. Tratnyek, R.L. Johnson, Nanotechnologies for environmental cleanup, *Nano Today*, 1 (2006) 44-48.
- [115] T. Phenrat, N. Saleh, K. Sirk, H.-J. Kim, R. Tilton, G. Lowry, Stabilization of aqueous nanoscale zerovalent iron dispersions by anionic polyelectrolytes: adsorbed anionic polyelectrolyte layer properties and their effect on aggregation and sedimentation, *J. Nanopart. Res.*, 10 (2008) 795-814.
- [116] S.R. Lewis, S. Datta, M. Gui, E.L. Coker, F.E. Huggins, S. Daunert, L. Bachas, D. Bhattacharyya, Reactive nanostructured membranes for water purification, *Proc. Natl. Acad. Sci. U. S. A.*, (2011).
- [117] N.S. Satarkar, J. Zach Hilt, Hydrogel nanocomposites as remote-controlled biomaterials, *Acta Biomater.*, 4 (2008) 11-16.

- [118] F. He, D. Zhao, J. Liu, C.B. Roberts, Stabilization of Fe–Pd Nanoparticles with Sodium Carboxymethyl Cellulose for Enhanced Transport and Dechlorination of Trichloroethylene in Soil and Groundwater, *Industrial & Engineering Chemistry Research*, 46 (2006) 29-34.
- [119] R.A. Frimpong, S. Fraser, J.Z. Hilt, Synthesis and temperature response analysis of magnetic-hydrogel nanocomposites, *Journal of Biomedical Materials Research Part A*, 80A (2007) 1-6.
- [120] M.R. Guilherme, R. Silva, E.M. Girotto, A.F. Rubira, E.C. Muniz, Hydrogels based on PAAm network with PNIPAAm included: hydrophilic-hydrophobic transition measured by the partition of Orange II and Methylene Blue in water, *Polymer*, 44 (2003) 4213-4219.
- [121] E.C. Muniz, G. Geuskens, Influence of temperature on the permeability of polyacrylamide hydrogels and semi-IPNs with poly(N-isopropylacrylamide), *J. Membr. Sci.*, 172 (2000) 287-293.
- [122] E. Adem, G. Burillo, E. Bucio, C. Magaña, M. Avalos-Borja, Characterization of interpenetrating networks of acrylic acid (AAc) and N-isopropylacrylamide (NIPAAm) synthesized by ionizing radiation, *Radiat. Phys. Chem.*, 78 (2009) 549-552.
- [123] S. Chen, L. Jiang, Y. Dan, Preparation and thermal response behavior of poly(N-isopropylacrylamide-co-acrylic acid) microgels via soap-free emulsion polymerization based on AIBN initiator, *J. Appl. Polym. Sci.*, 121 (2011) 3322-3331.

- [124] S. Liu, X. Liu, F. Li, Y. Fang, Y. Wang, J. Yu, Phase behavior of temperature- and pH-sensitive poly(acrylic acid-g-N-isopropylacrylamide) in dilute aqueous solution, *J. Appl. Polym. Sci.*, 109 (2008) 4036-4042.
- [125] S. Lin-Gibson, S. Bencherif, J.A. Cooper, S.J. Wetzel, J.M. Antonucci, B.M. Vogel, F. Horkay, N.R. Washburn, Synthesis and Characterization of PEG Dimethacrylates and Their Hydrogels, *Biomacromolecules*, 5 (2004) 1280-1287.
- [126] M.E. Byrne, E. Oral, J. Zachary Hilt, N.A. Peppas, Networks for recognition of biomolecules: molecular imprinting and micropatterning poly(ethylene glycol)-Containing films, *Polym. Adv. Technol.*, 13 (2002) 798-816.
- [127] J. Zhang, M. Zhang, K. Tang, F. Verpoort, T. Sun, Polymer-Based Stimuli-Responsive Recyclable Catalytic Systems for Organic Synthesis, *Small*, 10 (2014) 32-46.
- [128] W. Li, H. Zhao, P.R. Teasdale, R. John, S. Zhang, Synthesis and characterisation of a polyacrylamide-polyacrylic acid copolymer hydrogel for environmental analysis of Cu and Cd, *React. Funct. Polym.*, 52 (2002) 31-41.
- [129] J. Xu, Synthesis and Reactivity of Membrane-supported Bimetallic Nanoparticles for PCB and Trichloroethylene Dechlorination, in, University of Kentucky, 2007.
- [130] J.T. Nurmi, P.G. Tratnyek, Electrochemical studies of packed iron powder electrodes: Effects of common constituents of natural waters on corrosion potential, *Corros. Sci.*, 50 (2008) 144-154.

- [131] P. Mulvaney, Metal Nanoparticles: Double Layers, Optical Properties, and Electrochemistry, in: Nanoscale Materials in Chemistry, John Wiley & Sons, Inc., 2002, pp. 121-167.
- [132] S.M.C. Ritchie, K.E. Kissick, L.G. Bachas, S.K. Sikdar, C. Parikh, D. Bhattacharyya, Polycysteine and Other Polyamino Acid Functionalized Microfiltration Membranes for Heavy Metal Capture, Environ. Sci. Technol., 35 (2001) 3252-3258.
- [133] Y.M. Mohan, P.S.K. Murthy, J. Sreeramulu, K.M. Raju, Swelling behavior of semi-interpenetrating polymer network hydrogels composed of poly(vinyl alcohol) and poly(acrylamide-co-sodium methacrylate), J. Appl. Polym. Sci., 98 (2005) 302-314.
- [134] H. Yu, D.W. Grainger, Thermo-sensitive swelling behavior in crosslinked N-isopropylacrylamide networks: Cationic, anionic, and ampholytic hydrogels, J. Appl. Polym. Sci., 49 (1993) 1553-1563.
- [135] J.A. Jaber, J.B. Schlenoff, Polyelectrolyte Multilayers with Reversible Thermal Responsivity, Macromolecules, 38 (2005) 1300-1306.
- [136] B.D. Barr-Howell, N.A. Peppas, Importance of junction functionality in highly crosslinked polymers, Polym. Bull., 13 (1985) 91-96.
- [137] Y.H. Bae, T. Okano, S.W. Kim, Temperature dependence of swelling of crosslinked poly(N,N'-alkyl substituted acrylamides) in water, J. Polym. Sci., Part B: Polym. Phys., 28 (1990) 923-936.
- [138] R. Ghosh, Novel membranes for simulating biological barrier transport, J. Membr. Sci., 192 (2001) 145-154.

- [139] Y. Kiso, Y. Sugiura, T. Kitao, K. Nishimura, Effects of hydrophobicity and molecular size on rejection of aromatic pesticides with nanofiltration membranes, *J. Membr. Sci.*, 192 (2001) 1-10.
- [140] H.-L. Lien, W.-x. Zhang, Nanoscale iron particles for complete reduction of chlorinated ethenes, *Colloids Surf. Physicochem. Eng. Aspects*, 191 (2001) 97-105.
- [141] J. Xu, A. Dozier, D. Bhattacharyya, Synthesis of Nanoscale Bimetallic Particles in Polyelectrolyte Membrane Matrix for Reductive Transformation of Halogenated Organic Compounds, *J. Nanopart. Res.*, 7 (2005) 449-467.
- [142] V. Polshettiwar, R.S. Varma, Green chemistry by nano-catalysis, *Green Chemistry*, 12 (2010) 743-754.
- [143] G.E. Hoag, J.B. Collins, J.L. Holcomb, J.R. Hoag, M.N. Nadagouda, R.S. Varma, Degradation of bromothymol blue by 'greener' nano-scale zero-valent iron synthesized using tea polyphenols, *J. Mater. Chem.*, 19 (2009) 8671-8677.
- [144] V. Smuleac, R. Varma, S. Sikdar, D. Bhattacharyya, Green Synthesis of Fe and Fe/Pd Bimetallic Nanoparticles in Membranes for Reductive Degradation of Chlorinated Organics, *J. Membr. Sci.*, 379 (2011) 131-137.
- [145] D.E. Meyer, S. Hampson, L. Ormsbee, D. Bhattacharyya, A study of groundwater matrix effects for the destruction of trichloroethylene using Fe/Pd nanoaggregates, *Environmental Progress & Sustainable Energy*, 28 (2009) 507-518.
- [146] S.J. Bransfield, D.M. Cwiertny, K. Livi, D.H. Fairbrother, Influence of transition metal additives and temperature on the rate of organohalide reduction

by granular iron: Implications for reaction mechanisms, *Appl. Catal., B*, 76 (2007) 348-356.

[147] A. Borgschulte, R.J. Westerwaal, J.H. Rector, H. Schreuders, B. Dam, R. Griessen, Catalytic activity of noble metals promoting hydrogen uptake, *J. Catal.*, 239 (2006) 263-271.

[148] G.K. Parshetti, R.-a. Doong, Dechlorination of chlorinated hydrocarbons by bimetallic Ni/Fe immobilized on polyethylene glycol-grafted microfiltration membranes under anoxic conditions, *Chemosphere*, 86 (2012) 392-399.

[149] V. Smuleac, R. Varma, B. Baruwati, S. Sikdar, D. Bhattacharyya, Nanostructured Membranes for Enzyme Catalysis and Green Synthesis of Nanoparticles, *ChemSusChem*, 4 (2011) 1773-1777.

[150] V. Smuleac, L. Bachas, D. Bhattacharyya, Aqueous-phase synthesis of PAA in PVDF membrane pores for nanoparticle synthesis and dichlorobiphenyl degradation, *J. Membr. Sci.*, 346 (2010) 310-317.

[151] J.D. Debord, L.A. Lyon, Synthesis and Characterization of pH-Responsive Copolymer Microgels with Tunable Volume Phase Transition Temperatures, *Langmuir*, 19 (2003) 7662-7664.

[152] H. Feil, Y.H. Bae, F. Jan, S.W. Kim, Effect of comonomer hydrophilicity and ionization on the lower critical solution temperature of N-isopropylacrylamide copolymers, *Macromolecules*, 26 (1993) 2496-2500.

[153] D. Kuckling, M.E. Harmon, C.W. Frank, Photo-Cross-Linkable PNIPAAm Copolymers. 1. Synthesis and Characterization of Constrained Temperature-Responsive Hydrogel Layers, *Macromolecules*, 35 (2002) 6377-6383.

- [154] A.R. Tao, S. Habas, P. Yang, Shape control of colloidal metal nanocrystals, *Small*, 4 (2008) 310-325.
- [155] V. THOMAS, M. NAMDEO, Y.M. MOHAN, S.K. BAJPAI, M. BAJPAI, Review on Polymer, Hydrogel and Microgel Metal Nanocomposites: A Facile Nanotechnological Approach, *Journal of Macromolecular Science, Part A: Pure and Applied Chemistry*, 45 (2007) 107-119.
- [156] R. Dai, Z. Liu, Y. Liang, F. Geng, C. Ge, K. Ullah, F. Lv, Y. Zhang, Y. Deng, Separation of peptides with an aqueous mobile phase by temperature-responsive chromatographic column (*J. Sep. Science* 35'16), *J. Sep. Sci.*, 35 (2012) NA-NA.
- [157] C. Alexander, Stimuli-responsive hydrogels: Drugs take control, *Nat Mater*, 7 (2008) 767-768.
- [158] K. Sieradzki, Potential Solutions for Creating Responsive Materials, *Science*, 332 (2011) 1158-1159.
- [159] R.A. Pérez, J.-E. Won, J.C. Knowles, H.-W. Kim, Naturally and synthetic smart composite biomaterials for tissue regeneration, *Adv. Drug Del. Rev.*, 65 (2013) 471-496.
- [160] J. Kobayashi, Y. Akiyama, M. Yamato, T. Okano, 5.06 - Biomaterials: Temperature-Responsive Polymer, in: M.-Y. Editor-in-Chief: Murray (Ed.) *Comprehensive Biotechnology (Second Edition)*, Academic Press, Burlington, 2011, pp. 51-64.
- [161] E. Fleige, M.A. Quadir, R. Haag, Stimuli-responsive polymeric nanocarriers for the controlled transport of active compounds: Concepts and applications, *Adv. Drug Del. Rev.*, 64 (2012) 866-884.

- [162] L. Ying, P. Wang, E.T. Kang, K.G. Neoh, Synthesis and Characterization of Poly(acrylic acid)-graft-poly(vinylidene fluoride) Copolymers and pH-Sensitive Membranes, *Macromolecules*, 35 (2001) 673-679.
- [163] S. Çakmak, A.S. Çakmak, M. Gümüşderelioğlu, PNIPAAm-grafted thermoresponsive microcarriers: Surface-initiated ATRP synthesis and characterization, *Materials Science and Engineering: C*, 33 (2013) 3033-3040.
- [164] E. Costa, M.M. Lloyd, C. Chopko, A. Aguiar-Ricardo, P.T. Hammond, Tuning Smart Microgel Swelling and Responsive Behavior through Strong and Weak Polyelectrolyte Pair Assembly, *Langmuir*, 28 (2012) 10082-10090.
- [165] Y. Zhang, H.F. Chan, K.W. Leong, Advanced materials and processing for drug delivery: The past and the future, *Adv. Drug Del. Rev.*, 65 (2013) 104-120.
- [166] Q. Fan, K.K. Sirkar, J. Wu, A thermo-sensitive release system based on polymeric membrane for transdermal delivery of doxycycline HCl, *J. Membr. Sci.*, 337 (2009) 175-181.
- [167] D. Roy, J.N. Cambre, B.S. Sumerlin, Future perspectives and recent advances in stimuli-responsive materials, *Prog. Polym. Sci.*, 35 (2010) 278-301.
- [168] J. Huang, X.-L. Wang, W.-S. Qi, X.-H. Yu, Temperature sensitivity and electrokinetic behavior of a N-isopropylacrylamide grafted microporous polyethylene membrane, *Desalination*, 146 (2002) 345-351.
- [169] L. Liang, M. Shi, V.V. Viswanathan, L.M. Peurrung, J.S. Young, Temperature-sensitive polypropylene membranes prepared by plasma polymerization, *J. Membr. Sci.*, 177 (2000) 97-108.

- [170] N.I. Shtanko, V.Y. Kabanov, P.Y. Apel, M. Yoshida, A.I. Vilenskii, Preparation of permeability-controlled track membranes on the basis of 'smart' polymers, *J. Membr. Sci.*, 179 (2000) 155-161.
- [171] S.J. Lue, C.-H. Chen, C.-M. Shih, M.-C. Tsai, C.-Y. Kuo, J.-Y. Lai, Grafting of poly(N-isopropylacrylamide-co-acrylic acid) on micro-porous polycarbonate films: Regulating lower critical solution temperatures for drug controlled release, *J. Membr. Sci.*, 379 (2011) 330-340.
- [172] X. Tan, S.P. Tan, W.K. Teo, K. Li, Polyvinylidene fluoride (PVDF) hollow fibre membranes for ammonia removal from water, *J. Membr. Sci.*, 271 (2006) 59-68.
- [173] S.R. Lewis, S. Datta, M. Gui, E.L. Coker, F.E. Huggins, S. Daunert, L. Bachas, D. Bhattacharyya, Reactive nanostructured membranes for water purification, *Proceedings of the National Academy of Sciences*, 108 (2011) 8577-8582.
- [174] Y. Li, L.-Y. Chu, J.-H. Zhu, H.-D. Wang, S.-L. Xia, W.-M. Chen, Thermoresponsive Gating Characteristics of Poly(N-isopropylacrylamide)-Grafted Porous Poly(vinylidene fluoride) Membranes, *Industrial & Engineering Chemistry Research*, 43 (2004) 2643-2649.
- [175] J.-Z. Yu, L.-P. Zhu, B.-K. Zhu, Y.-Y. Xu, Poly(N-isopropylacrylamide) grafted poly(vinylidene fluoride) copolymers for temperature-sensitive membranes, *J. Membr. Sci.*, 366 (2011) 176-183.
- [176] Z. Chen, Z.-M. Cui, C.-Y. Cao, W.-D. He, L. Jiang, W.-G. Song, Temperature-Responsive Smart Nanoreactors: Poly(N-isopropylacrylamide)-

Coated Au@Mesoporous-SiO₂ Hollow Nanospheres, *Langmuir*, 28 (2012) 13452-13458.

[177] H. Susanto, M. Ulbricht, Photografted Thin Polymer Hydrogel Layers on PES Ultrafiltration Membranes: Characterization, Stability, and Influence on Separation Performance, *Langmuir*, 23 (2007) 7818-7830.

[178] M. Gui, L.E. Ormsbee, D. Bhattacharyya, Reactive Functionalized Membranes for Polychlorinated Biphenyl Degradation, *Industrial & Engineering Chemistry Research*, 52 (2013) 10430-10440.

[179] S.J. Lue, J.-J. Hsu, C.-H. Chen, B.-C. Chen, Thermally on-off switching membranes of poly(N-isopropylacrylamide) immobilized in track-etched polycarbonate films, *J. Membr. Sci.*, 301 (2007) 142-150.

[180] Z.M.O. Rzaev, S. Dinçer, E. Piskin, Functional copolymers of N-isopropylacrylamide for bioengineering applications, *Prog. Polym. Sci.*, 32 (2007) 534-595.

[181] L. Ying, W.H. Yu, E.T. Kang, K.G. Neoh, Functional and Surface-Active Membranes from Poly(vinylidene fluoride)-graft-Poly(acrylic acid) Prepared via RAFT-Mediated Graft Copolymerization, *Langmuir*, 20 (2004) 6032-6040.

[182] L. Ying, E.T. Kang, K.G. Neoh, Synthesis and Characterization of Poly(N-isopropylacrylamide)-graft-Poly(vinylidene fluoride) Copolymers and Temperature-Sensitive Membranes, *Langmuir*, 18 (2002) 6416-6423.

[183] Z. Cheng, X. Zhu, E.T. Kang, K.G. Neoh, Modification of Poly(ether imide) Membranes via Surface-Initiated Atom Transfer Radical Polymerization, *Macromolecules*, 39 (2006) 1660-1663.

- [184] T.P. Russell, Surface-Responsive Materials, *Science*, 297 (2002) 964-967.
- [185] P.S. Curti, M.R. De Moura, E. Radovanovic, A.F. Rubira, E.C. Muniz, R.A. Moliterno, Surface modification of polystyrene and poly(ethylene terephthalate) by grafting poly(N-isopropylacrylamide), *J Mater Sci Mater Med*, 13 (2002) 1175-1180.
- [186] W. Xiaoling, G.M. Marian, Grafting of poly(N - isopropylacrylamide) onto nylon and polystyrene surfaces by atmospheric plasma treatment followed with free radical graft copolymerization, *J. Appl. Polym. Sci.*, 104 (2007) 3614-3621.
- [187] N. Vandecasteele, D. Merche, F. Reniers, XPS and contact angle study of N₂ and O₂ plasma-modified PTFE, PVDF and PVF surfaces, *Surf. Interface Anal.*, 38 (2006) 526-530.
- [188] G. Beamson, D. Briggs, High resolution XPS of organic polymers, the scienta ESCA300 database. , Wiley, New York, 1992.
- [189] L. Ying, E.T. Kang, K.G. Neoh, Characterization of membranes prepared from blends of poly(acrylic acid)-graft-poly(vinylidene fluoride) with poly(N-isopropylacrylamide) and their temperature- and pH-sensitive microfiltration, *J. Membr. Sci.*, 224 (2003) 93-106.
- [190] X.-L. Wang, J. Huang, X.-Z. Chen, X.-H. Yu, Graft polymerization of N-isopropylacrylamide into a microporous polyethylene membrane by the plasma method: technique and morphology, *Desalination*, 146 (2002) 337-343.
- [191] J.C. Reijenga, L.G. Gagliardi, E. Kenndler, Temperature dependence of acidity constants, a tool to affect separation selectivity in capillary electrophoresis, *J. Chromatogr. A*, 1155 (2007) 142-145.

- [192] Y.-C. Chen, R. Xie, L.-Y. Chu, Stimuli-responsive gating membranes responding to temperature, pH, salt concentration and anion species, *J. Membr. Sci.*, 442 (2013) 206-215.
- [193] J.K. Shim, Y.B. Lee, Y.M. Lee, pH-dependent permeation through polysulfone ultrafiltration membranes prepared by ultraviolet polymerization technique, *J. Appl. Polym. Sci.*, 74 (1999) 75-82.
- [194] C.D. Jones, L.A. Lyon, Dependence of Shell Thickness on Core Compression in Acrylic Acid Modified Poly(N-isopropylacrylamide) Core/Shell Microgels, *Langmuir*, 19 (2003) 4544-4547.
- [195] Z. Xing, C. Wang, J. Yan, L. Zhang, L. Li, L. Zha, pH/temperature dual stimuli-responsive microcapsules with interpenetrating polymer network structure, *Colloid. Polym. Sci.*, 288 (2010) 1723-1729.
- [196] M.C.Y. Wong, K. Martinez, G.Z. Ramon, E.M.V. Hoek, Impacts of operating conditions and solution chemistry on osmotic membrane structure and performance, *Desalination*, 287 (2012) 340-349.
- [197] L. Xiao, A.B. Isner, J.Z. Hilt, D. Bhattacharyya, Temperature responsive hydrogel with reactive nanoparticles, *J. Appl. Polym. Sci.*, 128 (2013) 1804-1814.
- [198] J. Xu, D. Bhattacharyya, Fe/Pd Nanoparticle Immobilization in Microfiltration Membrane Pores: Synthesis, Characterization, and Application in the Dechlorination of Polychlorinated Biphenyls, *Industrial & Engineering Chemistry Research*, 46 (2006) 2348-2359.
- [199] F. Liu, N.A. Hashim, Y. Liu, M.R.M. Abed, K. Li, Progress in the production and modification of PVDF membranes, *J. Membr. Sci.*, 375 (2011) 1-27.

- [200] G.-d. Kang, Y.-m. Cao, Application and modification of poly(vinylidene fluoride) (PVDF) membranes – A review, *J. Membr. Sci.*, 463 (2014) 145-165.
- [201] T. Qu, K. Pan, L. Li, B. Liang, L. Wang, B. Cao, Influence of Ultrasonication Conditions on the Structure and Performance of Poly(vinylidene fluoride) Membranes Prepared by the Phase Inversion Method, *Industrial & Engineering Chemistry Research*, 53 (2014) 8228-8234.
- [202] Z. Cui, E. Drioli, Y.M. Lee, Recent progress in fluoropolymers for membranes, *Prog. Polym. Sci.*, 39 (2014) 164-198.
- [203] J.F. Hester, A.M. Mayes, Design and performance of foul-resistant poly(vinylidene fluoride) membranes prepared in a single-step by surface segregation, *J. Membr. Sci.*, 202 (2002) 119-135.
- [204] M. Rahbari-Sisakht, D. Rana, T. Matsuura, D. Emadzadeh, M. Padaki, A.F. Ismail, Study on CO₂ stripping from water through novel surface modified PVDF hollow fiber membrane contactor, *Chem. Eng. J.*, 246 (2014) 306-310.
- [205] R. Thomas, E. Guillen-Burrieza, H.A. Arafat, Pore structure control of PVDF membranes using a 2-stage coagulation bath phase inversion process for application in membrane distillation (MD), *J. Membr. Sci.*, 452 (2014) 470-480.
- [206] J. Lu, S.-G. Kim, S. Lee, I.-K. Oh, A Biomimetic Actuator Based on an Ionic Networking Membrane of Poly(styrene-*alt*-maleimide)-Incorporated Poly(vinylidene fluoride), *Adv. Funct. Mater.*, 18 (2008) 1290-1298.
- [207] A.M. Mika, R.F. Childs, J.M. Dickson, B.E. McCarry, D.R. Gagnon, A new class of polyelectrolyte-filled microfiltration membranes with environmentally controlled porosity, *J. Membr. Sci.*, 108 (1995) 37-56.

- [208] A.M. Mika, R.F. Childs, J.M. Dickson, Chemical valves based on poly(4-vinylpyridine)-filled microporous membranes, *J. Membr. Sci.*, 153 (1999) 45-56.
- [209] L. Xiao, A. Isner, K. Waldrop, A. Saad, D. Takigawa, D. Bhattacharyya, Development of bench and full-scale temperature and pH responsive functionalized PVDF membranes with tunable properties, *J. Membr. Sci.*, 457 (2014) 39-49.
- [210] K. Ishihara, M. Kobayashi, N. Ishimaru, I. Shinohara, GLUCOSE INDUCED PERMEATION CONTROL OF INSULIN THROUGH A COMPLEX MEMBRANE CONSISTING OF IMMOBILIZED GLUCOSE OXIDASE AND A POLY(AMINE), *Polym. J.*, 16 (1984) 625-631.
- [211] K. Ishihara, N. Muramoto, I. Shinohara, CONTROLLED RELEASE OF ORGANIC SUBSTANCES USING POLYMER MEMBRANE WITH RESPONSIVE FUNCTION FOR AMINO COMPOUNDS, *J. Appl. Polym. Sci.*, 29 (1984) 211-217.
- [212] S.P. Nunes, M.L. Sforça, K.-V. Peinemann, Dense hydrophilic composite membranes for ultrafiltration, *J. Membr. Sci.*, 106 (1995) 49-56.
- [213] L.E.S. Brink, S.J.G. Elbers, T. Robbertsen, P. Both, The anti-fouling action of polymers preadsorbed on ultrafiltration and microfiltration membranes, *J. Membr. Sci.*, 76 (1993) 281-291.
- [214] H. Iwata, T. Matsuda, Preparation and properties of novel environment-sensitive membranes prepared by graft polymerization onto a porous membrane, *J. Membr. Sci.*, 38 (1988) 185-199.

- [215] S. Akhtar, C. Hawes, L. Dudley, I. Reed, P. Stratford, Coatings reduce the fouling of microfiltration membranes, *J. Membr. Sci.*, 107 (1995) 209-218.
- [216] S. Munari, A. Bottino, G. Capannelli, Casting and performance of poly(vinylidene fluoride) based membranes, *J. Membr. Sci.*, 16 (1983) 181-193.
- [217] Z.Z. Laizhou SONG, Shizhe SONG, Zhiming GAO, Preparation and Characterization of the Modified Poly(vinylidene Fluoride) (PVDF) Hollow Fibre Microfiltration Membrane, *J. Mater. Sci. Technol.*, 23 (2007) 55-60.
- [218] G.J. Ross, J.F. Watts, M.P. Hill, P. Morrissey, Surface modification of poly(vinylidene fluoride) by alkaline treatment¹. The degradation mechanism, *Polymer*, 41 (2000) 1685-1696.
- [219] J. WOOTHIKANOKKHAN, P. CHANGSUWAN, Dehydrofluorination of PVDF and Proton Conductivity of the Modified PVDF/Sulfonated SEBS Blend Membranes, *Journal of Metals, Materials and Minerals*, 18 (2008) 57-62.
- [220] H. Kise, H. Ogata, Phase transfer catalysis in dehydrofluorination of poly(vinylidene fluoride) by aqueous sodium hydroxide solutions, *Journal of Polymer Science: Polymer Chemistry Edition*, 21 (1983) 3443-3451.
- [221] E.D. Owen, M. Shah, M.V. Twigg, Phase transfer catalysed degradation of poly(vinyl chloride). I: Product characterisation and handling, *Polym. Degrad. Stab.*, 51 (1996) 151-158.
- [222] R. Crowe, J.P.S. Badyal, Surface modification of poly(vinylidene difluoride)(PVDF) by LiOH, *J. Chem. Soc., Chem. Commun.*, (1991) 958-959.

- [223] A. Bottino, G. Camera-Roda, G. Capannelli, S. Munari, The formation of microporous polyvinylidene difluoride membranes by phase separation, *J. Membr. Sci.*, 57 (1991) 1-20.
- [224] A.C. Sun, W. Kosar, Y. Zhang, X. Feng, A study of thermodynamics and kinetics pertinent to formation of PVDF membranes by phase inversion, *Desalination*, 309 (2013) 156-164.
- [225] E. Fontananova, J.C. Jansen, A. Cristiano, E. Curcio, E. Drioli, Effect of additives in the casting solution on the formation of PVDF membranes, *Desalination*, 192 (2006) 190-197.
- [226] M. Gu, J. Zhang, X. Wang, H. Tao, L. Ge, Formation of poly(vinylidene fluoride) (PVDF) membranes via thermally induced phase separation, *Desalination*, 192 (2006) 160-167.
- [227] H.H. Himstedt, H. Du, K.M. Marshall, S.R. Wickramasinghe, X. Qian, pH Responsive Nanofiltration Membranes for Sugar Separations, *Industrial & Engineering Chemistry Research*, 52 (2013) 9259-9269.
- [228] C. Zhao, S. Nie, M. Tang, S. Sun, Polymeric pH-sensitive membranes—A review, *Prog. Polym. Sci.*, 36 (2011) 1499-1520.
- [229] A.M. Hollman, D. Bhattacharyya, Controlled Permeability and Ion Exclusion in Microporous Membranes Functionalized with Poly(l-glutamic acid), *Langmuir*, 18 (2002) 5946-5952.
- [230] J.O. Abitoye, P. Mukherjee, K. Jones, Ion Implantation: Effect on Flux and Rejection Properties of NF Membranes†, *Environ. Sci. Technol.*, 39 (2005) 6487-6493.

- [231] J. Song, X.-M. Li, A. Figoli, H. Huang, C. Pan, T. He, B. Jiang, Composite hollow fiber nanofiltration membranes for recovery of glyphosate from saline wastewater, *Water Res.*, 47 (2013) 2065-2074.
- [232] W.-x. Zhang, C.-B. Wang, H.-L. Lien, Treatment of chlorinated organic contaminants with nanoscale bimetallic particles, *Catal. Today*, 40 (1998) 387-395.
- [233] F.-L. Mi, S.-S. Shyu, Y.-B. Wu, S.-T. Lee, J.-Y. Shyong, R.-N. Huang, Fabrication and characterization of a sponge-like asymmetric chitosan membrane as a wound dressing, *Biomaterials*, 22 (2001) 165-173.
- [234] J. Xu, D. Bhattacharyya, Fe/Pd Nanoparticle Immobilization in Microfiltration Membrane Pores: Synthesis, Characterization, and Application in the Dechlorination of Polychlorinated Biphenyls, *Industrial & Engineering Chemistry Research*, 46 (2006) 2348-2359.
- [235] N. Hilal, H. Al-Zoubi, N.A. Darwish, A.W. Mohamma, M. Abu Arabi, A comprehensive review of nanofiltration membranes: Treatment, pretreatment, modelling, and atomic force microscopy, *Desalination*, 170 (2004) 281-308.
- [236] S. Cheng, D.L. Oatley, P.M. Williams, C.J. Wright, Positively charged nanofiltration membranes: Review of current fabrication methods and introduction of a novel approach, *Adv. Colloid Interface Sci.*, 164 (2011) 12-20.
- [237] J. Zhao, Y. Su, X. He, X. Zhao, Y. Li, R. Zhang, Z. Jiang, Dopamine composite nanofiltration membranes prepared by self-polymerization and interfacial polymerization, *J. Membr. Sci.*, 465 (2014) 41-48.

- [238] A.W. Mohammad, R.K. Basha, C.P. Leo, Nanofiltration of glucose solution containing salts: Effects of membrane characteristics, organic component and salts on retention, *J. Food Eng.*, 97 (2010) 510-518.
- [239] J. Shirley, S. Mandale, V. Kochkodan, Influence of solute concentration and dipole moment on the retention of uncharged molecules with nanofiltration, *Desalination*, 344 (2014) 116-122.
- [240] Y. Zhang, Y. Su, J. Peng, X. Zhao, J. Liu, J. Zhao, Z. Jiang, Composite nanofiltration membranes prepared by interfacial polymerization with natural material tannic acid and trimesoyl chloride, *J. Membr. Sci.*, 429 (2013) 235-242.
- [241] S.C. Low, C. Liping, L.S. Hee, Water softening using a generic low cost nano-filtration membrane, *Desalination*, 221 (2008) 168-173.
- [242] K. Yoon, B.S. Hsiao, B. Chu, High flux nanofiltration membranes based on interfacially polymerized polyamide barrier layer on polyacrylonitrile nanofibrous scaffolds, *J. Membr. Sci.*, 326 (2009) 484-492.
- [243] M. Elimelech, W.A. Phillip, The Future of Seawater Desalination: Energy, Technology, and the Environment, *Science*, 333 (2011) 712-717.
- [244] L. Peeva, J.d.S. Burgal, I. Valtcheva, A.G. Livingston, Continuous purification of active pharmaceutical ingredients using multistage organic solvent nanofiltration membrane cascade, *Chem. Eng. Sci.*, 116 (2014) 183-194.
- [245] M.N.A. Seman, M. Khayet, N. Hilal, Nanofiltration thin-film composite polyester polyethersulfone-based membranes prepared by interfacial polymerization, *J. Membr. Sci.*, 348 (2010) 109-116.

- [246] J. Xiang, Z. Xie, M. Hoang, D. Ng, K. Zhang, Effect of ammonium salts on the properties of poly(piperazineamide) thin film composite nanofiltration membrane, *J. Membr. Sci.*, 465 (2014) 34-40.
- [247] J. Xiang, Z. Xie, M. Hoang, K. Zhang, Effect of amine salt surfactants on the performance of thin film composite poly(piperazine-amide) nanofiltration membranes, *Desalination*, 315 (2013) 156-163.
- [248] X. Wang, T.-M. Yeh, Z. Wang, R. Yang, R. Wang, H. Ma, B.S. Hsiao, B. Chu, Nanofiltration membranes prepared by interfacial polymerization on thin-film nanofibrous composite scaffold, *Polymer*, 55 (2014) 1358-1366.
- [249] W. Fang, L. Shi, R. Wang, Interfacially polymerized composite nanofiltration hollow fiber membranes for low-pressure water softening, *J. Membr. Sci.*, 430 (2013) 129-139.
- [250] J. Jegal, S.G. Min, K.-H. Lee, Factors affecting the interfacial polymerization of polyamide active layers for the formation of polyamide composite membranes, *J. Appl. Polym. Sci.*, 86 (2002) 2781-2787.
- [251] W.R. Bowen, J.S. Welfoot, Predictive modelling of nanofiltration: membrane specification and process optimisation, *Desalination*, 147 (2002) 197-203.
- [252] C. Umpuch, S. Galier, S. Kanchanatawee, H.R.-d. Balmann, Nanofiltration as a purification step in production process of organic acids: Selectivity improvement by addition of an inorganic salt, *Process Biochem.*, 45 (2010) 1763-1768.
- [253] G. Trägårdh, V. Gekas, Membrane technology in the sugar industry, *Desalination*, 69 (1988) 9-17.

- [254] A. Hinkova, Z. Bubnik, P. Kadlec, V. Pour, H. Starhova, Membrane filtration in the sugar industry, CHEMICAL PAPERS-SLOVAK ACADEMY OF SCIENCES, 54 (2001) 375-382.
- [255] A. Hinkova, Z. Bubník, P. Kadlec, J. Pridal, Potentials of separation membranes in the sugar industry, Sep. Purif. Technol., 26 (2002) 101-110.
- [256] X.-L. Wang, C. Zhang, P. Ouyang, The possibility of separating saccharides from a NaCl solution by using nanofiltration in diafiltration mode, J. Membr. Sci., 204 (2002) 271-281.
- [257] G. Bargeman, J.M. Vollenbroek, J. Straatsma, C.G.P.H. Schroën, R.M. Boom, Nanofiltration of multi-component feeds. Interactions between neutral and charged components and their effect on retention, J. Membr. Sci., 247 (2005) 11-20.
- [258] A. Bouchoux, H.R.-d. Balmann, F. Lutin, Nanofiltration of glucose and sodium lactate solutions: Variations of retention between single- and mixed-solute solutions, J. Membr. Sci., 258 (2005) 123-132.
- [259] N.a. Ali, A.W. Mohammad, A.L. Ahmad, Use of nanofiltration predictive model for membrane selection and system cost assessment, Sep. Purif. Technol., 41 (2005) 29-37.
- [260] D.L. Oatley-Radcliffe, S.R. Williams, M.S. Barrow, P.M. Williams, Critical appraisal of current nanofiltration modelling strategies for seawater desalination and further insights on dielectric exclusion, Desalination, 343 (2014) 154-161.
- [261] E. Vellenga, G. Trägårdh, Nanofiltration of combined salt and sugar solutions: coupling between retentions, Desalination, 120 (1998) 211-220.

- [262] P. Pal, P. Dey, Process intensification in lactic acid production by three stage membrane integrated hybrid reactor system, *Chemical Engineering and Processing: Process Intensification*, 64 (2013) 1-9.
- [263] W.R. Bowen, A.W. Mohammad, N. Hilal, Characterisation of nanofiltration membranes for predictive purposes — use of salts, uncharged solutes and atomic force microscopy, *J. Membr. Sci.*, 126 (1997) 91-105.
- [264] N.K. Saha, S.V. Joshi, Performance evaluation of thin film composite polyamide nanofiltration membrane with variation in monomer type, *J. Membr. Sci.*, 342 (2009) 60-69.
- [265] Y. Mansourpanah, S.S. Madaeni, A. Rahimpour, Fabrication and development of interfacial polymerized thin-film composite nanofiltration membrane using different surfactants in organic phase; study of morphology and performance, *J. Membr. Sci.*, 343 (2009) 219-228.
- [266] N. Hilal, H. Al-Zoubi, N.A. Darwish, A.W. Mohammad, Characterisation of nanofiltration membranes using atomic force microscopy, *Desalination*, 177 (2005) 187-199.
- [267] S. Déon, P. Dutournié, P. Bourseau, Transfer of monovalent salts through nanofiltration membranes: A model combining transport through pores and the polarization layer, *Ind. Eng. Chem. Res.*, 46 (2007) 6752-6761.
- [268] W.R. Bowen, J.S. Welfoot, Modelling the performance of membrane nanofiltration—critical assessment and model development, *Chem. Eng. Sci.*, 57 (2002) 1121-1137.

- [269] F.J. Benítez, J.L. Acero, A.I. Leal, M. González, The use of ultrafiltration and nanofiltration membranes for the purification of cork processing wastewater, *J. Hazard. Mater.*, 162 (2009) 1438-1445.
- [270] F.G. Donnan, Theory of membrane equilibria and membrane potentials in the presence of non-dialysing electrolytes. A contribution to physical-chemical physiology, *J. Membr. Sci.*, 100 (1995) 45-55.
- [271] X.-L. Wang, W.-N. Wang, D.-X. Wang, Experimental investigation on separation performance of nanofiltration membranes for inorganic electrolyte solutions, *Desalination*, 145 (2002) 115-122.
- [272] W.R. Bowen, H. Mukhtar, Characterisation and prediction of separation performance of nanofiltration membranes, *J. Membr. Sci.*, 112 (1996) 263-274.
- [273] R.t. Shannon, Revised effective ionic radii and systematic studies of interatomic distances in halides and chalcogenides, *Acta Crystallographica Section A: Crystal Physics, Diffraction, Theoretical and General Crystallography*, 32 (1976) 751-767.
- [274] E.L. Cussler, *Diffusion: mass transfer in fluid systems*, Cambridge university press, 2009.
- [275] S. Déon, A. Escoda, P. Fievet, A transport model considering charge adsorption inside pores to describe salts rejection by nanofiltration membranes, *Chem. Eng. Sci.*, 66 (2011) 2823-2832.
- [276] B. Cuartas-Uribe, M.C. Vincent-Vela, S. Álvarez-Blanco, M.I. Alcaina-Miranda, E. Soriano-Costa, Nanofiltration of sweet whey and prediction of lactose

retention as a function of permeate flux using the Kedem–Spiegler and Donnan Steric Partitioning models, *Sep. Purif. Technol.*, 56 (2007) 38-46.

[277] S.S. Sablani, M.F.A. Goosen, R. Al-Belushi, M. Wilf, Concentration polarization in ultrafiltration and reverse osmosis: a critical review, *Desalination*, 141 (2001) 269-289.

[278] X.-L. Wang, W.-J. Shang, D.-X. Wang, L. Wu, C.-H. Tu, Characterization and applications of nanofiltration membranes: State of the art, *Desalination*, 236 (2009) 316-326.

[279] C.Y. Tang, Q.S. Fu, C.S. Criddle, J.O. Leckie, Effect of Flux (Transmembrane Pressure) and Membrane Properties on Fouling and Rejection of Reverse Osmosis and Nanofiltration Membranes Treating Perfluorooctane Sulfonate Containing Wastewater, *Environ. Sci. Technol.*, 41 (2007) 2008-2014.

[280] H. Tsutsui, M. Moriyama, D. Nakayama, R. Ishii, R. Akashi, Synthesis and Temperature-Responsive Properties of Novel Semi-interpenetrating Polymer Networks Consisting of a Poly(acrylamide) Polymer Network and Linear Poly(acrylic acid) Chains, *Macromolecules*, 39 (2006) 2291-2297.

Vita

Li Xiao graduated with a B.S. degree in Chemical Engineering at Tianjin University, Tianjin, China in July 2007. Later, she was recommended to graduate school at Tianjin University without examination due to her excellent undergraduate performance. She received her master degree in Chemical Engineering in Tianjin University, Tianjin, China in July 2009. In August 2009, she began her Ph.D. in Chemical Engineering under the guidance of Prof. Dibakar Bhattacharyya at University of Kentucky.

Awards & Honors:

- 2014 AIChE Separations Division Graduate Student Research Award (June, 2014)
- University of Kentucky Outstanding Graduate Student Award (May, 2014)
- North American Membrane Society (NAMS) Elias Klein award (June, 2011)
- PPG Industries Scholarship (Fall 2008)
- HUA-CHEM Chemical Company Scholarship (Fall 2006)

Publications:

- Xiao, L.; Bhattacharyya, D. "Nanofiltration of Sugar Containing Salt: Interaction between Sugar and Salt on Retention" *to be submitted to J. Membr. Sci.*
- Xiao, L.; Davenport, D.; Bhattacharyya, D. "Polymerization and Functionalization of Membrane Pores for Water Related Applications" *to be submitted to Industrial and Engineering Chemistry Research (2014).*
- Xiao, L.; Isner, A.; Waldrop, K.; Saad, A.; Takigawa, D.; Bhattacharyya, D. "Development of Bench and Full-Scale Temperature and pH Responsive

Functionalized PVDF Membranes with Tunable Properties”. *J. Membr. Sci.* 457 (0), 39-49 (2014).

- Xiao, L.; Isner, A. B.; Hilt, J. Z.; Bhattacharyya, D. “Temperature responsive hydrogel with reactive nanoparticles”. *J. Appl. Polym. Sci.*, 128 (3), 1804-1814 (2013).
- Smuleac, V.; Xiao, L.; Bhattacharyya, D. “Greener and Other Approaches To Synthesize Fe and Pd Nanoparticles in Functionalized Membranes and Hydrogel”. In Sustainable Nanotechnology and the Environment: Advances and Achievements, *American Chemical Society*: 2013; Vol. 1124, pp 41-58 (2013). (Book chapter)
- Lewis, R.S.; Smuleac, V.; Xiao, L.; Bhattacharyya, D. “Tunable separations, reactions, and nanoparticle synthesis in functionalized membranes”. In D. Bhattacharyya; T. Schäfer; S. R. Wickramasinghe; Sylvia Daunert, *Responsive Membranes and Materials* (pp. 97-132), *John Wiley & Sons* (2012). (Book chapter)

Professional Conference Presentations (Poster/Oral):

- Xiao, L., Smuleac, V., Bachas, L., Ormsbee, L., Bhattacharyya, D., “Hydrogel and Membrane Immobilized Nanoparticles for Water Detoxification”, 2010 NIEHS-SRP Annual Meeting, Portland, OR (2010) – Poster
- Xiao, L., Bhattacharyya, D., “Responsive Hydrogel for Nanoparticles Synthesis and Water Detoxification”, 2011 Annual NAMS meeting, Las Vegas, NV (2011)-Poster and Oral
- Xiao, L., Hilt, J. Z., Isner, A., Bhattacharyya, D., “Reactive Nanoparticles Immobilized in Hydrogel for Toxic Organics Degradation” 11th American Institute of Chemical Engineers Annual Meeting (AIChE), Minneapolis, MN (2011) – Oral
- Xiao, L., Isner, A., Bhattacharyya, D., “Toxic Organic Destruction by Temperature-responsive Hydrogel Immobilized Metallic Nanoparticles”, 2011 NIEHS-SRP Annual Meeting, Lexington, KY (2011) – Poster
- Xiao, L., Bhattacharyya, D., “Temperature Responsive Hydrogel for Nanoparticles Synthesis and Water Detoxification”, Sino-US Joint Chemical Engineering Conference, Beijing, China (2011) - Oral
- Xiao, L., Isner, A., Hilt, J. Z., Bhattacharyya, D., “Temperature Responsive Hydrogel Immobilized Reactive Nanoparticles for Toxic Organics

Degradation”, 2012 Annual NAMS meeting, New Orleans, LA (2012)-
Poster and Oral.

- Xiao, L., Gui, M., Smuleac, V., Isner, A., Varma, R., Ormsbee, L., Sikdar, S., Bhattacharyya, D., “ Green and Responsive Materials for Remediation”, 2012 NIEHS-SRP Annual Meeting, Raleigh, NC, (2012)-Oral.
- Xiao, L., Gui, M., Smuleac, V., Varma, R., Ormsbee, L., Sikdar, S., Bhattacharyya, D., “Integrated Iron-Polymer Membranes for Water Purification”, Research Translation Seminar Series, Frankfort, KY, (2013)-Oral.
- Xiao, L., Saad, A., Waldrop, K., Bhattacharyya, D., “Temperature Responsive Membranes for Separations and Water Detoxification”, 2013 NAMS Annual Meeting, Boise, ID, 2013-Oral and Poster.
- Xiao, L., Waldrop, K., Isner, A., Saad, A., Bhattacharyya, D., “Temperature Responsive Membranes Immobilized Nanoparticles for remediation”, 2013 NIEHS-SRP Annual Meeting, Baton Rouge, LA, 2013-Poster.
- Xiao, L., Isner, A., Saad, A., Waldrop, K., Bhattacharyya, D.,” Responsive Functionalized Membranes for Environmental Catalyst and Tunable Separations”, 2013 AIChE Annual Meeting, San Francisco, CA, 2013-Oral.